July 2017

A New Paradigm for Predicting Fracture Growth, Interaction and Linkage: Faulting in Numerical and Physical Experiments with Work Optimization

Jessica McBeck

A NEW PARADIGM FOR PREDICTING FRACTURE GROWTH, INTERACTION AND LINKAGE: FAULTING IN NUMERICAL AND PHYSICAL EXPERIMENTS WITH WORK OPTIMIZATION

A Dissertation Presented

by

JESSICA A. MCBECK

Submitted to the Graduate School of the
University of Massachusetts Amherst in partial fulfillment
of the requirements for the degree of

DOCTOR OF PHILOSOPHY

MAY 2017

Department of Geosciences

A NEW PARADIGM FOR PREDICTING FRACTURE GROWTH, INTERACTION AND LINKAGE: FAULTING IN NUMERICAL AND PHYSICAL EXPERIMENTS WITH WORK OPTIMIZATION

A Dissertation Presented

By

JESSICA A. MCBECK

Approved as to style and content by:

_____
Michele Cooke, Chair

_____
Sanjay Arwade, Member

_____
David Boutt, Member

_____
Elizabeth Madden, Member

_____
Bertrand Maillot, Member

_____

Julie Brigham-Grette, Department Head
Department of Geosciences

ACKNOWLEDGEMENTS

I have many people to thank for supporting me throughout my academic career, including many supportive and inspiring teachers. I am profoundly indebted to M. Cooke who has spent countless hours guiding my research pursuits, honing my scientific writing and fine-tuning my oral scientific communication. Any successes in my future scientific career are due to her excellent mentorship. Chris Condit provided invaluable guidance throughout my graduate studies, and without who I would not have matriculated at UMass. I am very grateful for the mentorship and welcoming of Bertrand Maillot, Pauline Souloumiac, and Baptiste Mary during my time in France. Betsy Madden, Laurie Brown, Mike Williams, Shelia Seaman, Barb Tewksbury and many others were excellent teachers and role models who I strive to emulate in my scientific and life pursuits. Finally, I would not exist without my wonderful parents, and likely would not have pursued higher education if I had not been surrounded by such an argumentative, inquisitive, stubborn family that relishes learning.

ABSTRACT

A NEW PARADIGM FOR PREDICTING FRACTURE GROWTH, INTERACTION AND LINKAGE: FAULTING IN NUMERICAL AND PHYSICAL EXPERIMENTS WITH WORK OPTIMIZATION

MAY 2017

JESSICA A. MCBECK, B.A., HAMILTON COLLEGE

M.A., UNIVERSITY OF MASSACHUSETTS AMHERST

Ph. D., UNIVERSITY OF MASSACHUSETTS AMHERST

Directed by: Professor Michele L. Cooke

This dissertation predicts fracture propagation and interaction within the framework of work optimization. With this approach, fractures are predicted to propagate along the path that optimizes work. This dissertation includes three projects that predict fracture growth using work optimization in varying tectonic environments. The projects build on work completed during my M.S. at UMass, which includes the development of the fracture modeling tool Growth by Optimization of Work (GROW) [*McBeck et al*., 2016]. GROW simulates fracture propagation, interaction and linkage by iteratively searching for fracture propagation paths that maximize the change in external work done on the system divided by the new fracture area propagated in an increment of growth, $\Delta W_{ext}/\Delta A$. In Ch. 1, I use GROW to simulate fault development in a crustal extensional step over. This investigation of a crustal fault network demonstrates the utility of the work optimization approach in predicting the development and interaction of crustal faults. The analyses investigate the influence of fault geometry and anisotropy on fault propagation and interaction, and the range of highly efficient fault propagation paths in extensional step over configurations. In Ch. 2, I integrate observations from physical and numerical experiments in order to predict the geometry of accretion faults in a numerical simulation of a physical accretion experiment. This analysis is a novel approach to predicting accretion fault geometry, which could complement traditional Coulomb failure criteria. In Ch. 3, I track the evolution of individual

components of the energy budget within an accretionary system. This analysis reveals the tradeoffs between competing deformational processes throughout the evolution of accretionary systems. The energy budget provides a framework for directly comparing the energetic contribution or consumption of diverse deformation mechanisms, from frictional sliding to internal host rock deformation.

TABLE OF CONTENTS

Page

LIST OF TABLES

LIST OF FIGURES

CHAPTER 1

PREDICTING THE EVOLUTION OF EXTENSIONAL STEP OVERS IN ANISOTROPIC SYSTEMS WITH WORK OPTIMIZATION: IMPLICATIONS FOR THE HAYWARD-RODGERS CREEK FAULT NETWORK

1.1. Abstract

Determining whether the northern Hayward fault is hard-linked to the southern Rodgers Creek fault within San Pablo Bay, CA, USA, or if the faults are separated by <5 km, is critical to assessing seismic hazard in the San Francisco Bay area. Recent geophysical imaging of the upper 5 m suggests that the Hayward fault hard-links to the Rodgers Creek fault near the onshore southern terminus of the Rodgers Creek fault. To constrain the geometry of this extensional step over at seismogenic depths, we simulate fault growth and interaction with the modeling tool Growth by Optimization of Work (GROW). GROW predicts fault growth by propagating faults in the orientation that maximizes the change in external work relative to new fault area. Two new implementations to GROW allow exploration of the sensitivity of fault growth to heterogeneities and anisotropy. The first implementation builds propagation forecasts of fault growth that indicate a range of highly efficient fault geometries. The second implementation enables fault propagation within anisotropic systems, such as foliated metamorphic host rock. These implementations applied to fault growth within extensional step overs indicate that early in extensional step over development, a single linking fault propagates across the step over, developing with relatively high propagation power, or rate of efficiency gain. After this first structure develops, faults propagate with

reduced propagation power, forming increasingly wider basins. These modeling efforts suggest that the dominant direction and strength of the anisotropy control fault development. Step over development in models with differing initial fault geometries suggest that the Hayward fault links with the Rodgers Creek fault at seismogenic depths if the mapped portion of the Rodgers Creek that extends into the San Pablo Bay is inactive. The model predictions of average slip rate, slip per earthquake and earthquake magnitude closely match paleoseismic estimates.

1.2. Introduction

The Rodgers Creek-Hayward fault network, near the San Pablo Bay in northern CA, USA, is predicted to have the highest likelihood (32%) of the faults within the San Francisco bay area of producing a magnitude ≥6.7 earthquake within the next 30 years [*Field et al*., 2015]. The surficial traces of the southern end of the dextral Rodgers Creek fault and northern end of the dextral Hayward fault form an extensional step over within San Pablo Bay, to the northeast of San Francisco (Fig. 1.1). Interpretations of seismic reflection and refraction data indicate that within the upper 1-2 km the Rodgers Creek and Hayward faults are separated by ~4 km [e.g., *Parsons et al*., 2003]. More recent ultrahigh-resolution seismic reflection cross sections attained with a chirp subbottom profiler suggest that a through-going transfer fault links the tip of the Hayward fault with the Rodgers Creek fault within 2-5 m of the surface (Fig. 1.1) [*Watt et al*., 2016]. Although this geophysical imaging has informed the present-day fault geometry within the shallow subsurface [e.g., *Watt et al.*, 2016], to fully assess seismic hazard in the San Francisco Bay region we must work to determine if the faults are linked at seismogenic

depths. Paleoseismic evidence shows that seismic rupture can be arrested when the perpendicular separation between strike-slip faults in a step over configuration is >5 km, but that rupture is more likely to propagate across step overs with smaller separation [e.g., *Lettis et al., 2002*; *Wesnousky*, 2008]. Simulating the evolution of the Hayward-Rodgers Creek step over may help predict the active fault configuration at seismogenic depths, and the associated likelihood of ruptures to arrest at the step over.

To predict the geometry of the Hayward-Rodgers Creek step over at seismogenic depths, we propagate faults in the direction that optimizes work with the numerical modeling tool Growth by Optimization of Work (GROW) [*McBeck et al.,* 2016]. In order to gain a first-order understanding of fault growth within extensional step overs, we first simulate the propagation and interaction of two underlapping planar faults with initial spacing and geometry that approximates the Rodgers Creek and Hayward fault strands. Relatively few numerical simulations have been able to robustly predict fault propagation in segmented fault networks [e.g., *Gupta et al*., 1998; *Cowie et al*., 2000; *Finzi et al*., 2009]. Consequently, determining the factors that control fault propagation and interaction between planar faults in an extensional step over constitutes an important step in understanding fault development in crustal step overs. Following the investigation of fault development in the simplified planar fault simulations, we predict the interaction between faults that more closely approximate the geometry of the southern segment of the Rodgers Creek fault and the northern segment of the Hayward fault. For both suites of models, we investigate the sensitivity of fault growth to host rock heterogeneities, including pervasive anisotropy.

1.3. Background

1.3.1. Extensional step over evolution in anisotropic systems

Field observations, scaled physical analog experiments and numerical and analytical techniques have shed insight on the mechanisms that control fault evolution [e.g., *Cooke et al.*, 2016]. Interpretations of field observations provide critical insight into the development of extensional step overs along strike-slip faults in crustal environments [e.g., *Mann et al*., 1983]. Quantitative monitoring of scaled physical experiments enable direct observation of the complete evolution of segmented fault systems [e.g., *McClay and Dooley,* 1995; *Cooke et al*., 2013; *Hatem et al*., 2015]. Additionally, numerical simulations enable analysis of the stress and strain field within segmented fault systems [e.g., *Willemse,* 1997; *Bürgmann,* 1994; *Crider and Pollard,* 1998; *Cowie et al*., 2000; *Kattenhorn and Pollard,* 2001]. Predicting the evolution of propagating faults is critical to constraining seismogenic hazard and identifying potential hydrocarbon sources.

Field observations of extensional step overs suggest that they initially develop as narrow basins bounded by faults that directly connect the strike-slip fault segments (Fig. 1.2) [e.g., *Mann et al*., 1983]. With additional strike-slip displacement, the initially narrow basins are thought to widen parallel to the strike of the main fault segments, and ultimately develop into rhomboidal shapes [e.g., *Mann et al*., 1983]. Scaled physical experiments of extensional basin evolution indicate that in the initial stages of basin development, obliquely-slipping normal faults propagate from the main fault segments and form a narrow graben connecting the segments [e.g., *Dooley et al*., 1999; *Rahe et al*., 1998; *Wu et al*., 2009; *Dooley and Schreurs*, 2012]. The initial geometry of the parallel fault segments controls the graben geometry: underlapping fault segments typically form

elongate, rhomboidal grabens, while overlapping fault segments develop box-like, rhomboidal graben [e.g., *McClay and Dooley,* 1995; *Dooley and McClay,* 1997]. With continued displacement, the basin may then widen via additional normal fault development [*Dooley et al*., 1999].

Segmented fault networks can develop in mechanically anisotropic crust. Strength anisotropy arises from the presence of pre-existing fractures, sedimentary layering, schistocity and other foliation. Field observations, physical experiments and numerical simulations reveal the influence of strength anisotropy on fault development. For example, field observations suggest that pre-existing basement fabrics [e.g., *Morley et al*., 2004], pre-existing normal faults [e.g., *Zampieri et al*., 2003] and stratigraphy within limestone and shale sequences [e.g., *Ferrill et al*., 2007] provide mechanical anisotropy that influence fault development. Zones of weakness in pre-rift sediments or crystalline rocks have been observed to exert a first-order control continental rift development [e.g., *McConnell*, 1972; *Dixon et al*., 1987; *Daily et al*., 1989; *Smith and Mosley*, 1993; *Morley et al*., 2004; *Cunningham and Mann*, 2007].

Physical experiments provide additional insight into the influence of anisotropy on fault development. The majority of scaled physical experiments that simulate fault development within heterogeneous systems aim to capture the influence of pre-existing faults on fault development [e.g., *Sassi et al*., 1993; *Faccenna et al*., 1995; *Bonini et al*., 1997; *Dubois et al*., 2002; *Bellahsen and Daniel*, 2005; *Del Ventisette et al*., 2006]. Triaxial compression tests of layered rocks show that the geometry of newly propagated faults changes with the orientation of the layering relative to the applied principal stresses [e.g., *Peacock and Sanderson*, 1992].

Numerical approaches further constrain the factors that control fault development within anisotropic systems. *Chester and Fletcher* [1997] present an analytical solution for the distribution of stress produced by sliding on a wavy frictionless fault within anisotropic material. This work simulates anisotropy by considering the rock to behave as an incompressible linear viscous fluid that has a greater resistance to contraction and extension than to shear in the principle anisotropy directions [*Chester and Fletcher*, 1997]. This seminal investigation indicates that as the magnitude of anisotropy increases, the pattern of shear failure within contractional and extensional step overs becomes increasingly similar, whereas in isotropic systems, the geometry of shear failure is distinctly different in contractional and extensional step over systems [*Chester and Fletcher,* 1997]. More recent numerical simulations represent pre-existing planes of weakness with elastic properties that differ from the host rock [e.g., *Yin*, 1994; *Gudmundsson et al*., 2010; *Tong and Yin*, 2010]. One of the few numerical simulations of step over development within an anisotropic system simulates fault development in a model with layers of different rheologies, representing the seismogenic upper crust overlying a viscoelastic substrate [*Finzi et al*., 2009]. Deformation within the simulated upper crust is determined by a thermodynamically-based continuum damage model for evolving elastic properties of rocks that sustain inelastic brittle deformation [*Finzi et al*., 2009]. In these models, strain is localized along damaged fault cores at seismogenic depths, and strain is distributed over a broader region at shallow depths [*Finzi et al*., 2009]. Throughout the entire simulated earthquake cycle, material within step overs remains damaged, with reduced rigidity and shear-wave velocity [*Finzi et al*., 2009].

In our parameterizations of pervasive strength anisotropy, we vary the internal friction coefficient as a function of orientation relative to a global coordinate system. GROW allows anisotropy to be simulated through the parameterization of other properties as well, including the inherent shear strength, tensile strength, and dynamic friction.

1.3.2. Regional tectonics of the San Pablo Bay area

The Hayward and Rodgers Creek faults are part of a complex fault network that lies to the east of the San Andreas fault, within the San Francisco Bay area of northern California, USA. Although many investigations work to constrain the evolution of the San Andreas fault [e.g., *Furlong et al*., 1989; *Powell*, 1993; *Matti and Morton*, 1993], fewer investigations focus on fault development near the San Pablo Bay. In this region, the majority of faults develop within the Franciscan Complex, which includes variably deformed and metamorphosed detrital sedimentary rocks that accreted along the western North American plate margin due east-dipping subduction of the Farallon slab [e.g., *Wakabayashi*, 1992]. After subduction ceased, major strike slip faults, including the San Andreas, developed within the Franciscan to accommodate right lateral slip between the Pacific plate and western North American plate boundary [e.g., *Wakabayashi*, 1992]. The Franciscan includes detrital sedimentary rocks (mostly sandstones), serpentinite, basaltic volcanic rocks and chert, and minor limestone [*Bailey et al*., 1964; *Blake et al*., 1988; *Coleman*, 2000; *Wakabayashi*, 2004, 2012]. Near the San Pablo Bay, the Franciscan complex consists of a stack of coherent nappes separated by low-angle mélange zones that were folded about NW-SE subhorizontal fold axes [*Blake et al*., 1984; *Wakabayashi*

and Moores, 1988; *Wakabayashi*, 1989, 1992]. The Franciscan stack of nappes is ~10 km thick, and folded into a broad NW-trending synform centered on Tiburon Peninsula, and a parallel antiform centered on the eastern San Francisco Bay [*Blake et al*., 1984; *Wakabayashi and Moores*, 1988]. Thick mélange zones (200-1500 m) separate the coherent nappes, and thinner mélange zones (<300 m) are part of the internal imbrication of the coherent nappes [e.g., *Wakabayashi*, 1992].

In the San Pablo Bay area, volcanism related to a northward migrating slab window, large scale block rotations and plate motions, and northward-migrating restraining and releasing bends have contributed to fault development by weakening the crust, changing the principal stress orientations and promoting fault development near pre-existing faults [*McLaughlin et al*., 2012 and references therein]. Interpretations of $^{40}Ar/^{39}Ar$ dating, tephrochronology, gravity and aeromagnetic data, and structural relationships suggest that the Rodgers Creek fault zone initiated ~7 Ma from a proto-Hayward fault zone as a transtensional basin-forming fault [*McLaughlin et al*., 2012]. Recent interpretations of geophysical imaging within the San Pablo Bay [*Watt et al*., 2016] refine the evolution of *McLaughlin et al*. [2012], suggesting that at ~8 Ma, changes in plate motion lead to transpression and fault reorganization within the San Pablo Bay. After this reorganization, a transtensional basin developed between southern segment of the Rodgers Creek, and northern segment of the Hayward. After ~7 Ma, the Hayward segment propagated north toward the Rodgers Creek until it connected [*Watt et al*., 2016].

1.4. Fault propagation and interaction with GROW

1.4.1. Simulating fault development with Growth by Optimization of Work

To determine how the Rodgers Creek and Hayward faults may link at seismogenic depths, we simulate step over evolution with the numerical modeling tool GROW (Fig. 1.3) [*McBeck et al*., 2016; *Madden et al*., in review]. GROW simulates fracture propagation by adding elements to growing fracture tips in the radial orientation that optimizes the change in external work, W_{ext}, produced by fracture propagation divided by the change in new fracture area, $\Delta W_{ext}/\Delta A$ [*McBeck et al*., 2016]. In a two-dimensional system, W_{ext} may be calculated from the sum of the products of shear traction and displacement, τ and u_s, and normal traction and displacement, σ_n and u_n, integrated over the system boundaries, B:

$$W_{ext} = \frac{1}{2}\iint_B (\tau u_s + u_n\sigma_n)\, dB \qquad \text{Eq. 1.1}$$

The factor of one-half is appropriate for one loading step because W_{ext} is the area under the force-displacement curve. This area forms a triangle shape with one loading increment. When multiple loading steps are used, external work is calculated by integrating over multiple loading steps because the W_{ext} produced at each loading increment may not increase monotonically.

To find the boundary tractions and displacements required to calculate external work, GROW repeatedly calls the boundary element method (BEM) program Fric2D [*Cooke and Pollard*, 1997]. Boundaries and fractures are discretized into linear segments that may open or slip, but not interpenetrate, in response to tractions or displacements applied to the boundaries, or perturbations from other fractures. Slip and tractions on dislocation

surfaces are calculated with the quasi-static equations of deformation following the displacement discontinuity method.

In GROW, fractures stop propagating when fractures link with other fractures or the model boundaries, or when none of the radial elements added to the tip of the fracture fail in tension or shear. An element fails in tension when the normal stress across its surface, σ_n, which is positive when tensile, exceeds or equals the tensile strength of the intact rock at the fault tip. A potential growth element fails in shear following the Coulomb criterion, when the magnitude of the shear stress across its surface, τ, exceeds or equals the difference between the inherent shear strength, S_0, and the product of the internal coefficient of friction, μ_0, and normal stress, σ_n (tension positive), across the potential element. This formulation of the Coulomb criterion describes the propagation of faults through intact rock. Consequently, in GROW, the properties of the new radial elements added to the tip of the growing fault should be within ranges appropriate for intact rock.

When two or more faults are growing, GROW searches sequentially for the optimal orientation of potential fault elements [*McBeck et al.*, 2016]. In particular, GROW finds the optimal orientation of an element at the tip of one growing fault, adds this element to the fault tip, and then searches for the optimal orientation of an element added to the tip of another growing fault. In this second step, the efficient element found at the first tip is included within the model. After the most efficient element orientations are identified for all of the growing faults, GROW enters a tuning step that searches for the most efficient combination of element orientations at all the fault tips with element orientations close to the most efficient orientations found in the first step [*McBeck et al.*, 2016].

1.4.2. GROW fault development in anisotropic systems

To enable GROW to better predict the evolution of fracture networks in crustal tectonic settings in which the host rock may not be isotropic, we implemented a new functionality that allows GROW to simulate fault development in systems with anisotropic material properties. These properties may be any of the intact material properties, such as the inherent shear strength and internal friction coefficient. The user determines the specific function or set of values that describes the anisotropy of the property or properties relative to a two-dimensional global coordinate system, which is measured clockwise from the left horizontal plane. Such pervasive anisotropy may be present in host rocks with preexisting stratigraphic layering, fractures or metamorphic fabric [e.g., *Chester and Fletcher*, 1997].

This implementation is particularly beneficial for simulating fault propagation within the San Pablo Bay because the NW-SE trend of the metamorphosed Franciscan complex provides significant strength anisotropy in the San Francisco Bay region that approximately parallels the strike of the fault segments outside of the step over [e.g., *Wakabayashi*, 1992]. The NW-SE subhorizontal fold axes of nappes within the Franciscan complex near San Pablo Bay contribute to this anisotropy because thick mélange zones separate the coherent nappes, and thinner (<300 m) mélange zones provide internal imbrication within the nappes [e.g., *Wakabayashi*, 1992]. The Franciscan complex contains serpentinite [e.g., *Wakabayashi*, 2004; 2012], which introduces strength anisotropy at the grain scale.

To predict the interaction of the Hayward and Rodgers Creek fault strands, we parameterize the anisotropy of the host rock by varying the internal coefficient of friction.

This distribution of internal friction is controlled by the orientation at which the friction is minimized, θ_{min}, the magnitude of the minimum internal friction coefficient, μ_0^{min}, the magnitude of the maximum internal friction coefficient, μ_0^{max}, and the degrees from θ_{min} at which the friction is maximized, or saturated, θ_{sat} (Fig. 1.4)**.** These parameters control the curve that describes anisotropy. The distribution of internal friction employed in this analysis resembles an ellipse with a flat top. We constructed this function to describe strength anisotropy because varying the parameters θ_{min} and μ_0^{min} provides insight into the sensitivity of fault development to various expressions of strength anisotropy in crustal rocks. Parameterizing θ_{min} reveals how the direction of pervasive anisotropy controls fault development. Parameterizing μ_0^{min} reveals the influence of the magnitude of the anisotropy, which may differ depending on the physical characteristic that produces the anisotropy.

In particular, the internal coefficient of friction, μ_0^{min}, at some orientation, θ_i, between θ_{min}-θ_{sat} and θ_{min}+θ_{sat} is defined by an ellipse with horizontal radius of θ_{sat} and vertical radius of μ_0^{max}-μ_0^{min} that is shifted in the vertical (μ) direction by μ_0^{min}, and shifted in the horizontal (θ) direction by θ_{min}-θ_{sat},

$$\frac{(\theta_i-(\theta_{min}-\theta_{sat}))^2}{{\theta_{sat}}^2}+\frac{(\mu_i-\mu_{0min})^2}{(\mu_{max}-\mu_{min})^2}=1 \qquad \text{Eq. 1.2}$$

The distribution of friction is symmetric, and so both θ_{min} and 180°-θ_{min} minimize friction.

1.4.3. GROW propagation forecasts

The second new implementation enables GROW to better predict the propagation of interacting faults in heterogeneous systems by building propagation forecasts of fault growth. These propagation forecasts outline the range of possible fracture geometries, while the original GROW algorithm predicts only one optimal path from a growing fracture tip [*McBeck et al*., 2016]. Heterogeneities within the system may induce growing faults to deviate from the optimal propagation path. Propagation forecasts aim to encompass such epistemic uncertainties by describing a range of likely deviations from the optimal path. The forecasts use the distribution of external work at each growth increment to determine the likely range of efficient geometries.

To build the propagation forecast, at each increment of growth, GROW finds the $\Delta W_{ext}/\Delta A$ produced by the addition of each element radial to the growing fracture tip (Fig. 1.5A). GROW then identifies the range of element orientations within a certain percentage of the maximum $\Delta W_{ext}/\Delta A$ through linear interpolation of the $\Delta W_{ext}/\Delta A$ results. GROW then calculates the $\Delta W_{ext}/\Delta A$ of the interpolated system to ensure accurate representation of the efficiency of the system with the interpolated element orientation.

When the distribution of $\Delta W_{ext}/\Delta A$ is broad, the resulting propagation forecast will be relatively broad (Fig. 1.5). A wide propagation forecast indicates that the fault propagation path may be sensitive to local heterogeneities that would promote propagation away from the optimal path. Conversely, when the distribution of $\Delta W_{ext}/\Delta A$ has one well-defined narrow peak, the propagation forecast will be narrow, closely enveloping the optimal growth path (Fig. 1.5). A narrow propagate forecast reveals that the propagation is relatively insensitive to heterogeneities.

In most GROW simulations, the distribution of $\Delta W_{ext}/\Delta A$ in an increment of growth contains one peak (Fig. 1.5). Consequently, there will be two element orientations for which a certain percentage of the maximum $\Delta W_{ext}/\Delta A$ is achieved, and the user must select whether the maximum or minimum orientation, relative to the clockwise direction from the fault tip, will be identified as the extent of the propagation forecast in that particular GROW run. Consequently, one GROW run produces one edge of a propagation forecast, and two GROW runs are required to build one propagation forecast from the tip of one growing fault, or many propagation forecasts from the tip of many growing faults. After the forecast element orientation is identified, it is added to the tip of the growing fault, and GROW searches for the next forecast element orientation from the tip of the previously added element. With the propagation forecast implementation, GROW does not enter a tuning step to refine the search for the most efficient element orientation at each increment of growth.

1.4.4. Loading conditions

To derive the displacements applied to the 2D model boundaries (Fig. 1.6), we superpose the displacements due to lithostatic confining stress and the displacements due to tectonic motion that accumulate over several thousand years. We progressively increase the number of years simulated within an increment of fault growth from 2500 years, in steps of 500 years, until the faults link or until an applied time interval of 5000 years is not sufficient to propagate the faults. In particular, we begin the GROW run by applying the displacements from lithostatic stress and accumulated over 2500 years of tectonic motion, and if the faults stop propagating before linking with the other fault, we

then increase the number of years simulated in an increment of growth by 500 years. We cease increasing the loading after the faults stop propagating when 5000 years of tectonic displacements are simulated. This progressive loading of several thousand-year time intervals is well-suited for simulating fault interaction within step overs because it encompasses several earthquake cycles of the Rodgers Creek-Hayward faults, which have a recurrence rate of 230-710 years [e.g., *Schwartz et al*., 1992; *Hayward Fault Paleoearthquake Group*, 1999].

To derive the displacements applied to the model boundaries due to lithostatic stress, we convert lithostatic stress to strain via Hooke's elasticity relationships, and then convert strain to displacements. Relocated earthquake hypocenters [*Waldhauser and Schaff*, 2008; version v201112.1] indicate that the seismogenic zone beneath San Pablo Bay extends from ~7-12 km. These GROW models simulate fault development at 7 km depth. We calculate the lithostatic stress, σ_L, at 7 km with the density of mafic rock, (ρ = 2700 kg/m^3), the depth, d, and gravitational constant, g, in a tension positive sign convention, as

$$\sigma_L = -gd\rho \qquad \text{Eq. 1.3}$$

The fault parallel, ε^L_{xx}, and perpendicular, ε^L_{yy}, strains due to lithostatic stress are derived using Hooke's 2D plane strain relationships,

$$\varepsilon^L_{xx} = \left(\frac{1-\nu^2}{E}\sigma_{xx} - \frac{\upsilon(1+\upsilon)}{E}\sigma_{yy}\right) \qquad \text{Eq. 1.4}$$

$$\varepsilon^L_{yy} = \left(\frac{-\upsilon(1+\upsilon)}{E}\sigma_{xx} + \frac{1+\upsilon^2}{E}\sigma_{yy}\right) \qquad \text{Eq. 1.5}$$

where E is Young's modulus, ν is Poisson's ratio and $\sigma_{xx} = \sigma_{yy} = \sigma_L$.

To derive the applied displacements arising from tectonic motion, we calculate the total strain that accumulates over several thousand years from the components of the regional strain rate tensor. The best-fitting uniform horizontal strain field for the San Francisco bay region has principal strain rates of $\dot{\varepsilon}_{11}$ = 164.7±7.2 nanostrain/yr and $\dot{\varepsilon}_{22}$ = -157.9±6.9 nanostrain/yr oriented N74.0°W and N16.0°E, respectively, with contraction negative [*Pollitz and Nyst*, 2005]. A coordinate transformation of the principal strain rate tensor provides the components of the strain rate tensor parallel and perpendicular to the fault strikes due to tectonic motion, $\dot{\varepsilon}_{ij}$. The total strain that accumulates over t years due to long term tectonic motion is then $\varepsilon^T_{ij} = \dot{\varepsilon}_{ij} t$. The total strain parallel, ε_{xx}, and perpendicular, ε_{yy}, to the faults due to tectonic motion and lithostatic stress is $\varepsilon^T_{xx} + \varepsilon^L_{xx}$, and $\varepsilon^T_{yy} + \varepsilon^L_{yy}$, respectively. The shear strain of the modeled region does not include a lithostatic component, and is ε^T_{xy}.

The displacements applied to the model boundaries are calculated from the derived strain and the initial model width, w, and height, h. The normal displacement applied to the top model boundary equals the change in model height due to the total normal strain perpendicular to the faults, $h\varepsilon_{yy}$. The normal displacements applied to the right boundary equals the change in model width due to the normal strain parallel to the faults, $w\varepsilon_{xx}$. We apply the displacements due to ε_{xy} with a step-wise distribution on the model boundaries so that all of the ε_{xy} due to tectonic motion is resolved on the modeled faults. The shear displacements applied to the model boundaries maintain kinematic compatibility (Fig. 1.6A-B). The applied displacements produce a region of elevated strain energy density

between the growing fault tips, with higher and lower strain energy density lobes along the length of the faults outside and inside the fault step over (Fig. 1.6C-D).

1.4.5. Initial fault geometry

In order to investigate the influence of material anisotropy on fault development, we first simulate fault growth in two suites of models (Fig. 1.6). We simulate fault interaction in simplified models in which the perpendicular separation distance between the planar, parallel underlapping faults matches the approximate distance between the subparallel strands of the Rodgers Creek and Hayward faults [*Watt et al*., 2016]. In the second suite of models, the initial geometry of the modeled faults follows the geometry inferred from geophysical observations [*Watt et al*., 2016].

In the simplified fault models, we use the propagation forecast implementation of GROW to reveal highly efficient fault geometries that may differ from the optimal geometry due to local heterogeneities. In particular, we present results from GROW runs in which the percentage, *p*, that determines the extent of the propagation forecast is 90% and 95%. We then investigate the influence of strength anisotropy on fault development by parameterizing the internal coefficient of friction (Fig. 1.4B-D). To investigate the influence of the direction of anisotropy, we vary the orientation of minimum internal friction coefficient from 160-200° clockwise from the left horizontal plane. To investigate the control of the strength of anisotropy, we vary the magnitude of the minimum internal friction coefficient from 0.1-0.4, and keep the maximum internal friction coefficient constant at 0.6.

In the Hayward fault propagation simulations, the initial fault geometries are approximated from recent geophysical interpretations of the fault strands within San Pablo Bay, but do not include the recently identified linking segment [*Watt et al.,* 2016]. Whereas earlier geophysical data indicated that the Rodgers Creek fault extends into the San Pablo Bay [*Parsons et al.,* 2003], *Watt et al*. [2016] does not find evidence of this segment of the Rodgers Creek fault in the upper 2-5 m. In order to shed insight on the active geometry of the Rodgers Creek fault within San Pablo Bay, we develop two simulations with differing active Rodgers Creek fault lengths (Fig. 1.7). The two fault configurations enable exploration of the influence of the Rodgers Creek segment that may extend into the San Pablo bay (Fig. 1.1), and deflect toward the Hayward fault (Fig. 1.7). In contrast to the simplified fault simulations, in these simulations we do not predict the propagation of both the Rodgers Creek and Hayward fault, but only search for the efficient propagation path of the Hayward fault, because here we aim to constrain the fault geometry of the Hayward segment. Similar to the parametric study of the planar fault configuration, with these simulations we will explore the influence of host rock anisotropy on Hayward fault development.

1.4.6. Material and fault properties

The prescribed material properties represent mafic, metamorphosed rock similar to the Franciscan complex (Table 1.1). The coefficients of internal, static and dynamic friction are within measurements from laboratory strength experiments [e.g., *Byerlee*, 1978; *Lockner et al*., 2011]. In these simulations, the prescribed inherent shear strength determines if propagating fault tips fail under the applied loading conditions. The applied

tensile strength does not influence whether the tips fail because the region in which the faults grow in the model is in compression, and so failure only occurs in shear.

Tests with GROW models with high inherent shear strength reveal that increasing the inherent shear strength of the faults prevents the tips from failing, and so stops the propagation of the faults earlier than the models with lower inherent shear strength. However, whether the fault tips fail in shear depends on the displacements applied to the model boundaries. Changing the inherent shear strength only determines if a potential fault element fails, and will not change the amount of slip along potential fault elements that fail, which is determined by the evolving fault friction. Consequently, the distribution of $\Delta W_{ext}/\Delta A$ among failed fault elements will remain the constant under the same loading conditions, and the orientation of the most efficient element will remain unchanged as long as the same set of elements fail. In this study, we do not aim to predict the number of simulated years after which a fault tip stops propagating, but rather to predict the long-term evolution of step over development.

In this contribution, we simulate anisotropy strength by parameterizing the internal friction coefficient from 0.1 to 0.6, which is within the range of internal friction calculated in laboratory experiments for rocks containing weak mineral phases [e.g., *Lockner et al*., 2011]. Although laboratory strength experiments have been exacted on intact wafers of anisotropic rocks with foliation planes of phyllosilicates [e.g., *Collettini et al*., 2009], constraining the distribution of internal friction coefficient as a function of orientation within one rock type has remained elusive.

Strength measurements of rock samples collected from surface outcrops near the Hayward fault in northern California [*Morrow and Lockner*, 2001] provide constraints on

the distribution of frictional strength at seismogenic depths within San Pablo Bay. Failure and frictional sliding tests on intact rock cylinders of antigorite serpentinite from New Idria, CA, at room temperature and effective pressures up to 192 MPa (12 km) find that the intact friction coefficient is between 0.60-0.92 [*Morrow and Lockner*, 2001]. Of the rock samples tested by *Morrow and Lockner* [2001], the altered keratophyre produced the lowest internal friction coefficient estimates (0.43-0.66).

Strength measurements of fault gouge and intact wall rock from the San Andreas Fault Observatory at Depth (SAFOD) near Parkfield, CA, further constrain the potential range in strength of rocks within San Pablo Bay. The phase III multilateral core drilling operation recovered core from fine-grained sandstones to mudstones in the wall rock near two shear zones, and foliated fault gouge consisting of sedimentary rock and serpentinite porphyroclasts within a matrix of Mg-rich clays from the shear zones [*Holdsworth et al*., 2011]. Frictional strength measurements indicate that the stable sliding friction of the sedimentary wall rock is between 0.6-0.4, and that the internal friction is similar in magnitude [*Lockner et al*., 2011]. The measured sliding friction of powders created from the foliated fault gouge is much lower than the wall rock (0.13-0.21), which may be due to the abundance (60-65% volume) of the weak mineral saponite (0.05) in the fault gouge [*Lockner et al*., 2011]. The *in situ* intact and sliding frictional strength of the wall rock and fault gouge may be lower than the values measured in the laboratory tests because the preparation of the samples involved grinding the returned core into a powder. The measured frictional strength of intact, undisturbed samples can be less than half the frictional strength of their powder derivatives if the rocks contain well-developed foliation planes that host weak minerals [e.g., *Collettini et al*., 2009].

In summary, the existing literature suggests that the internal friction coefficient of crustal materials within the San Pablo Bay could be between the minimum (0.1) and maximum (0.6) internal friction coefficients applied in our parameterizations of anisotropy.

To determine the appropriate length of the fault and boundary elements, we perform a discretization analysis that is described in full in the supporting information. Systematic variation of the element length reveal that an element length of 250 m provides a robust compromise between the model solution (external work) and model run time.

1.5. Simplified fault development

1.5.1. Propagation forecasts of simplified fault

For the simplified fault models, the most efficient propagation path of each fault gently curves towards the other fault, until linking with the other fault (Fig. 1.8A). The zone of the 95% propagation forms a shape similar to the narrow basins that are thought to develop early in extensional step over evolution (Fig. 1.2A). The zone of the 90% propagation forecast is about a third as wide as the 95% zone (Fig. 1.8A). The highly efficient propagation paths form increasingly wide basins, with the geometry of the 90% propagation forecast defining the widest basin, and the width of the basin decreasing with increasing percentage criterion.

The distribution of $\Delta W_{ext}/\Delta A$ in the first increment of growth provides insight into the resulting propagation forecasts (Fig. 1.8B). For the elements added to the upper left fault tip in the first growth increment, the outside limit of the 95% propagation forecast is 4° from the optimal orientation, whereas the inside limit of the 95% propagation forecast is

2° from the optimal orientation. This anisotropy to the $\Delta W_{ext}/\Delta A$ distribution produces an asymmetric propagation forecast that has a greater area toward the outside of the step over, so that the outside limits of the propagation forecasts are further from the optimal path than the inside limits in the first fault growth increment. In the first few increments of fault growth, the inside limits of the 95% propagation forecast closely parallels the optimal path, propagating within 0.5 km (Fig. 1.8A).

The evolution of $\Delta W_{ext}/\Delta A$ reveals how fault interaction controls the efficiency gain and propensity for fault growth (Fig 1.8C). Power is the rate of change in work, and in GROW simulations, fracture growth is a proxy for time. Consequently, the change in $\Delta W_{ext}/\Delta A$ due to fracture growth is the propagation power [*McBeck et al*., 2016]. The evolution of propagation power of the optimal system shows that after the first increments of growth, the system gains efficiency at a faster rate than the outside limits of the 95% and 90% propagation forecasts (Fig. 1.8C). The propagation power of the optimal propagation path, and the outside limits of the propagation forecasts, reveal when the faults begin to interact via soft and hard linkage: when the tips of the faults begin to overlap across the step over, $\Delta W_{ext}/\Delta A$ increases slightly (Fig. 1.8C). The largest gain in efficiency, and greatest propagation power occurs when the faults hard-link.

1.5.2. Simplified fault development with anisotropy

Both the strength and direction of pervasive, host rock anisotropy influence fault propagation (Fig. 1.9). In these parameterizations, we control the anisotropy strength by varying the minimum internal friction coefficient, μ_0^{min}, and keeping the maximum internal friction coefficient at 0.6 (Fig. 1.9A). We control the anisotropy direction with

the orientation at which the internal friction coefficient is minimized, θ_{min}. When $\mu_0^{min}$is 0.1, simulating the strongest anisotropy, and θ_{min} is 160º, the predicted fault geometry matches the predicted geometry of the isotropic system (Fig. 1.9C). The distribution of $\Delta W_{ext}/\Delta A$ produced by potential growth elements in the first increment of growth (Fig. 1.9B) reveals that the increase in $\Delta W_{ext}/\Delta A$ at 160º due to the reduction in the internal friction coefficient is not sufficient to overcome the larger $\Delta W_{ext}/\Delta A$ at the most efficient orientation in the isotropic system. The fault propagates at 200º instead of 160º because the influence of the fault tip stress field is stronger than the influence of the material anisotropy. However, when θ_{min} is 180º, the increase in $\Delta W_{ext}/\Delta A$ produced by the potential fault element at 180º is sufficient to shift the optimal orientation from 200º to 180º. The increase in ΔW_{ext} due to the 180º fault element is produced by the lower internal friction along the potential element, which allows more slip along the element and consequently, less tractions along the boundaries to accommodate the applied displacements. In this case, the material anisotropy has greater influence on fault propagation direction than the fault tip stress field. When the anisotropy direction is 200º, the preference for growth along this orientation promotes the faults to propagate parallel to this direction until linking with the other fault (Fig. 1.9C).

The strength of anisotropy controls the predicted fault geometry when the anisotropy direction differs from the most efficient orientation of the isotropic system identified in the first increment of growth (Fig. 1.9D-I). When θ_{min} is 180º, and the strength of the anisotropy is greatest, (μ_0^{min}=0.1, μ_0^{max}=0.6), the faults parallel to the anisotropy direction (Fig. 1.9D-F). In simulations with weaker anisotropy (μ_0^{min}>0.1, μ_0^{max}=0.6), the faults initially propagate parallel to each other, and then propagate toward each other at

shallow angles, propagating just inside and outside of the high efficiency region defined by the isotropic propagation forecast envelopes (Fig. 1.8A). In the first increment of fault growth, the gain in efficiency at 180º is sufficient to shift the optimal direction from 200º to 180º for all the tested strengths (Fig. 1.9E). However, the resulting propagation paths of the systems in which μ_0^{min}>0.1 (Fig. 1.9F) demonstrate that after the first initial increments of fault growth, the fault tip stress field overwhelms the influence of material anisotropy.

When the anisotropy direction is 200º, and the anisotropy strength varies as μ_0^{min}=0.1-0.4, the differing anisotropy strength does not change the overall predicted geometry (Fig. 1.9G-I). In particular, when θ_{min} is 200º, changing the strength of the anisotropy only produces changes in the predicted path within ~500 m of the adjacent fault.

1.6. Hayward fault simulations

1.6.1. Propagation forecasts of Hayward fault

To constrain the active geometry of the Hayward and Rodgers Creek faults, we simulate the propagation of the Hayward faults in two models with different initial fault geometries (Fig. 1.6). The fault geometries of the two models differ in the length of modeled Rodgers Creek fault. In one model, the Rodgers Creek fault geometry follows the geometry inferred from early geophysical imaging that identified the southern terminus of the Rodgers Creek fault within the San Pablo Bay [*Parsons et al.,* 2003]. In the other model, the Rodgers Creek fault geometry follows the geometry inferred from recent geophysical imaging that did not find evidence of slip along the Rodgers Creek

fault within the San Pablo Bay [*Watt et al.*, 2016]. In the models in which the Rodgers Creek fault terminus lies outside the bay, the modeled Rodgers Creek fault is shorter than the Rodgers Creek fault in the other models.

The highly efficient propagation paths of the Hayward fault closely match the geometry of the northern Hayward strand inferred from recent geophysical imaging (Fig. 1.10). In the Hayward fault simulation with the shorter Rodgers Creek fault, the inferred trace of the Hayward lies within the 90% propagation forecast envelope. In the longer Rodgers Creek simulation, the inferred Hayward trace lies outside of the 90% propagation forecast, although the leftmost (northwest) edge of the 90% propagation forecast intersects a <1 km portion of the inferred Hayward trace. The optimal Hayward path predicted in the shorter Rodgers Creek fault simulation lies closer to the geophysically inferred Hayward trace than the optimal path predicted in the longer Rodgers Creek simulation.

1.6.2. Hayward fault propagation in anisotropic systems

To shed insight on the sensitivity of fault development to pervasive anisotropy within the San Pablo bay, we vary the anisotropy direction from 180º to 200º. We explore anisotropy with these orientations because the dominant strength anisotropy in the San Pablo Bay area likely parallels or subparallels the strikes of the Hayward and Rodgers Creek faults [e.g., *Wakabayashi*, 1992].

In both suites of models with differing Rodgers Creek fault geometries, when the anisotropic direction is 200º, the predicted Hayward fault propagation paths are within 0.5 km of the inferred trace along its entire length (Fig. 1.11A). In the model with the

longer Rodgers Creek fault, when the anisotropy direction is 180º, the predicted Hayward path curves toward Rodgers Creek at a steeper angle than the inferred fault path (Fig. 1.11B). However, in the model with the shorter Rodgers Creek fault, a difference in the anisotropy direction of 20º, from 180º to 200º, does not produce as significant changes in the predicted Hayward geometry as in the model with the longer Rodgers Creek fault (Fig. 1.11A). In the model with the shorter Rodgers Creek fault, when the anisotropy direction is 180º, the predicted path of the Hayward fault intersects the interfered Hayward trace along most of its length.

The reduced sensitivity of fault development to anisotropy direction in the shorter Rodgers Creek fault model indicates that the fault tip stress field exerts greater influence on fault propagation in the shorter Rodgers Creek fault model than in the longer Rodgers Creek fault model. The elevated mode II stress intensity factor of the Hayward fault tip in the model with the shorter Rodgers Creek fault (2248 MPa*$m^{1/2}$) relative to the model with the longer Rodgers Creek fault (2064 MPa*$m^{1/2}$) supports the interpretation that fault tip stress field more strongly controls fault development in the shorter Rodgers Creek fault model. A step over with a geometry similar to the shorter Rodgers Creek model is more likely to produce the geophysically-inferred geometry under a wider range of anisotropic conditions than a step over with a geometry similar to the longer Rodgers Creek model.

1.7. Discussion

The simplified fault propagation simulations presented here shed insight on the interaction of propagating faults in underlapping extensional step over geometries, and

the evolution of efficiency due to fault growth and linkage. The Hayward fault propagation simulations constrain potential active fault geometries of the Hayward-Rodgers Creek step over at seismogenic depths with the San Pablo Bay. In the following sections, we discuss the implications of these modeling efforts, future laboratory strength measurements that could help determine if the applied parameterizations of internal friction are likely to occur within San Pablo bay, and the seismic hazard implications of the northern end of the Hayward fault linking with southern end of the Rodgers Creek fault.

1.7.1. Evolution of planar step over faults

Following the assumption that as a step over evolves, the most efficient faults develop first and subsequently, less efficient faults develop, we may build temporal evolutions of step over development using the optimal paths predicted by GROW, and the propagation forecasts, which reveal the extent of less efficient propagation paths. Early in extensional step over development, the adjacent faults may propagate toward each other at a steep angle to the parent fault until linking with the other fault tip, forming a geometry similar to the optimal path predicted by GROW (Fig. 1.8), and proposed by *Mann et al*. [1983] (Fig. 1.2). After the fault tips link between the parallel parent strands, the next stage of fault development may include the propagation of faults that surround the initial linking structure, forming a narrow basin geometry (Fig. 1.2B). Our modeling efforts suggest that the propagation of these surrounding faults may increase the total system efficiency at a lower rate, with reduced propagation power, than the first linking structures that form. The geometry of the 95% and 90% propagation forecasts of the simplified fault

simulations suggest that as the step over matures, new faults could continue to develop outside the initial linking structure and subsequent narrow basins, forming increasingly larger basins that produce gains in efficiency at an increasingly lower rates.

These simplified simulations lend additional evidence that pervasive host rock anisotropy can exert a significant influence on fault development. Both the strength and direction of the anisotropy determine whether the presence of anisotropy changes fault propagation, interaction and linkage. While considering the extent of propagation forecasts may address the potential impact of local heterogeneities, anisotropy can produce fault paths that propagate outside the isotropic forecast envelopes (Fig. 1.9).

1.7.2. Propagation of the Hayward fault

The improved prediction of the Hayward fault geometry in simulations with a shorter active Rodgers Creek segment suggests that the mapped portion of the Rodgers Creek fault within San Pablo Bay may have been inactive at the time that the Hayward fault propagated and linked. Whereas marine magnetic anomalies, gravity gradients and seismic reflection data provide evidence of slip along the Hayward fault within the upper 5 m of the San Pablo Bay, these datasets do not indicate recent slip along the potential portion of the Rodgers Creek fault that lies within the bay [*Watt et al*., 2016], which was previously inferred from geophysical data [*Parsons et al*., 2003]. However, this portion of the Rodgers Creek could be present at deeper levels. Our modeling efforts are consistent with the more recent interpretations, which suggest that the southern extent of activity on the Rodgers Creek fault lies outside the bay [*Watt et al*., 2016].

1.7.3. Frictional strength distribution at seismogenic depths within San Pablo Bay

For the simplified fault simulations, a difference in internal friction coefficient of only 33%, from 0.6 to 0.4, is sufficient to cause the predicted fault propagation paths to deviate from those within the isotropic system (Fig. 1.9). For the Hayward fault propagation simulations, the predicted Hayward fault propagation path is similar to the inferred fault trace when the anisotropy direction is 200º from the left horizontal plane, and the anisotropy strength is the largest applied here, with a minimum and maximum internal friction coefficient of 0.1 and 0.6, respectively. Laboratory measurements of the internal friction coefficient of highly foliated, metamorphosed accretionary sediments in which the orientation of foliation planes is varied with respect to the principal stresses would help evaluate if the parameterization of anisotropy employed in these numerical simulations are likely to occur in the San Pablo Bay at seismogenic depths.

Microstructural observations of deforming serpentinite indicate that microcracks dominantly form parallel to the (001) cleavage of serpentine grains [*Escartin et al*., 1997], suggesting that the orientation of foliation planes in serpentinites control the anisotropic strength distribution. Moreover, the frictional strength of dry sheet structure minerals, including lizardite serpentinite, positively correlate with the (001) interlayer bond strength [*Moore and Lockner*, 2004]. Secondary-electron SEM photomicrographs of shear surfaces indicate that interlayer bond strength controls frictional strength because platy minerals rotate into alignment with shear planes that develop, and shear occurs via breakage of the interlayer bonds [*Moore and Lockner*, 2004].

These frictional strength estimates indicate that the range in internal friction coefficient of the host rock within San Pablo Bay could be as large as the range in the

internal friction coefficient (0.1, 0.6) prescribed in our anisotropy distribution. The direction of planes of weakness, i.e., the prescribed anisotropy direction, is likely controlled by the orientation of foliation planes of weak minerals [e.g., *Moore and Lockner*, 2004; *Collettini et al*., 2009]. Geologic evidence suggests that the dominant orientation of foliation planes are parallel and subparallel to the onshore strike of the Hayward and Rodgers Creek faults near the San Pablo Bay [e.g., *Wakabayashi*, 2004]. Consequently, we are confident that our chosen parameterizations of anisotropy distribution are within estimates of the strength distribution in the San Pablo Bay. Additional laboratory strength measurements of different orientations of highly foliated serpentinite in intact wafers from outcrops near the Rodgers Creek-Hayward fault network would help determine the most appropriate strength distribution for this crustal step over.

1.7.4. Seismic hazard

To estimate earthquake magnitude with these quasi-static models, we use the average slip along modeled faults within the simulated time increment, the recurrence interval of the faults estimated from historical and paleoseismic data, and the empirical relationship of average slip to moment magnitude of *Wells and Coppersmith* [1994]. We estimate the modeled slip per event as the average slip rate along the faults divided by the number of earthquakes expected to occur within the simulated time. We find the number of earthquakes from the simulation time (2500) divided by the minimum (230 years) [*Schwartz et al*., 1992] and maximum (710 years) [*Hayward Fault Paleoearthquake Group*, 1999] estimates of the recurrence intervals for the Rodgers Creek fault or

Hayward fault. We calculate the slip per event in two models that both contain a short Rodgers Creek fault: in one model, the Hayward fault is not linked with the Rodgers Creek and in the other, the Hayward fault links with the Rodgers Creek (Fig. 1.12).

The model with the connected faults provides greater average slip rate (5.4 mm/yr) and range of slip per event (1.3-3.9 m) relative to the unconnected fault model because fault linkage facilitates slip transfer between the faults. The low slip along the portion of the Rodgers Creek fault to the right of the linking segment highlights the transfer of slip. In the unconnected fault model, the average slip rate is 4.4 mm/yr and the slip per event ranges from 1.0-3.1 m. The reported range in slip per event reflects the range in recurrence interval estimated for the Hayward fault or Rodgers Creek fault (230-710 years). Empirical relationships of average surface slip per event to moment magnitude indicate that the average earthquake magnitude may be 7.2-7.6 M [*Wells and Coppersmith*, 1994], with the larger magnitude corresponding to the linked faults. This earthquake magnitude range agrees with estimates from geodetically-inferred slip on the Hayward fault in the 1868 earthquake (7 M) [*Yu and Segall*, 1996], and estimates from historical earthquake evidence and paleoseismic slip rates of the magnitude of the combined rupture of the Hayward and Rodgers Creek faults (7.09-7.39 M) [*Schwartz et al*., 2014].

The minimum estimates of average slip per event are similar to estimates of slip per event derived from paleosiesmic data near the southern end of the Rodgers Creek fault. Offset channels in late Holocene alluvial deposits at the Beebe Ranch site (1.8-2.3 m) [*Budding et al*., 1991; *Schwartz et al*., 1992], and an offset channel at the Triangle G Ranch site (1.6-3.4 m) [*Hecker et al*., 2005] produce ranges in slip per event near our

minimum estimates (1.0-1.3 m). The Triangle G site and Beebe Range site are ~15 km northwest of the edge of the San Pablo bay that the Rodgers Creek fault approaches, and consequently lie just outside the left (northwest) edge of our model domain. The largest surface rupture estimated for the Rodgers Creek fault at the Beebe Range site (2.8-5.4 m) [*Budding et al*., 1991] more closely matches the maximum estimates of slip per event (3.1-3.9 m). Our estimates of slip per event are similar to geodetically-inferred slip in the 1868 Hayward fault earthquake (1.4-2.3 m) [*Yu and Segall*, 1996].

The estimates of average slip rate in our models (4.4-5.4 mm/yr) are slightly less than geologic estimates of the slip rate of the Rodgers Creek and Hayward faults. The latest Pleistocene to Holocene slip rate for the northern Hayward fault section is constrained from dextral offset of Strawberry Creek in Berkeley and radiocarbon dating of fluvial terraces (~10 mm/yr) [*P.L. Williams personal commun.*, 1999], and dextral offset of a marine-abrasion-platform embayment in the Point Pinole area (site 55a-1, 3.5 mm/yr) [*Borchardt*, 1998]. Offset channels at the Beebe Ranch site indicate that the slip rate of the Rodgers Creek fault is 6.4-10.4 mm/yr [*Schwartz et al*., 1992], with a minimum slip rate of 2.1-5.8 mm/yr for the past 1300 years [*Budding et al*., 1991]. The average model slip rate may be lower than these geologic estimates because the measurements were taken outside of the San Pablo Bay, where the local fault complexity of the step over may reduce slip rates. In summary, our model estimates of average slip rate, slip per event and earthquake magnitude are within ranges estimated from geologic and historical evidence.

1.8. Conclusions

To constrain the geometry of the Rodgers Creek-Hayward fault within the San Pablo Bay at seismogenic depths, we simulate the propagation and interaction of the northern Hayward fault and the southern Rodgers Creek fault using the work optimization modeling tool GROW. Simulations of fault interaction in simplified extensional step overs produce patterns similar to fault geometries expected in the early stages of extensional step over development. Propagation forecasts of fault development suggest that the optimal configuration of the first linking structure between two underlapping faults in an extensional step over is a single transfer fault. As the step over evolves, younger faults develop outside of the older faults, forming increasingly wider basins. The evolution of propagation power within GROW simulations indicates that the first faults that develop produce relatively large gains in efficiency as they grow, and subsequent faults produce increasingly smaller gains in efficiency, developing with reduced propagation power relative to the first faults. Simulations of fault interaction within anisotropic systems indicate that both the orientation and strength of anisotropy determine whether strength anisotropy or fault tip stresses control the predicted fault propagation paths. In the simplified step over simulations explored here, the orientation of planes of weakness must be within 40° of the fault strike to impact the fault propagation path. In these simulations, the frictional strength of the anisotropy only needs to be 33% less than the host rock to cause the predicted fault propagation paths to deviate from the predicted paths in the isotropic system.

In simulations of the Hayward fault propagation, models including a shorter Rodgers Creek fault that does not extend into the San Pablo Bay produce Hayward fault propagation paths that closely match the inferred geometry. Models with a longer Rodgers Creek fault, which extends into the bay, do not produce Hayward fault propagation paths that match the inferred geometry, except when the anisotropy direction is 20° from the Rodgers Creek fault strike. In models with a shorter Rodgers Creek fault, a difference of 20° in the anisotropy direction only minimally changes the predicted Hayward fault propagation path, indicating that fault propagation is relatively insensitive to changes in anisotropy direction for this step over configuration. Under a range of anisotropic frictional strength distributions, the most efficient fault propagation path from the Hayward fault more closely matches the inferred fault trace in the shorter Rodgers Creek fault models. The average slip rate and slip per event produced in models with a shorter Rodgers Creek fault predict that the average moment magnitude of earthquakes may be 7.2-7.6 M, consistent with estimates from historical earthquake and paleoseismic geologic observations [e.g., *Schwartz et al*., 2014].

1.9. Figures

Figure 1.1

Interpreted fault geometry of San Pablo step over. The Rodgers Creek and Hayward faults extensional step over within San Pablo Bay, to the north of San Francisco Bay, CA, USA. A) Context map with Google Earth image (Map data: Google, SIO, NOAA, US Navy, NGA, GEBCO, Image Landsat/Copernius) and quaternary faults from USGS fault and fold database (white) [*US Geological Survey and California Geological Survey*]. Red box indicates study area shown in (B). B) Fault geometry of step over from previous interpretations in black dashed lines [*Parsons et al*., 2003] and more recent interpretations in solid gray lines [*Watt et al*., 2016].

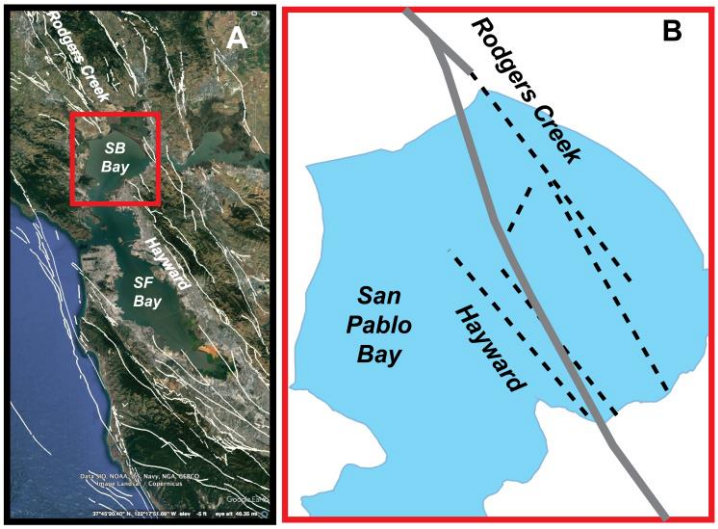

Figure 1.2

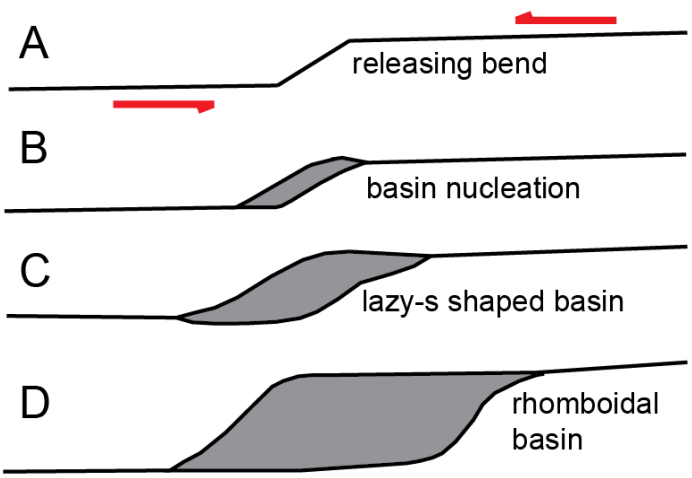

Idealized development of releasing step overs. Modified from *Mann et al*. (1983). A) First, fault hard-links tips of underlapping fault segments, forming releasing bend. B) Narrow basin develops. C) Basin widens and becomes more elongate, developing into "lazy-S" shape. D) Rhomboidal basin forms.

Figure 1.3

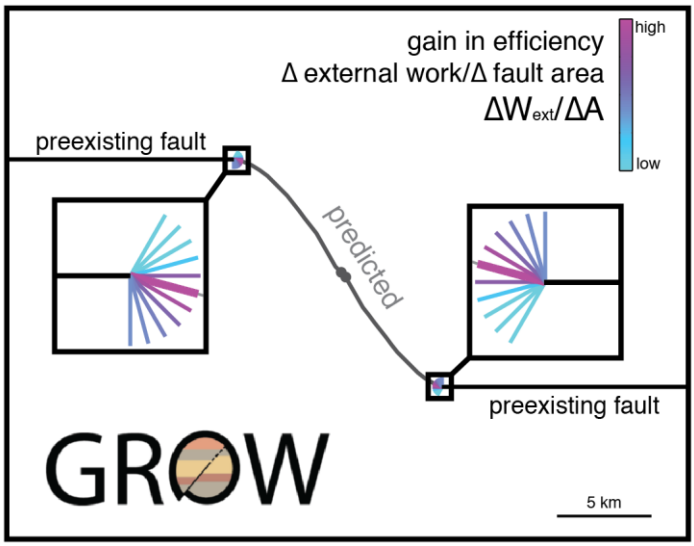

Schematic of GROW algorithm. GROW predicts fault interaction by selecting the propagation paths that optimize $\Delta W_{ext}/\Delta A$. Faults stop growing when they link with other faults or model boundaries, or if the fault tip does not fail in shear or tension.

Figure 1.4

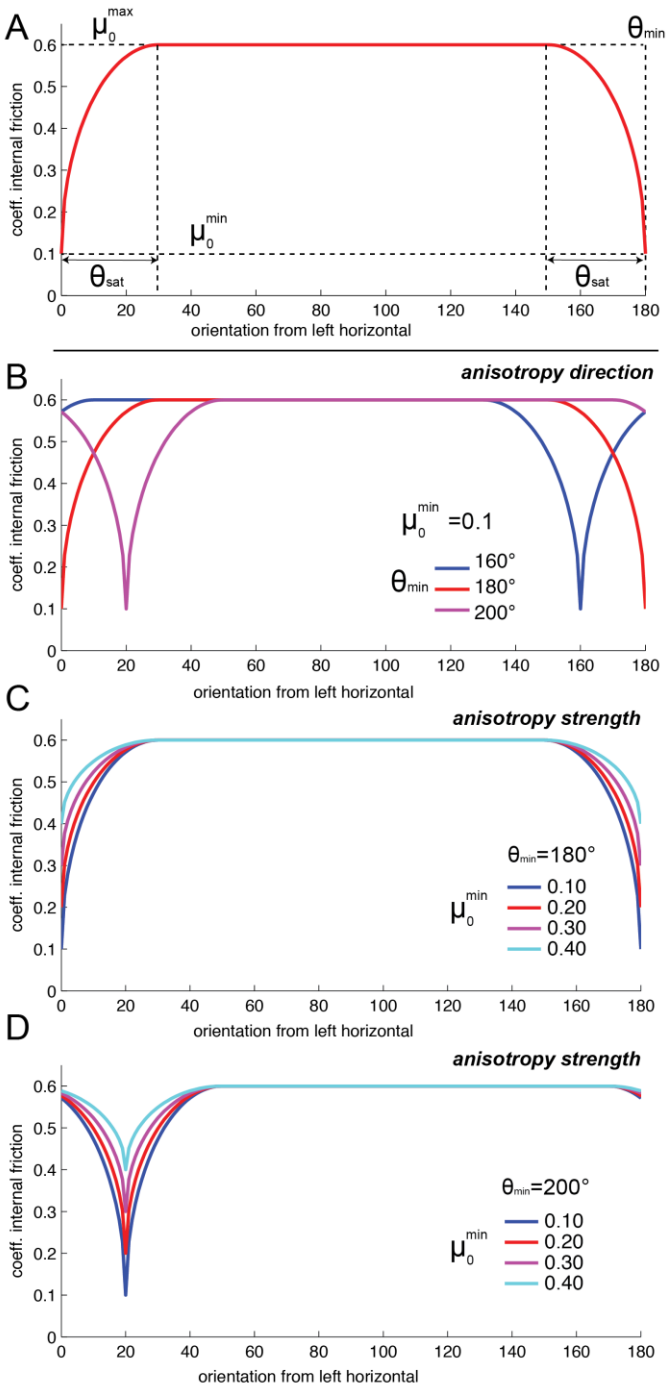

Anisotropic distributions of internal friction coefficient, μ_0. A) Friction distribution is controlled by orientation at which μ_0 is minimized, θ_{min}, the magnitude of the minimum friction coefficient, μ_0^{min}, the magnitude of the maximum friction coefficient, μ_0^{max} (0.6), and the degrees from θ_{min} at which the friction is maximized, or saturated, θ_{sat} (30°). B-D) Internal friction distributions used in simulations. B) Distribution when θ_{sat}=30°, μ_0^{max}=0.6, μ_0^{min}=0.1, and θ_{min} is 160° (blue), 180° (red) and 200° (dark blue) from global left horizontal plane. C) Distribution when θ_{sat}=30°, μ_0^{max}=0.6, θ_{min} =180°, and μ_0^{min}=0.1 (dark blue), 0.2 (red), 0.3 (pink) and 0.4 (light blue) from global left horizontal plane. D) Distribution when θ_{sat}=30°, μ_0^{max}=0.6, θ_{min} =200°, and μ_0^{min}=0.1 (dark blue), 0.2 (red), 0.3 (pink) and 0.4 (light blue) from global left horizontal plane.

Figure 1.5

Construction of propagation forecasts. A) Distribution of $\Delta W_{ext}/\Delta A$ calculated in initial search for efficient propagation path orientation (red dots). Horizontal lines show $p\frac{\Delta W_{ext}}{\Delta A}$ for each percentage. B) Close up of box in (A). Large rectangles indicate range of potential fault element orientations that produce $\Delta W_{ext}/\Delta A$ greater or equal to $p\frac{\Delta W_{ext}}{\Delta A}$. Squares show $\Delta W_{ext}/\Delta A$ calculated for fracture geometries that include an element at each interpolated angle. C-D) Distribution of $\Delta W_{ext}/\Delta A$ at each growth increment determines width of propagation forecast. When the distribution contains narrow peak (C), the propagation forecast is expected to be narrow, indicating that heterogeneities may only minimally impact fault propagation (C inset). When the distribution is broad (D), the propagation forecast is expected to be broad, indicating that fault growth will be sensitive to heterogeneities (D inset).

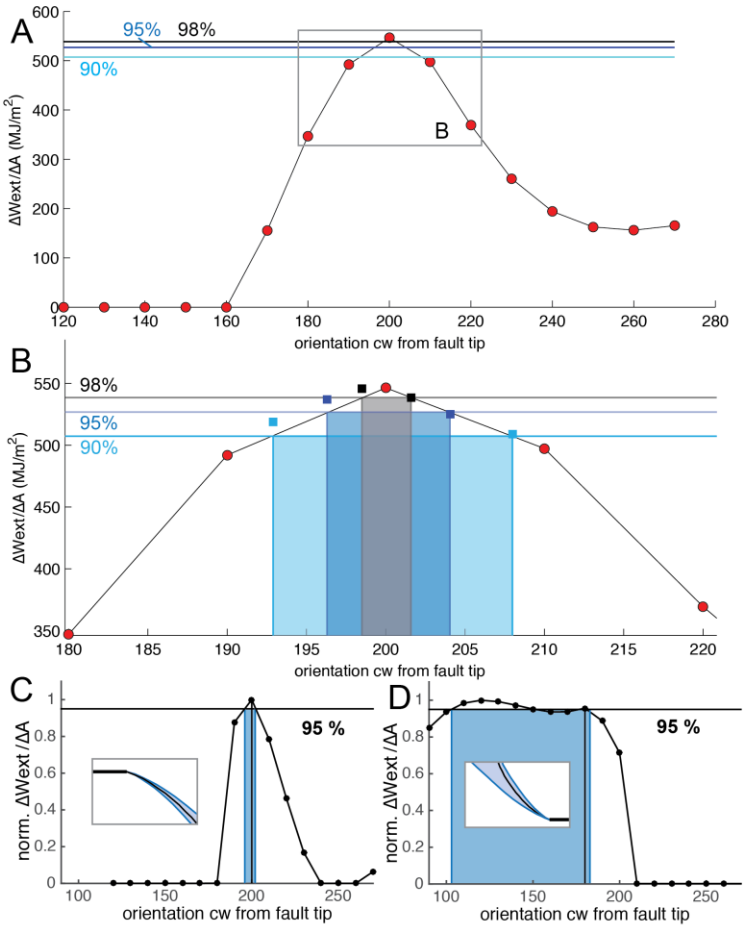

Figure 1.6

Development of numerical model loading conditions. Displacements applied to model boundaries for simplified fault simulations (A) and Hayward fault propagation simulations (B). Strain energy density (SED) field produced by applied boundary displacements for simplified fault simulations (C) and Hayward fault propagation simulations (D). Average SED of Hayward fault propagation simulation is similar to average SED of simplified fault simulations, indicating similarity of stress field near fault tips.

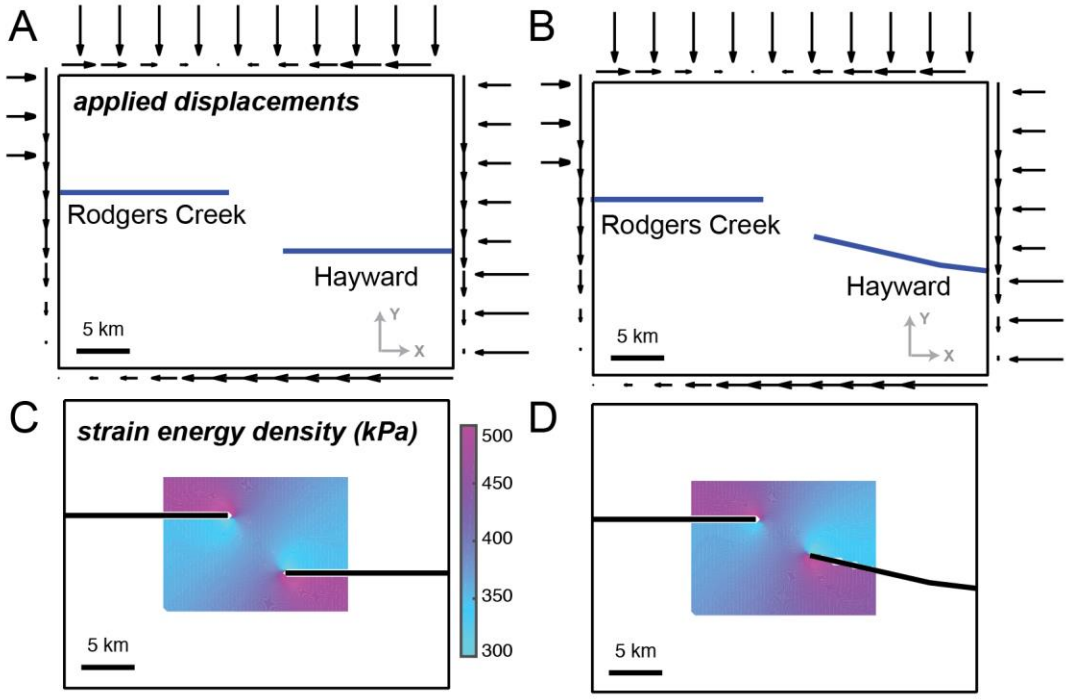

Figure 1.7

Initial fault geometry of Hayward fault propagation simulations. A) Shorter and B) longer Rodgers Creek fault. Dashed segment indicates Hayward fault geometry inferred from geophysical imaging [*Watt et al*., 2016].

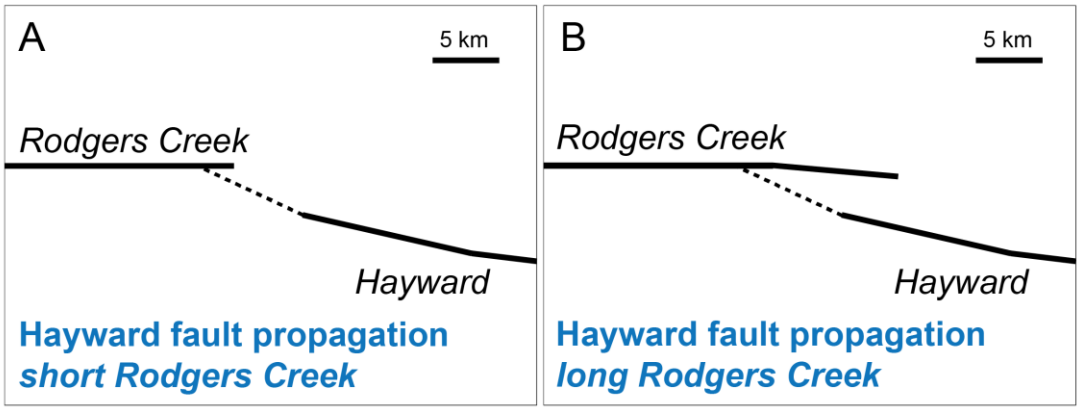

Figure 1.8

Optimal paths and propagation forecasts of simplified fault simulations. A) Predicted fracture geometries for simplified fault simulations of most efficient (black), and 95% (red) and 90% (blue) propagation forecasts. Inset figure shows model boundaries. B) Distribution of $\Delta W_{ext}/\Delta A$ produced by addition of elements to upper left fault tip in the first increment of growth. The asymmetric shape of the propagation forecast arises from the anisotropy of $\Delta W_{ext}/\Delta A$. C) The evolution of $\Delta W_{ext}/\Delta A$ throughout fault growth for the optimal propagation (black), and the outside limits of the 95% (red) and 90% (blue) propagation forecasts. Inset figures show fault geometry when fault begin to overlap (1), when faults more fully overlap (2), and when faults link (3). Fault elements propagated by GROW are colored by $\Delta W_{ext}/\Delta A$ at growth increment in which element was added. Propagation power is the slope of the $\Delta W_{ext}/\Delta A$ curves.

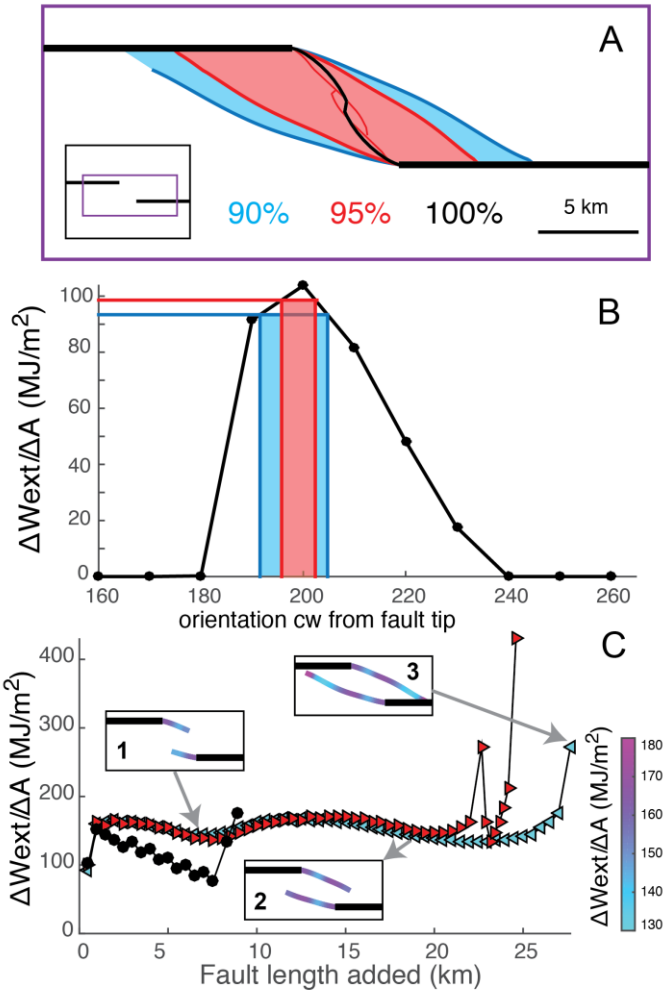

Figure 1.9

Predicted fault geometries for anisotropic systems. A-C) Varying θ_{min} from 160° (red), 180° (pink) and 200° (light blue), with θ_{sat}=30°, μ_0^{max}=0.6, μ_0^{min}=0.1. Distribution of internal friction coefficient in first increment of growth at tip of upper left fault (simplified Rodgers Creek fault) (A), resulting $\Delta W_{ext}/\Delta A$ at this growth increment (B), and complete propagation paths for each anisotropic system (C). D-F) Varying μ_0^{min} from 0.1 (red), 0.2 (pink), 0.3 (blue), and 0.4 (green), with θ_{min}=180°, θ_{sat}=30°, μ_0^{max}=0.6. Distribution of internal friction coefficient in first increment of growth at tip of upper left fault (D), resulting $\Delta W_{ext}/\Delta A$ at this growth increment (E), and complete propagation paths for each anisotropic system (F). G-I) Varying μ_0^{min} from 0.1 (red), 0.2 (pink), 0.3 (blue), and 0.4 (green), with θ_{min}=200°, θ_{sat}=30°, μ_0^{max}=0.6. Distribution of internal friction coefficient in first increment of growth at tip of upper left fault (G), resulting $\Delta W_{ext}/\Delta A$ at this growth increment (H), and complete propagation paths for each anisotropic system (I). Gray shaded region in C), F) and I) indicate extent of 90% propagation forecast envelope.

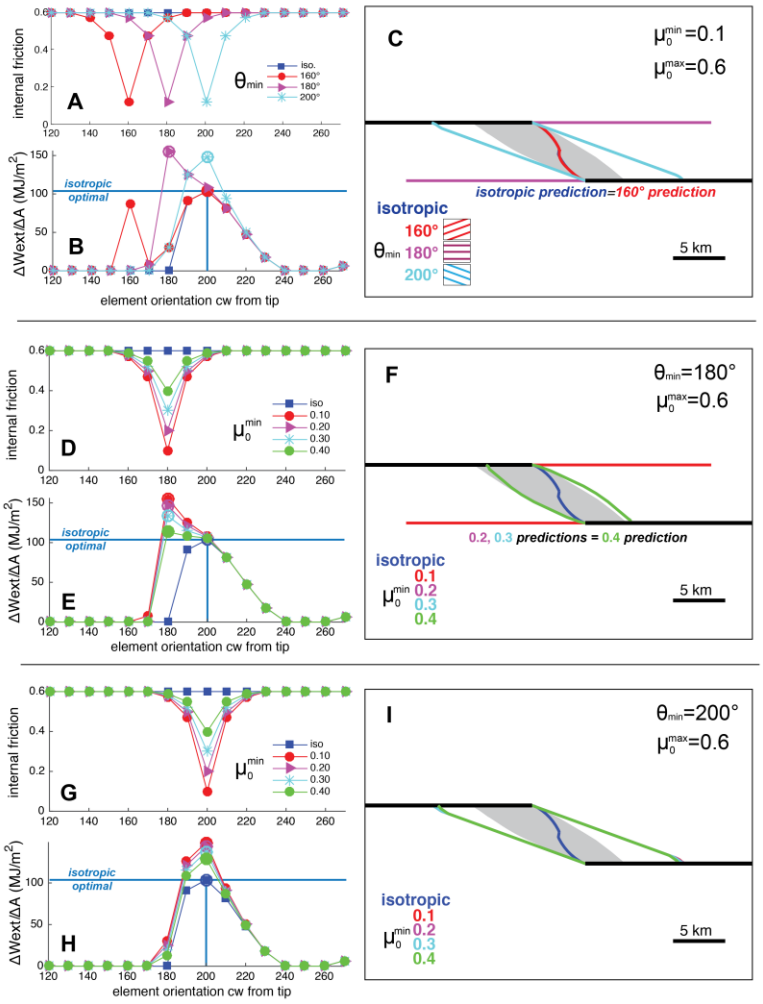

Figure 1.10

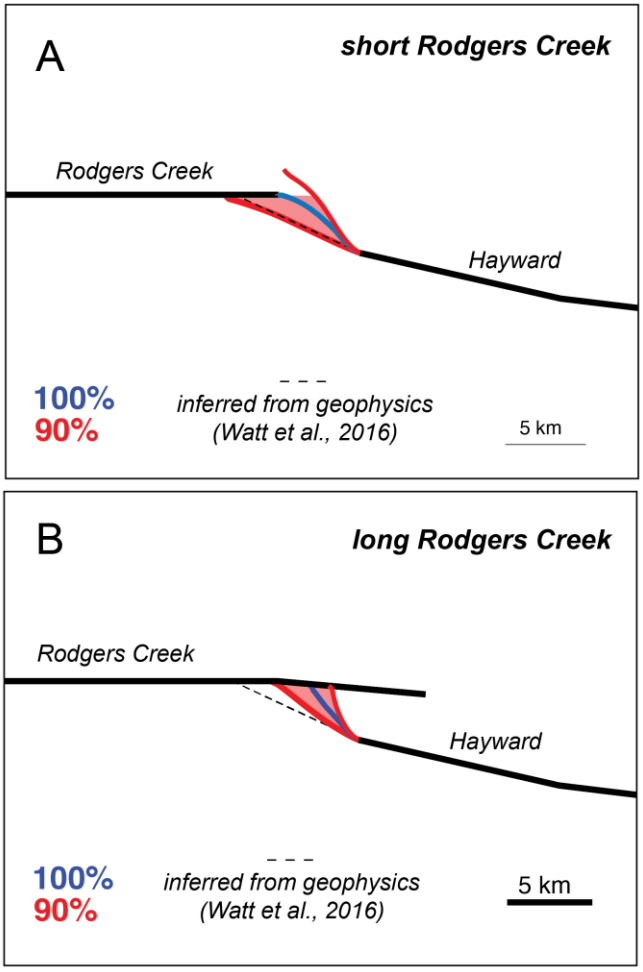

Optimal path and propagation forecasts of Hayward fault. A) Shorter Rodgers Creek and B) longer Rodgers Creek fault. Dashed lines indicate fault geometry inferred from geophysical imaging of *Watt et al.* (2016). The 90% propagation forecasts of both models intersect or overlap the inferred trace of the Hayward fault. Propagation forecast of the Hayward fault more fully overlaps the inferred trace, and the optimal path of the Hayward fault is closer to the inferred trace in shorter Rodgers Creek fault model.

Figure 1.11

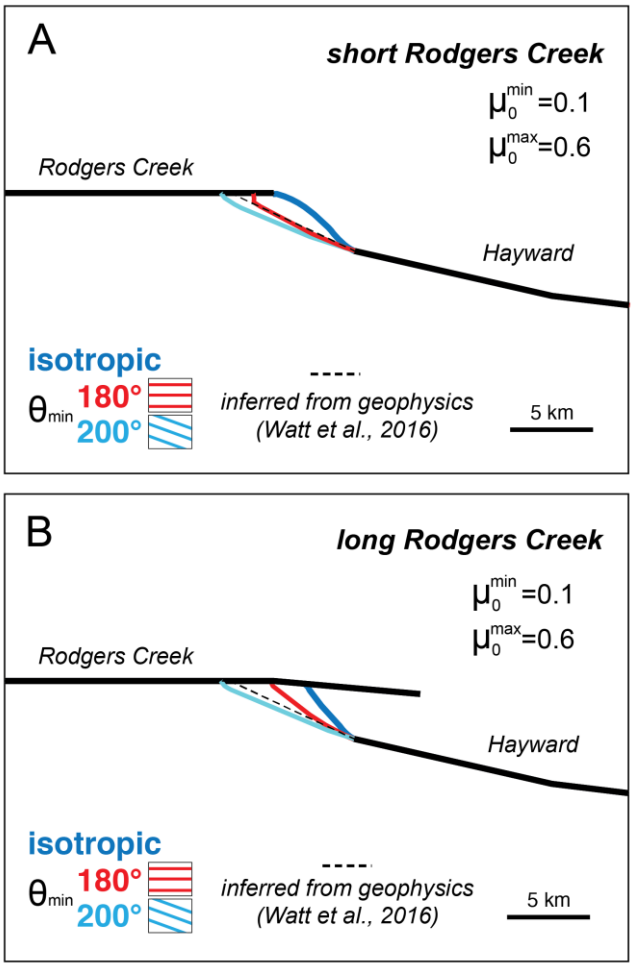

Predicted optimal Hayward propagation in anisotropic systems. A) Shorter and B) longer Rodgers Creek fault. Anisotropic systems with θ_{sat}=30°, μ_0^{min}=0.1, μ_0^{max}=0.6, and θ_{min} is 180° (red) or 200° (light blue). When θ_{min}=200°, the predicted Hayward propagation path is similar to the inferred geometry in both sets of models. When θ_{min}=180°, the predicted Hayward path is closer to the inferred trace in the model with a shorter Rodgers Creek. In both models, when θ_{min}=180°, the predicted fault geometry matches the fault geometry predicted in the isotropic simulation.

Figure 1.12

Average slip per event along faults. Models with unconnected (A) and connected (B) Rodgers Creek and Hayward faults with the minimum (230 years) and maximum (710 years) recurrence intervals estimated for the Rodgers Creek and Hayward faults. Average slip per event, and the associated earthquake magnitude estimated from *Wells and Coppersmith* [1994], increases when faults are connected. Fault linkage increases slip near fault terminations by transferring slip from one fault to the other.

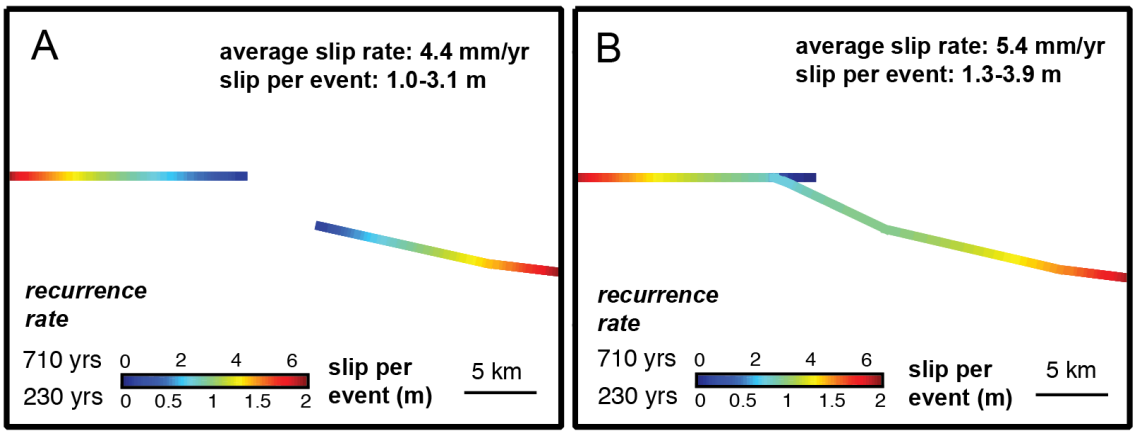

1.10. Tables

Table 1.1

Intact rock and material properties of step over models. Values are representative of intact crustal rock, and estimates of crustal fault properties [e.g., *Byerlee*, 1978; *Lockner et al*., 2011; *Morrow and Lockner*, 2001].

Property	Value
Poisson's ratio	0.25
Young's modulus	60 GPa
Density	2700 kg/m^3
Tensile strength	0 MPa
Inherent shear strength	0 MPa
Internal friction coefficient	0.6
Cohesion	0 MPa
Static and dynamic friction coefficient	0.1
Slip-weakening distance	2 m

1.11. Supplemental information

1.11.1. Discretization analysis

In order to determine the appropriate length of the fault and boundary elements, we perform a discretization analysis in which the element length is are systematically varied (Fig. S1.1). The shape of the discretization curve indicates that an element length of 250 m provides a model solution that is similar to the solution of the model with the smallest possible element size (200 m) (Fig. S1.1). The difference in the calculated external work of the model with 250 m long boundary elements and 200 m long boundary elements is only 0.2% of the external work of the 200 m long boundary element model.

The distribution of $\Delta W_{ext}/\Delta A$ in the first increment of fault growth indicates that the most efficient propagation direction does not change when the fault element size ranges from 100-500 m (Fig. S1.1). Because GROW determines the direction of fracture growth, and the geometry of interacting fracture tips, from the $\Delta W_{ext}/\Delta A$ due to fracture growth, both the absolute value of W_{ext} and the $\Delta W_{ext}/\Delta A$ distribution serve as critical metrics of model reliability. The $\Delta W_{ext}/\Delta A$ distributions for each tested fault element length differs from each other because the newly added fault elements sample varying portions of the stress and strain fields near the growing fracture tips. We selected a fault element size of 250 m because this length is <1% of the total modeled length of the faults, which has proven to appropriately sample the stress and strain field near growing fracture tips in previous GROW simulations [e.g., *Madden et al*., in review; *McBeck et al*., 2016].

Supplemental Figure S.1.1

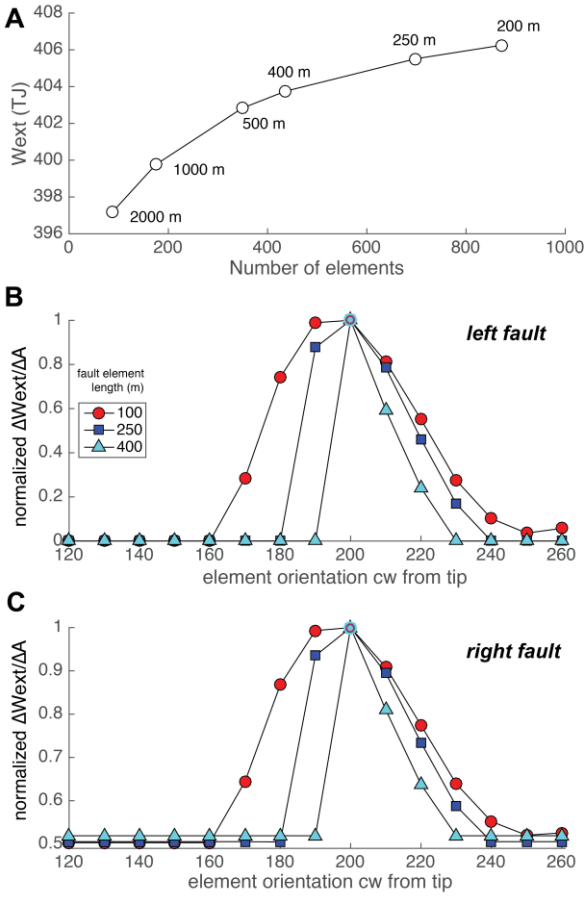

Discretization analysis. A) External work, W_{ext}, for models with different element lengths. Numbers next to symbols indicate element length. Distribution of $\Delta W_{ext}/\Delta A$ at first increment of growth from tip of simplified Rodgers Creek (B) and Hayward (C) fault for constant boundary element length (250 m), and differing fault element lengths: 100 m (red), 250 m (dark blue), and 400 m (light blue). The most efficient angle orientation remains constant at 200° as fault element length changes by factor of five.

CHAPTER 2

WORK OPTIMIZATION PREDICTS ACCRETION FAULTING: AN INTEGRATION OF PHYSICAL AND NUMERICAL EXPERIMENTS

2.1. Abstract

We employ work optimization to predict the geometry of frontal thrusts at two stages of an evolving physical accretion experiment. Analysis of numerical simulations indicates that fault dip and position determine the gain in efficiency due to fault development. Faults that produce the largest gains in efficiency, or change in external work per new fault area, $\Delta W_{ext}/\Delta A$, are considered most likely to develop. The predicted thrust geometry matches within 1 mm of the observed position and within a few degrees of the observed fault dip, for both the first forethrust and the first backthrust when the observed forethrust is active. The positions of the second backthrust and forethrust that produce >90% of the maximum $\Delta W_{ext}/\Delta A$ also overlap the observed thrusts. The work optimal fault dips are also within a few degrees of the faults dips that maximize the average Coulomb stress. Analysis of the evolving work budget reveals that for the fault growth investigated, the energy expended in off-fault deformation and frictional slip contribute more to the work budget than work against gravity. The evolution of mechanical efficiency for the two simulated stages resembles the evolution of experimental force. The numerical estimates of work consumed by fault propagation, $W_{prop}/\Delta A$, overlap the range calculated from experimental force data. The similarities of fault prediction and efficiency evolution between the numerical and physical experiments suggest that the models closely capture the development of the experimental faults.

Integrating numerical and physical experiments provides insight into the competing deformation mechanisms that control fault development.

2.2. Introduction

Geophysical observations have shed critical insight on the geometry of faults that develop at the front of accretionary wedges [e.g., *Bangs et al.*, 2004; *Barnes et al.*, 2002; *Davey et al.*, 1986; *Gulick et al.*, 2004; *Kopp et al*., 2000; *Moore et al*., 1990]. Balanced restorations of interpretations of fault geometry have constrained the development of these faults [e.g., *Adam et al.*, 2004; *Moore et al.*, 2011; *Morgan and Karig*, 1995; *Nemcok et al.*, 1999]. In complement to these geophysical interpretations, numerical models and scaled analog experiments capture the physics of accretion faulting and so have lent additional insight into fault mechanics at the deformation front [e.g., *Baba et al.*, 2001; *Buiter*, 2012; *Burbidge and Braun*, 2002; *Del Castello and Cooke*, 2007; *Graveleau et al.*, 2012; *Haq*, 2012; *Konstantinovskaia and Malavielle*, 2005, 2011; *Koyi and Cotton*, 2004; *Malavielle*, 2010; *McClay and Whitehouse*, 2004; *Miyakawa et al.*, 2010; *Mulugeta and Koyi*, 1992; *Naylor et al.*, 2005; *Persson and Sokoutis*, 2002; *Storti and McClay*, 1995]. Many previous studies have predicted the geometry of accretion faults using the conjugate failure planes that maximize Coulomb stress [e.g., *Mulugeta*, 1988; *Huiqi et al*., 1992], while fewer analyses have predicted this geometry through the optimization of energy components [*Cubas et al*., 2008; *Del Castello and Cooke*, 2007; *Maillot et al*., 2007; *Maillot and Koyi*, 2006; *Mary et al.*, 2013; *Maillot and Leroy*, 2003]. In particular, predictions of accretion thrust geometries using limit analysis, which identifies the active thrust geometry that produces the least upper bound in tectonic force

following the maximum strength theorem, closely match thrust geometries observed in physical experiments [*Cubas et al*., 2013; *Mary et al.,* 2013]. Additionally, numerical simulations of a physical accretion experiment suggest that the evolution of external work can shed insight on the growth of new accretionary thrusts [*Del Castello and Cooke*, 2007].

Del Castello and Cooke [2007] compare the efficiency of backthrust-forethrust pairs located at two different positions within a simulated accretion experiment, and find that the more efficient pair better matches the position of the observed pair. However, a more complete and systematic search for the most efficient position and dip of thrusts in an evolving physical accretion experiment has yet to be exacted. Additionally, the predictions of work optimization and Coulomb criteria have yet to be systematically compared. To address these gaps, we compare the predictions of external work optimization and Coulomb stress in numerical simulations of a physical accretion experiment to the fault geometries observed in the physical experiment.

In particular, we use work optimization to predict the geometry of accretion thrusts that develop in two stages of a physical accretion experiment: immediately before the development of the first and second backthrust-forethrust pairs. Within the work optimization framework, we predict that the fault configuration that produces the largest gains in efficiency, or the change in external work per new fault area, $\Delta W_{ext}/\Delta A$, will develop, rather than less efficient configurations. In order to identify the most efficient fault configuration, we compare $\Delta W_{ext}/\Delta A$ for numerical simulations that include faults at different positions and dips within the accretionary wedge. To assess the utility of the work optimization approach, we compare the geometry of the most efficient faults

predicted by work optimization to the geometry observed in the physical experiment and the fault geometry that maximizes Coulomb stress.

2.3. Growth of faults within accretionary wedges

Predictions of the geometry of accretionary faults using critical Coulomb wedge theory match many geophysical observations [e.g., *Adam and Reuther*, 2000; *Dahlen*, 1984, 1990; *Davis et al.*, 1983; *Davis and von Huene*, 1987; *Kopp and Kukowski*, 2003; *Lallemand et al.*, 1994; *Saffer and Bekins*, 2002; *Zhao et al.*, 1986]. This theory proposes that accretionary systems develop via the sequential outboard propagation of frontal thrusts until the angle between the wedge slope and basal surface attains a maximum, critical value [*Dahlen*, 1984; *Dahlen et al*., 1984; *Davis et al*., 1983]. After the system reaches this critical taper angle, the system slides stably on its basal detachment fault without internal deformation, such that every point within the wedge is at or on the verge of failure following the Coulomb failure criterion. Wedges with a taper angle lower than the minimum predicted angle (i.e., subcritical wedges) are predicted to develop thrust faults within the wedge that increase the taper angle (i.e., accretion), whereas wedges with a higher angle than the maximum predicted angle (i.e., supercritical wedges) are expected to develop normal faulting that reduce the angle [e.g., *Dahlen*, 1984; *Willette*, 1992; *Yuan et al.*, 2015].

The dips of new accretion thrusts in a critical Coulomb wedge depend on the orientation of the local principal stress [*Dahlen*, 1984; *Dahlen et al*., 1984; *Davis et al*., 1983]. Many experimental accretionary systems accommodate deformation via the outboard propagation of narrowly-spaced forethrusts [e.g., *Graveleau et al.*, 2012 and

references therein] and to the first-order follow critical Coulomb wedge theory. Episodic deviations from the steady-state behavior of critical Coulomb wedges have been demonstrated in many physical experiments where accretionary systems evolve through episodic cycles of 1) underthrusting, which causes wedge thickening and occurs via slip along existing thrusts, and 2) frontal accretion, which causes wedge lengthening and occurs through new accretion faulting at the front of the wedge [e.g., *Bigi et al*., 2010; *Buiter*, 2012; *Graveleau et al.*, 2012; *Gutscher et al*., 1996, 1998; *Haq*, 2012; *Konstantinovskaia and Malavielle*, 2005; *Malavielle*, 2010; *McClay and Whitehouse*, 2004; *Mulugeta and Koyi*, 1992; *Storti and McClay*, 1995]. Additionally, numerical models of accretionary systems [e.g., *Burbidge and Braun*, 2002; *Ellis et al*., 1999, 2004; *Wenk and Huhn*, 2013; *Yamada et al.*, 2014] and interpretations of crustal accretionary wedges [e.g., *Byrne and Fisher*, 1987; *Gutscher et al*., 1996; *Lallemand et al*., 1994; *Moore et al*., 1991; *Takami and Itaya*, 1996; *von Huene and Scholl*, 1991] suggest that accretionary systems develop faults through discrete, episodic processes rather than maintaining a critical state where the system is at failure everywhere.

Some analyses have used components of the system's energy budget to better understand accretion faulting and episodic deviations from critical Coulomb wedge theory [e.g., *Burbridge and Braun*, 2002; *Cubas et al*., 2008; *Del Castello and Cooke*, 2007; *Gutscher et al.*, 1998; *Hardy et al.*, 1998; *Mary et al*., 2013; *Souloumiac et al.*, 2009; 2010; *Yagupsky et al*., 2014]. These analyses have successfully used work optimization to predict the temporal evolution of accretionary systems, including the periodicity of the accretion-underthrusting cycle observed in analog experiments and inferred from seismic images of crustal accretionary wedge [*Gutscher et al*., 1998],

pulses of frontal accretion and underthrusting observed in numerical accretion simulations [*Burbridge and Braun*, 2002], and the outboard propagation of frontal accretion faults [*Hardy et al*., 1998]. Other analyses have used energy terms to predict the spatial distribution and geometry of accretion faults [e.g., *Cubas et al*., 2008; *Maillot et al*., 2007; *Maillot and Koyi*, 2006; *Del Castello and Cooke*, 2007; *Mary et al.*, 2013; *Yagupsky et al.*, 2014]. For example, *Mary et al.* [2013] use limit analysis to show that episodic accretion may be linked to slip weakening of the active faults, which is not considered in critical Coulomb wedge theory. In another study, *Del Castello and Cooke* [2007] investigate the evolution of the complete work budget of an accretionary system throughout a cycle of underthrusting and accretion.

Del Castello and Cooke [2007] use the complete work budget to shed insight on the transition from underthrusting to frontal accretion. This approach is more robust than considering only a subset of the work budget because individual components influence the energy budget to varying degrees throughout the evolution of the fault system [e.g., *Cooke and Madden*, 2014; *Del Castello and Cooke*, 2007]. The complete work budget includes the energy dissipated in internal strain or internal work of deformation, W_{int}, work of uplift against gravity, W_{grav}, work done against frictional sliding on faults, W_{fric}, energy required to created new fault area, W_{prop}, and energy of ground shaking, W_{seis} [e.g., *Cooke and Madden*, 2014]. Following the law of conservation of energy, the work consumed in the system must equal the total external work done on the boundaries of the system, W_{ext}:

$$W_{ext} = W_{int} + W_{grav} + W_{fric} + W_{prop} + W_{seis} \qquad \text{Eq. 2.1}$$

In a two-dimensional system, W_{ext} may be calculated from the sum of the products of shear traction and displacement, τ and u_s, and normal traction and displacement, σ_n and u_n, integrated over all of the model boundaries, B:

$$W_{ext} = \frac{1}{2}\iint_B (\tau u_s + u_n \sigma_n)\, dB \qquad \text{Eq. 2.2}$$

Within the work optimization framework, fault configurations that produce the maximum gain in W_{ext} per new fault area propagated, $\Delta W_{ext}/\Delta A$, are considered more likely to develop than less efficient fault configurations, which produce less $\Delta W_{ext}/\Delta A$ [*Cooke and Madden*, 2014]. This method provides a global approach for predicting fault geometry that assesses changes in the stress and displacement field far from the newly propagated fault (Eq. 2), and includes the contribution of all of the deformational processes that consume or produce work within the fault system (Eq. 1) [*Cooke and Madden*, 2014].

2.4. Methods

We simulate two stages of new fault growth observed in physical accretion experiments performed at the Université de Cergy-Pontoise (UCP) tectonic modeling lab with numerical models that replicate the moving wall and basal displacements observed in the experiment. To assess the utility of the work optimization approach, we compare the geometry of the most efficient faults predicted by work optimization to the geometry observed in the physical experiment, and the geometries predicted by Coulomb stress.

2.4.1. Physical experiment

For the accretionary experiment E240 performed at UCP, dry sand was deformed in a rectangular box with a fixed frontwall, basal plate and sidewalls [*Herbert et al*., 2015]. To simulate accretion, an electric screw motor translates the backwall of the box towards the frontwall at a constant speed. Throughout the duration of the experiment, a camera captures photos of the cross section of the wedge through the box's glass sidewall every five seconds. To construct the sandpack, a sedimentation device, designed and built at UCP, sieves the sand two or three times before deposition [*Maillot*, 2013]. The sand deposition method strongly controls the frictional properties of the system, and thus how the sandpack accommodates strain [e.g., *Krantz,* 1991; *Lohrmann et al.*, 2003; *Maillot*, 2013]. The UCP sedimentation device produces very homogeneous, isotropic and dense sandpacks consisting of planar layers [*Maillot*, 2013]. This homogeneous sandpack enables robust comparison of the thrust geometry observed in the physical experiment and the geometry predicted in the numerical analysis.

The early episodes of fault development in this physical experiment include 1) the horizontal propagation of the basal detachment fault, 2) the formation of the first backthrust-forethrust pair near the outboard tip of the detachment, 3) the propagation of a second backthrust ~10 mm closer to the backwall than the first pair, 4) the propagation of a second forethrust ~10 mm outboard of the first pair, and 5) the development of a second backthrust-forethrust pair ~60 mm beyond the active thrust [*Herbert et al*., 2015]. Preceding the development of each new forethrust, the detachment fault propagates outboard of the pre-existing thrusts, and a diffuse region of shear strain and dilation

develops above the detachment tip. After the first forethrust-backthrust pair develops, the backthrust is progressively translated within the hanging wall of the forethrust as slip accumulates along the forethrust. After the root of the first backthrust has been uplifted sufficiently so that it no longer intersects the basal detachment, the second backthrust develops. The second backthrust forms a new pair with the first forethrust, with the root of this pair at the detachment. At this stage, the first backthrust ceases to accommodate slip, and the second backthrust slips until after the development of the second forethrust-backthrust pair. Before the development of the new thrust pair, the detachment propagates and slips ~10 mm beyond the root of the first forethrust and second backthrust, and the second forethrust forms near the outboard extent of the detachment. Similar to backthrust development, after the second forethrust propagates, slip along the first forethrust ceases, and the second forethrust slips until the development of the second pair. With onset of the second forethrust, the second backthrust adjusts its geometry slightly so that it roots into the detachment at the same point as the second forethrust. The second forethrust-backthrust pair forms following a second episode of detachment propagation and slip that extends ~60 mm beyond the active forethrust. This distance is significantly farther than the extent of detachment propagation that precedes the development of the second forethrust.

We calculate the incremental displacement field of the wedge cross-section with digital image correlation (DIC) of sequential photos captured in the experiment. For every two sequential photos of the wedge cross-section, we use Particle Image Velocimetry analysis to determine the instantaneous velocity field at a grid of points through the DIC of pixel constellations [*Adam et al*., 2005; *Hoth*, 2005]. In order to

highlight the rotation of material that indicates the development of discrete thrusts, we use the velocity field to calculate the incremental curl field between successive images. High rotation rates (e.g., curl) highlight localized slip along faults. We calculate the curl field of the velocity field, ***U***, from the cross product of the gradient operator with the velocity vector, ***U***:

$$\nabla x U = \left(\frac{\partial U_y}{\partial x} - \frac{\partial U_x}{\partial y}\right)\hat{z} \qquad \text{Eq. 2.3}$$

where *x* is the horizontal direction, *y* is the vertical direction, and *z* is the out-of-plane direction.

The incremental horizontal displacement and incremental curl fields reveal the geometry of the first and second backthrust-forethrust pairs, which meet the base of the experiment at 65±7 mm and 114±6 mm, respectively, from the physical backwall (Fig. 2.1). The thrust faults are illuminated by both sharp gradients in the horizontal velocity (or incremental displacement) field, which correspond to high strain in the horizontal direction, and by elevated regions of curl, which indicate enhanced rotation of sand and higher shear strain. The range in the reported observed positions arises from the width of regions of elevated curl that span multiple millimeters around each thrust (supp. Fig. 2.1). We observe the development of the first and second backthrust-forethrust pairs after about 3 mm and 37 mm of backwall displacement, which are captured in the 16th and 48th incremental displacement fields**.**

In this study, we search for the optimal geometry of new planar thrusts within the first and second forethrust-backthrust pairs. We focus on these two stages, and not on the

intervening stages of single forethrust and backthrust growth, because at these stages of the experiment the wedge undergoes the most significant reorganizations in active fault configuration with the development of and slip along two new thrust faults. Additionally, searching for the optimal geometry of thrusts in the second backthrust-forethrust pair provides insights into the tradeoffs of continued slip along pre-existing faults versus propagation of entirely new thrusts. Simulating these stages of wedge development allows the direct comparison of the gain in efficiency due to forethrust or backthrust propagation.

2.4.2. Development of numerical simulation of the physical experiment

We simulate the UCP accretion experiment with the two-dimensional, plane strain, linear elastic, Boundary Element Method (BEM) modeling tool Fric2D [*Cooke and Pollard*, 1997]. Fric2D solves the quasi-static equations of deformation to determine the displacements and tractions on each element and at specified points within the model, produced by a given set of boundary conditions and fracture geometry [e.g., *Cooke and Pollard*, 1997; *Cooke and Murphy*, 2004; *Cooke and Madden*, 2014]. The BEM approach of Fric2D only requires the discretization of fractures and boundaries, which are comprised of linear elements that may not interpenetrate. Additionally, Fric2D 3.2.7 can simulate slip-weakening behavior along pre-existing fractures and/or potential growth elements [*Savage and Cooke*, 2010]. When an element slips beyond a prescribed slip-weakening distance, the coefficient of friction along that element evolves linearly from its static to its sliding value.

The Fric2D numerical models employed here simulate increments of deformation of the cross section of the physical wedge observed through the glass sidewalls. To simulate the increments of deformation, we derive the horizontal and vertical displacements observed along the moving backwall and just above the base of the experiment near the physical detachment, and apply these displacements to the corresponding boundaries of the numerical model. In this process, we first calculate the incremental displacement field before the first and second backthrust-forethrust pairs form (Fig. 2.1). Next, we take a transect of the horizontal and vertical components of the displacement field 1.42 and 1.21 mm above the base of the model, for the first and second stages of faulting, respectively (Fig. 2.2A-D). We select the transect depth so that it is as close as possible to the sliding detachment fault along the base of the model (Fig. 2.1), but avoids significant artifacts in the PIV data that occur along the base of the sandpack.

To reduce noise in the displacements, we run a fifteen-point median filter on the raw displacements in order to remove outliers. Then we calculate the five-point central moving average of the filtered displacements, which reduces noise with wavelengths less than two millimeters and preserves larger scale fluctuations in the displacements (Fig. 2.2E-F). Because Fric2D employs Eulerian deformation, the maximum boundary displacements should be less than half of the element size, which for these models is 1 mm. Consequently, the smoothed incremental displacements observed in the physical experiments are scaled by approximately one-half so that the maximum horizontal displacement is 0.50 mm. Using larger elements could permit the application of larger horizontal displacements, but has the undesirable effects of decreasing both the resolution and accuracy of the numerical solution. As long as the increment of displacement is

sufficiently large to cause frictional slip along the faults within the model, then the relative efficiency of a particular thrust geometry compared to other thrusts remains unchanged regardless of the magnitude of applied displacements, causing the optimal thrust geometry of a models that differ only in the magnitude of the applied displacements to remain the same. For these numerical simulations, the scaled displacements are sufficient to cause slip along faults that dip within 20° of the observed thrusts and are located within 30 mm of the observed thrusts, allowing assessment of the gain in efficiency of a broad range of fault geometries near the observed. The vertical displacements are scaled by the same ratio as the horizontal displacements. We apply the scaled horizontal and vertical displacements of the physical experiments to the base of the numerical model so that the applied boundary conditions simulate the vertical and horizontal displacements associated with slip along the detachment fault within the physical experiment. Consequently, these models do not simulate detachment deformation via slip along a frictional fault. However, the frictional work of the experimental detachment is captured in the modeled external work because the total external work on the numerical model is comprised of the work done on the backwall as well as that done on the basal boundary, which simulates the displacements of the detachment (Eq. 2). We apply displacements to these model boundaries, and Fric2D solves for the tractions on the boundaries required to achieve the applied displacements.

We apply the maximum basal horizontal displacement (0.5 mm) as the rightward normal displacement, u_n, on the left model boundary to simulate the translation of the backwall (Fig. 2.2D). We set shear tractions, τ=0, on this boundary, so that material at its contact is free to displace vertically. We prescribe zero normal displacements, u_n=0, and

shear tractions, τ=0, to the rightmost model boundary so that it does not translate horizontally. Allowing the left and right model boundaries to displace vertically enables the thickening of the sandpack near the backwall, such as observed in this physical experiment, as well as other physical accretion experiments [*Souloumiac et al.*, 2010]. We allow the top boundary of the model following the topography of the experiment to deform freely, such that this boundary experiences zero normal and shear tractions, σ_n=τ=0. Because each model boundary experiences some displacement or traction, each boundary of the model may contribute to the total external work of the system. Boundaries with zero-valued components of applied tractions or displacement do not contribute to the external work (Eq. 2). Consequently, the external work of these accretion models depends on the resulting normal tractions on the left side of the model, the modeled moving backwall, B_a, as well as the shear and normal tractions along the base of the model, the modeled detachment, D, so that Eq. 2 may be expressed as

$$W_{ext} = \frac{1}{2}\iint_D (\tau u_s + u_n\sigma_n)\, dD + \frac{1}{2}\iint_{B_a}(u_n\sigma_n)\, dB_a \qquad \text{Eq. 2.4}$$

We use the topography of the physical wedge at the two stages of interest within the experiment as the geometry of the top boundary of the models. Measurements of the dry CV32 sand used in the experiment constrain the material and fault properties (i.e., Young's modulus, density, static and dynamic friction) of the models [e.g., *Cubas et al.*, 2010; *Herbert*, 2014; *Lambe and Whitman*, 1969; *Maillot*, 2013]. Table 2.1 lists the intact material and fault properties used in the models simulating the physical experiments.

The applied loading conditions, material properties, and wedge geometry produce displacement fields within the numerical simulation that share first-order patterns with the observed displacement fields (Fig. 2.2). In the first stage of faulting, the incremental horizontal displacements of the physical experiment, and within the numerical simulation, gradually decrease with distance from the backwall. The incremental vertical displacements show a wide region of uplift from about 50-100 mm from the backwall in both the physical experiment and the simulation. In the second stage of faulting, the simulation produces a horizontal displacement field that is very similar to the pattern of the observed incremental horizontal displacements. The regions of the wedge between the pre-existing thrusts, and between the backwall and the pre-existing backthrust, move to the right as relatively coherent blocks without significant horizontal compaction (i.e., without large gradients in horizontal displacement). Additionally, the horizontal displacements within the portion of the wedge outboard of the pre-existing forethrust gradually decrease with increasing distance from the backwall. Furthermore, the simulation produces a broad region of uplift extending from about 80-120 mm from the backwall that matches the region of incremental vertical uplift within the experiment. In both the numerical simulation and the physical experiment, vertical uplift is greatest within the wedge between the pre-existing thrust faults.

2.4.3. Work optimization approach

To investigate the impact of accretion faulting on the mechanical efficiency of the accretionary wedge, we calculate the change in external work per fault area, $\Delta W_{ext}/\Delta A$, produced by new faults at systematically varying positions and dips within the wedge.

The fault geometry that produces the largest $\Delta W_{ext}/\Delta A$ is considered the most efficient, and thus most likely to develop according to work optimization principles [e.g., *Cooke and Madden*, 2014]. We use the ratio $\Delta W_{ext}/\Delta A$ to determine the most efficient geometry because faults with longer lengths, and thus larger areas, can accommodate more slip and so produce greater ΔW_{ext} than shorter faults [e.g., *Cooke and Madden*, 2014; *McBeck et al*., 2016]. While the growth of longer faults results in more efficient systems, the growth of these faults also consumes greater work in the production of new fault surface area [e.g., *Chester et al*., 2005; *Wilson et al*., 2005; *Herbert et al*., 2015]. For this study, we are interested in faults that provide the greatest increases in efficiency relative to the cost of creating the fault surface. The reported gain in efficiency indicates the increase in system efficiency (ΔW_{ext}) per change in fault area, ΔA, of one meter-squared because $\Delta W_{ext}/\Delta A$ incorporates the fact that systems with more fault area can accommodate greater slip. Consequently, $\Delta W_{ext}/\Delta A$ reveals fault geometries that are efficient relative to the cost of propagating new fault area. We calculate fault area from simulated fault length as Fric2D simulates a 2D, plane strain environment in which the model is one unit thick in the z-direction. For the analysis employed here, the change in fault area, ΔA, is the difference in total fault area following the addition of a new fault to the model, which is the area of the newly added fault.

We compare the efficiency of faults within the stages of wedge development in which the first and second backthrust-forethrust pairs form. The modeled faults root at the model base and intersect the top boundary of the model in a similar manner to the observed faults in the physical experiments. In the first stage of fault growth investigated, we predict the geometry of thrusts in the first backthrust-forethrust pair. Prior to addition

of the new faults, only gravitational work and internal work contribute to the work budget of the numerical wedge. After the first pair develops, frictional work also contributes to the work budget. In the second stage of fault growth investigated, we predict the geometry of the second backthrust-forethrust pair and investigate the influence of the new fault geometry on system efficiency that contains pre-existing faults, which accommodate slip immediately before the second pair develops (Fig.1). With these wedge simulations, we are able to investigate the changes in efficiency due to new fault growth, as well as the abandonment of active faults, and the related tradeoffs of continued slip on a pre-existing structure or propagation and slip on a new structure.

In the analysis of the first stage of thrust faulting, we vary the position and orientation of each new fault and calculate the $\Delta W_{ext}/\Delta A$ due to faults that root at the model base from 49 to 111 mm from the backwall, in increments of 2 mm, and orientations from 20° to 170° in increments of 2°. Reported orientations are measured clockwise from the left horizontal. With this sign convention and model design, faults oriented 0-90° are backthrusts, and 90-180° are forethrusts. The tested range of fault positions and orientations includes the approximate positions of the backthrust (65±7 mm) and forethrust (65±5 mm), and dips of the backthrust (45±10°) and forethrust (156±4°) observed in the physical experiment (supp. Fig. 2.1). In the analysis of the second stage of thrust faulting, we vary the position of faults from 80 to 138 mm from the backwall, in increments of 2 mm, and the orientations from 20° to 170°, in increments of 2°. These ranges include the approximate observed positions of the backthrust (114±6 mm) and forethrust (114±5 mm), and orientations of the backthrust (38±5°) and forethrust (156±3°) (supp. Fig. 2.1). For some of the fault geometries tested in the second stage

analysis, the added fault intersects the pre-existing forethrust. In these scenarios, we shorten the new fault so that it ends at the pre-existing forethrust. We assume that if a new fault intersects the pre-existing forethrust, the most efficient fault will terminate at the thrust. For example, in the physical experiment, the second forethrust-backthrust pair does not intersect the pre-existing forethrust. For this study, we presume that the thrusts that maximize $\Delta W_{ext}/\Delta A$ will form sufficiently outboard of the pre-existing thrusts such that they do not intersect or terminate at the pre-existing forethrust.

2.4.4. Coulomb failure planes and stress analysis

To evaluate the utility of the work optimization approach over traditional fault predictions, we compare the orientation of the most efficient faults to the orientations of fault planes that maximize Coulomb stress. For this comparison, we calculate the Coulomb stress along each potential fault over a range of dips at the position that matches the observed fault geometry. Using a tension positive sign convention, Coulomb stress, S_c, may be calculated from the shear traction, τ, the coefficient of internal friction, μ, and the normal traction, σ_n, as

$$S_c = |\tau| + \mu\sigma_n \qquad \text{Eq. 2.5}$$

In order to calculate Coulomb stress, we find the shear and normal tractions along potential fault planes prior to any slip or opening along those planes. Coulomb shear failure of those planes occurs when the Coulomb stress exceeds the inherent shear strength of the material. In this comparison of Coulomb stress and work optimization, we

load the numerical models such that a range of potential fault plane orientations fail in shear. If we reduced the applied loading so that only one of the potential faults failed, we would not be able to observe the sensitivity of ΔW_{ext} to orientation of the potential faults. While lower and higher loading would reduce and increase the values of the Coulomb stress and ΔW_{ext} respectively, the value along each potential fault plane relative to alternative planes is independent of degree of loading.

To compare the orientations of planes that maximize Coulomb stress with the work optimization predictions, we calculate both the average and maximum Coulomb stress along modeled faults prior to slip along those faults. In this comparison of Coulomb stress and work optimization predictions, faults that produce the maximum $\Delta W_{ext}/\Delta A$ are considered likely to develop before (e.g., under less applied loading) less efficient faults, and planes with high Coulomb stress are considered likely to fail before planes with lower stress. In this analysis, the potential fault planes that host high Coulomb stress would fail under lower applied displacements than fault planes that host lower Coulomb stress.

2.5. Results

We present the results of this work optimization analysis by first comparing the results of the first stage of faulting to the second stage of faulting. Then we compare the numerical predictions of highly efficient faults to the fault geometries observed in the physical experiment, and to the fault dips predicted by Coulomb stress. Following the results of these investigations, we search for the most efficient backthrust geometry in a system that includes the observed forethrust geometry. To shed insight on the evolution

of system efficiency, and the tradeoffs among the deformational processes that consume or produce work throughout wedge development, we analyze the components of the system work budget by tracking the evolution of the external, internal, frictional and gravitational work.

2.5.1. Comparison of first and second stages of faulting

Systematic investigation of external work for a wide range of single fault position and dip reveals that both stages of accretion produce two highly efficient thrust geometries, one forethrust and one backthurst for each stage (Fig. 2.3). The condition numbers of all model results, which indicate the reliability of the numerical solution, are reported in supplemental Fig. 2.2. Models with anomalously high condition numbers, that exceed 125% of the mode, are considered unreliable and removed from the search for the most efficient thrust geometry (supp. Fig. 2.2). The maximum $\Delta W_{ext}/\Delta A$ of the second stage of faulting (10.99 mJ/m^2) is only ~25% of the optimal gain in efficiency of the first stage (43.87 mJ/m^2), suggesting that fault propagation leads to successively smaller gains in efficiency throughout the development of the wedge. The maximum $\Delta W_{ext}/\Delta A$ of the second stage is likely lower than that of the first stage because slip along pre-existing thrusts in the later stage contributes to W_{ext} both before and after fault development.

2.5.2. Comparison of predicted and observed thrust geometry

In order to thoroughly assess the fault predictions of work optimization, we compare the observed thrust geometry in the physical experiment to the most efficient thrust and the range of thrusts geometries that have high efficiency (Fig. 2.4). Because small scale

material heterogeneities may cause faults to deviate from the precise prediction of the most efficient thrust geometry, we compare the observations to high-efficiency thrusts that produce >90% of the local maximum $\Delta W_{ext}/\Delta A$. If the high-efficiency thrusts do not overlap the experimental observations, then we also consider moderately high-efficiency thrusts that produce >80% of the local maximum $\Delta W_{ext}/\Delta A$. The black contour lines overlaid on the full suite of numerical simulations (Fig. 2.3) are 10% intervals relative to each local maximum $\Delta W_{ext}/\Delta A$. Consequently, the extent of the high-efficiency and moderately high-efficiency thrusts may be extracted from Fig. 2.3. To directly compare the observed to the predicted thrust geometry, we overlay the extent of these efficient thrusts on the incremental shear strain field of the associated stages of the experiment (Fig. 2.4).

For the first stage of faulting, the dip and location of the high-efficiency forethrusts (>90%) completely overlaps the observed forethrust, whereas the dip and location of the high-efficiency backthrusts only partly overlaps the geometry of the observed backthrust in the physical experiment (Fig. 2.4). In particular, the observed backthrust dips 45±10°. The most efficient predicted backthrust dips 32°, and the range of dips of high-efficiency backthrusts is 26-40°. The observed forethrust orientation is 156±4° (dip of 24°). The most efficient forethrust orientation is 154° (dip of 26°), and the range of orientations of high-efficiency is 146-160°. The observed position of the root of the forethrust-backthrust pair is 65±6 mm from the moving wall. The predicted position of the most efficient forethrust is 71 mm, and the range of positions of high-efficiency forethrusts is 63-75 mm. In contrast to the agreement of the observed and predicted most efficient forethrust position, the predicted position of the most efficient backthrust is 87 mm, and

the range of positions of high-efficiency and moderately high-efficiency backthrusts is 81-93 mm and 77-101 mm, respectively. Consequently, the lower bound of the range of moderately high efficiency (80%) backthrust positions (77 mm) differs from the observed position (65±6 mm) by more than 5 mm. The range of backthrusts that overlap the observed backthrust position produce 60% of the local maximum $\Delta W_{ext}/\Delta A$. This work optimization analysis predicts the forethrust position, and backthrust and forethrust dips with success, but predicts the backthrust position less precisely.

The analysis of the second stage reveals that the dips of high-efficiency forethrusts and backthrusts (>90% of the maximum $\Delta W_{ext}/\Delta A$) both match the observed thrust dips (Fig. 2.4C-D). The observed backthrust dips 38±5°. The predicted most efficient backthrust dips 30°, and the high-efficiency backthrusts range in orientation from 20 to 40°. The observed forethrust orientation is 156±3°; the predicted most efficient forethrust orientation is 158° (dip of 22°), and the high-efficiency forethrusts range in orientation from 148 to 168°. Similarly, the positions of the high-efficiency thrusts closely match the observed positions. The observed position of the root of the forethrust-backthrust pair is 114±5 mm from the moving wall. The predicted position of the most efficient backthrust is 122 mm, and the high-efficiency backthrusts range in position from 116 to 126 mm. The predicted position of the most efficient forethrust is 98 mm, and the range of positions of high-efficiency and moderately high-efficiency forethrusts is 94-102 mm and 86-114 mm, respectively. The high-efficiency geometries that produce >90% of the maximum $\Delta W_{ext}/\Delta A$ overlap most of the observed positions and dips of the second forethrust-backthrust pair: the high-efficiency backthrust geometries completely overlap

the observed backthrust, and the high-efficiency forethrust geometries overlap the upper two-thirds of the observed forethrust.

In the first stage of faulting, the basal location of the most efficient backthrust does not match the basal location of the most efficient forethrust. Consequently, when their development is considered independently, the predicted backthrust and forethrust intersect, and do not form a commonly rooted forethrust-backthrust pair. This mismatch of the position of the most efficient thrusts suggests that the optimal geometry of thrusting may differ if our analysis searched for the optimal pair location and set of orientations, rather than a single optimal thrust geometry. Although the backthrust is generally shorter-lived than the forethrust, the backthrust may play an important role in the location of forethrust-backthrust pair development. Using the kinematic approach of limit analysis to predict the position and dips of the active forethrust-backthrust pair has lent insight into the evolution of thrusting in accretionary systems [e.g., *Mary et al.,* 2013].

2.5.3. Comparison of Coulomb analysis and work optimization

To compare the orientations of planes that maximize Coulomb shear stress with the work optimization predictions, we calculate both the average and maximum Coulomb stress along each fault of different orientation at the observed basal position of thrust development before the fault slips. This comparison reveals that the fault orientation that produces the maximum of the average Coulomb stress more closely matches the observed faulting than the orientation of the fault that hosts the maximum Coulomb stress (Fig. 2.5).

In the first stage of faulting, the fault orientations that maximize the average Coulomb stress along the fault are within 2˚ of the orientation of faults with greatest efficiency (Fig. 2.5A-B). Furthermore, the backthrust orientation that maximizes $\Delta W_{ext}/\Delta A$ (40˚) equals the backthrust orientation that maximizes the average Coulomb stress. In the second stage of faulting, the fault orientations that maximize the average Coulomb stress along the fault differ by less than 4˚ from the orientations of the backthrust and forethrust that maximize $\Delta W_{ext}/\Delta A$ (Fig. 2.5E-F). This suggests that the faults that accommodate deformation most efficiently are those that have highest average Coulomb stress before slipping. However, when considering the onset of failure, we generally presume that the plane that hosts the maximum Coulomb stress is most likely to initiate and grow into a through-going fault. The orientations of the fault plane with maximum Coulomb stress disagree with work optimization predictions and fall outside of the observed orientations for the backthrusts and forethrusts at both stages of fault development. In the first stage of faulting, the orientations of the backthrust and forethrust that host the maximum Coulomb stress differ 12˚ and 6˚, respectively, from the most efficient, and 17˚ and 4˚, respectively, from the observed. In the second stage of faulting, the orientations of the backthrust and forethrust that maximize Coulomb stress differ 12˚ and 10˚, respectively, from the most efficient, and 10˚ and 9˚, respectively, from the observed.

In the first stage of faulting, the region of highest Coulomb stress indicating where incipient faults may initiate differs between the backthrust and forethrust. For the backthrusts, highest Coulomb stress occurs near the top of the wedge and near the inflection of the wedge topography because local differential uplift near the inflection promotes shear along thrusts (Fig. 2.5A). For the forethrusts, the highest Coulomb stress

develops near the base of the wedge because the lithostatic stress is highest at the base, and the resulting pre-failure normal tractions on forethrust segments near the base are also maximized (Fig. 2.5A). This Coulomb stress distribution suggests that new backthrusts may initiate near the top of the wedge, whereas new forethrusts may initiate near the base. In contrast, in the second stage of faulting, the highest Coulomb stress along both backthrusts and forethrusts arises near the wedge base, indicating that new thrust faults may initiate near the base (Fig. 2.5E).

The initiation of thrusts within physical accretion experiments has been documented with high temporal resolution to reveal shear bands that form prior to localization along a single thrust [*Bernard et al.*, 2007; *Dotare et al.*, 2016] These transient shear bands tend to have uniform slip, however, some shear bands accommodate greater slip near the wedge base [*Bernard et al.*, 2007; *Dotare et al.*, 2016], while others only slip near the top of the sandpack [*Dotare et al.*, 2016]. These differing patterns of shear strain suggest that incipient thrusts may propagate both upwards and downwards within the wedge. Similarly, our calculation of Coulomb stress along potential thrusts indicates that incipient thrusts may initiate near the top of the wedge, such as backthrusts in the first stage of faulting, or near the base of the wedge, such as forethrusts in the first stage, and both thrusts in the second stage. The mismatch between the planes with largest Coulomb stress and the experimental observations suggests that while faults may initiate at regions of highest Coulomb stress, the overall development of the fault follows the surface that has greatest average Coulomb stress, which produces the most efficient fault geometry.

In addition, the agreement between the maximum average Coulomb stress and the efficient thrust geometry is consistent with the fact that work optimization is a global

approach that considers the stress state throughout the system. The average Coulomb stress considers the stress state along the length of the fault, rather than just the portion of the fault that hosts the maximum Coulomb stress. Consequently, the work optimization approach is more similar in scope to the average Coulomb stress than the maximum Coulomb stress, and so average Coulomb stress is likely to produce more similar predictions to work optimization than the maximum Coulomb stress.

2.5.4. Forethrust development precedes backthrust

The work optimization approach of this study closely predicts the geometry of many of the observed thrusts (Fig. 2.4). However, for the first stage of faulting, the range of backthrusts that produce >90% of the maximum backthrust $\Delta W_{ext}/\Delta A$ does not completely overlap the observed backthrust position. The discrepancy between the position of the predicted and observed backthrust may result from independently searching for the optimal backthrust geometry in a system that does not already include an active forethrust. The incremental displacement and shear strain fields of the experiment reveal that shear strain localizes along a discrete forethrust-verging structure slightly before the backthrust fully forms (Fig. 2.1). Furthermore, after the forethrust and backthrust both develop, the forethrust accommodates greater slip than the backthrust, suggesting that the forethrust acts as the dominant fault (Fig. 2.1).

To determine if slip along the first forethrust promotes backthrust development, we search for the efficient geometry of the backthrust in a numerical wedge that represents the first stage of faulting immediately after the first forethrust develops. In this analysis, we compare $\Delta W_{ext}/\Delta A$ due to the development of backthrusts within the hanging wall of

the forethrust, with dips from 30-90° and basal positions from 39-65 mm, in increments of 2° and 2 mm, respectively. The model boundary geometry, and material and fault properties are identical to those values used in the analysis of the first stage of faulting (Fig. 2.2, Table 2.1). However, whereas in the first analysis we use displacements observed in DIC increment 15, in this new analysis the loading conditions represent the increment of the experiment immediately after the first forethrust develops, DIC increment 16 (Fig. 2.6).

This analysis reveals that the optimal backthrust forms a pair with the pre-existing forethrust, and intersects the root of the forethrust (Fig. 2.6F). The range of backthrust geometries that produce >90% of the maximum $\Delta W_{ext}/\Delta A$ completely overlaps the region of high shear strain along the backthrust in the physical experiment. The improved prediction of the backthrust geometry in the system that includes the active forethrust suggests that deformation along the young forethrust promotes backthrust development, ultimately forming a backthrust-forethrust pair.

The Coulomb stress along the backthrusts also sheds insight on the potential for backthrust development after forethrust growth. When the forethrust is included in the wedge, the orientation of the backthrust that maximizes average Coulomb stress differs 4° from the most efficient (Fig. 2.7). Similar to the first and second stages of faulting analysis, the orientation of the backthrust with maximum Coulomb stress differs from the most efficient backthrust orientation by a greater magnitude than the backthrust with the maximum of the average Coulomb stress, differing by 18° from the most efficient. This result suggests that faults may initiate in regions of maximum Coulomb stress, and then

propagate in the direction that maximizes the average Coulomb stress along the fault, which also produces high $\Delta W_{ext}/\Delta A$ for the fault system.

2.5.5. Evolution of efficiency

Comparing the evolution of the wedge's overall efficiency through the development of the first and second forethrust-backthrust pairs sheds additional insight into the influence of fault geometry on the mechanical efficiency of the accretionary system. In these numerical models, which have applied displacement loading on the boundaries, high external work (Eq. 2) indicates models with inefficient fault geometries that require greater tractions along the model boundaries to accommodate the applied displacement than models with more efficient geometries. Consequently, efficient fault configurations have greater slip along faults and less off-fault deformation. Because the magnitude of the external work required by the system depends on the applied displacements, the absolute values of external work are not as significant as the differences in external work between models with equivalent applied displacements. To shed insight on the evolution of system efficiency, and the tradeoffs of the deformational processes that consume or produce work throughout fault development, we calculate the external, internal, frictional, and gravitational work of wedge simulations with various observed fault configurations and applied displacements (Fig. 2.8).

For this analysis of work budget, we use fault geometries that match the observed active geometries at various stages before and after the first and second thrust pairs develop (Fig. 2.8). The applied displacements of the earliest wedge simulations (systems 0-3) are derived from the displacements observed immediately before the development of

the first thrust pair (DIC 15). The displacements of the next wedge simulation (system 4) uses the observed displacement immediately after the first thrust pair develops (DIC 16). To explore the second stage of faulting, the applied displacements of systems 5-8 simulate the displacements observed immediately before the second pair develops (DIC 47). The displacements of the most mature wedge simulation (system 9) uses the displacements observed immediately after the second thrust pair develops (DIC 48).

Before any faults develop in the wedge, the system is the least efficient and requires the greatest external work to accommodate the applied displacements (Fig. 2.9, system 0, W_{ext}=12.78 mJ). The development of either the forethrust or backthrust leads to increases in efficiency (i.e., reduction in boundary tractions and subsequent external work) from the initial external work of the system. Backthrust development produces a slightly larger gain in efficiency, ΔW_{ext}, (0.81 mJ) than forethrust development (0.58 mJ) because the backthrust (system 1) has less slip, and so the wedge consumes commensurately less work in frictional sliding, W_{fric}, and work done against gravity, W_{grav}, than in the wedge with the forethrust (system 2). Although the work consumed in off-fault deformation or internal work, W_{int}, is smaller in the wedge that includes the forethrust, the W_{fric}+W_{grav} of the wedge including the forethrust is greater than the W_{fric}+W_{grav} of the system with the backthrust. The higher $\Delta W_{ext}/\Delta A$ of the backthrust (28.40 mJ/m^2) compared to the forethrust (14.22 mJ/m^2) suggests that the gain in efficiency due to forethrust development is small relative to the cost of creating new fault at this stage of faulting.

The development of the first backthrust-forethrust pair (system 3) increases the efficiency of the system to an even greater extent than the backthrust or forethrust alone, requiring only 12.20 mJ of W_{ext}. More significantly, the wedge requires the least external

work to accommodate the applied displacements when the wedge includes the first pair, and the loading conditions simulate the observed displacements immediately after that pair develops (system 4, 11.39 mJ). System 4 more closely represents the physical wedge after the development of the first pair than system 3 because the development of the new thrust pair is associated with advancement of the basal detachment, which is reflected in the basal displacements simulated in system 4 (observed within DIC 16). In the numerical wedges, updating the applied displacements promotes slip along the new thrust pair, increases W_{grav} by 0.54 mJ, increases W_{fric} by 1.70 mJ and decreases W_{int} by 5.45 mJ from the initial system. Although both W_{fric} and W_{grav} increase after updating the displacements, the reduction in W_{int} is sufficient to reduce the total W_{ext} of the system. At this stage of fault development, the magnitude of ΔW_{int} is greater than $\Delta W_{fric}+\Delta W_{grav}$, and consequently, the reduction in off-fault deformation associated with fault development dominates the change in system efficiency.

In the second stage of faulting, the addition of new thrust faults produces smaller gains in efficiency than the first stage in part because the pre-existing thrusts continue to slip before and after thrust development in the second stage (Fig. 2.8). In particular, after the second backthrust-forethrust pair develops, and while the applied displacements simulate the displacements observed preceding new fault development (system 8), the total slip summed over the length of the thrusts in the second pair (102 mm) is only 28% of the slip along the pre-existing thrusts (363 mm) in the wedge. Updating the applied displacements to the basal displacements observed just after the new thrust pair develops (system 9) increases the total summed slip along the second pair to 310 mm, and decreases the total slip along the pre-existing pair to 134 mm.

In contrast to the first stage of faulting, in which the backthrust is slightly more efficient than the forethrust, in the second stage of faulting, forethrust development produces a larger gain in efficiency, ΔW_{ext}, (0.21 mJ) than backthrust growth (0.023 mJ) because less work is done in off-fault deformation in the wedge with the forethrust (system 7) than in the wedge with the backthrust (system 6). Applying the displacements observed in the increment of the experiment immediately following the development of the second pair (system 9) promotes slip along the new backthrust and forethrust and reduces slip along the pre-existing pairs, which reduces the W_{fric} of the system, and consequently reduces the total W_{ext}. New fault development in the second stage does not produce reductions in W_{int} that are as large as those in the first stage because the faults in the pre-existing pair continue to slip, causing regions of high off-fault deformation to persist around those faults (system 9, Fig 8; supp. Fig. 2.3).

2.6. Discussion

The work optimization approach used in this study provides insight into several key stages of wedge development. Here, we discuss the temporal sequence of faulting within and between the two stages of faulting that is illuminated by the analysis of the evolving work budget components. We contrast the sensitivity of efficiency to forethrust position in the first and second stages of faulting. We also compare our numerical estimates of external work to physical measurements of external force on the accretion experiment.

2.6.1. Efficiency evolution of numerical and physical experiment

Before the second backthrust-forethrust pair develops (Fig. 2.8, system 5), the external work of the modeled system is higher than the model representing the conclusion of the first stage of faulting (system 4) (Fig. 2.9A). This result is consistent with external force measurements from the physical experiments that show increasing force on the moving wall between episodes of fault growth (Fig. 2.10) [*Cruz et al*., 2010; *Cubas et al.*, 2010; *Souloumiac et al*., 2012; *Herbert et al*., 2015]. Through an analysis of the components of the work budget, *Del Castello and Cooke* [2007] show that thickening between accretion episodes increases the frictional work on the detachment, which subsequently increases the external work. Consistent with the findings of *Del Castello and Cooke* [2007], the increased overburden thickness at the second stage of forethrust-backthrust development produces greater frictional work on the existing faults within the wedge. Our models do not include the frictional work along a sliding detachment, which might also contribute to the frictional work of the experimental system. In our simulations of this experiment, the detachment work is captured in the external work, which is calculated from the tractions along the backwall and basal boundary required to produce the applied backwall and basal displacements (Eq. 2).

The gain in efficiency (ΔW_{ext}) due to the development of the second pair (system 9) is smaller than that gain due to the development of the first pair (system 4). Consistent with this numerical result, the force measured on the backwall throughout the physical accretion experiment reveals a greater drop associated with the development of the first pair, than the second (Fig. 2.10). Within the numerical simulation, the ΔW_{ext} due to the development of the second thrust pair (system 9) is smaller than the first pair (system 4) because the pre-existing thrust pair continues to slip after the development of the second

pair and consequently, the addition of the new fault pair has less impact on the overall fault network. The persistent slip along the pre-existing forethrust, in particular, causes the associated region of high strain energy density to remain relatively similar after the new pair develops (supp. Fig. 2.3). The incremental shear strain field of the physical accretion experiment confirms that after the new thrust pair develops, slip persists along the near surface, up-dip portions of the pre-existing forethrust (Fig. 2.1,). This observation, as well as the greater slip observed on forethrusts relative to backthrusts in both numerical and physical wedges in both stages of faulting (Fig. 2.1), suggest that the slip distribution along the physical thrusts is well-captured by the numerical thrusts. This validation suggests that the evolution of W_{ext}, W_{int}, W_{fric}, and W_{grav} tracked within the numerical systems may closely represent that evolution in the stages of the physical experiment simulated here.

2.6.2. Sensitivity of efficiency to forethrust position

For the first and second stages of forethrust-backthrust pair development, the highly efficient geometries that produce >80% of the maximum $\Delta W_{ext}/\Delta A$ almost completely overlap the regions of high shear strain in the physical experiment that highlight the forethrusts (Fig. 2.4). In the second stage of faulting, the range of forethrust positions that produce >80% of the maximum forethrust $\Delta W_{ext}/\Delta A$ (30 mm) is wider than that range in the first stage of faulting (20 mm). This observation suggests that $\Delta W_{ext}/\Delta A$ is more sensitive to position in the first stage of fault development than the second stage.

The varying sensitivity of efficiency to forethrust position arises from differences in the gradient of the basal displacements at the first and second stages of thrust faulting.

High gradients in the basal displacement produce local regions of high strain energy density (SED) within the wedge (Fig. 2.11). SED is the product of stress and strain [e.g., *Jaeger et al*., 2007], and measures the internal mechanical work stored in the host rock. Fault tips and other irregularities typically produce regions of high SED, and numerical analyses indicate that fractures tend to propagate into regions of high SED [e.g., *Du and Aydin*, 1993, 1996; *Olson and Cooke*, 2005; *Okubo and Schultz,* 2005]. In the first stage of thrust faulting, the applied basal displacements produce a localized region of high SED from ~70-90 mm from the backwall, whereas in the second stage, the applied displacements produce a wider region of high SED from ~90-130 mm from the backwall. The smaller region of high SED in the first stage results from the sharper gradient in the applied horizontal displacements, compare to the second stage of faulting (Fig. 2.11C). In the first stage of faulting, the sharp displacement gradient and associated high SED region occur in the region where the most efficient forethrusts form, suggesting that this localization of internal strain controls the predicted position of the thrusts. In contrast, in the second stage of faulting, the gentler displacement gradient results in a wider region of high SED, and a corresponding reduced sensitivity of $\Delta W_{ext}/\Delta A$ to horizontal position.

These gradients in the applied displacements arise from slip gradients along the basal detachment fault within the physical experiment. In the first stage of faulting, the distribution of slip along the physical wedge base produced by the detachment fault has a sharp decrease in slip near the location of incipient faulting. Applying the effects of this slip gradient to the base of our models provides a method of incorporating the local concentration of SED arising from the slip gradient along the detachment. In contrast, during the second stage of faulting the detachment produces a more gradual slip gradient

so that the position of thrust faulting is not as strongly controlled by the slip gradient as it is for the first stage of faulting.

2.6.3. Comparison of numerical and physical estimates for W_{prop}

The increase of W_{ext} between episodes of new fault development reveals that energy must accumulate within the fault system before it reaches the value required for the creation of new fault surfaces [*Del Castello and Cooke*, 2007]. Consequently, the energy required to create new fault surfaces, $W_{prop,}$ can be determined from the change in W_{ext} and forces on the system preceding and following fault development [*Herbert et al.*, 2015]. *Herbert et al.* [2015] calculate W_{prop} for the same physical accretion experiment simulated here (E240) from the change in force measured on the backwall and the distance over which the force drop occurs; in a sandpack of 16 mm thickness, W_{prop} is 104±60 mJ/m^2 [*Herbert et al*., 2015]. To compare our numerical calculations of W_{ext} to the physical estimates of W_{prop}, we scale our model displacement (0.5 mm) to the total displacement over which the faults develop (2 mm), and assume that W_{ext} scales linearly for the development of the first forethrust-backthrust pair. Incremental loading of the numerical wedge that contains the observed geometry of the backthrust and forethrust in the first stage of faulting (Fig. 2.9, system 3) reveals that W_{ext} increases approximately linearly after the loading increment in which slip occurs along the complete length of both faults (R^2=0.989, supp. Fig. 2.4). Although frictional slip is inelastic and may account for the deviance from purely linear, its small influence in these models suggests that W_{ext} may be linearly approximated.

In the numerical simulations of this experiment, the $\Delta W_{ext}/\Delta A$ due to the development of the first forethrust-backthrust pair is approximately 20 mJ/m^2 for 0.5 mm of moving

wall displacement. For the minimum and maximum of the observed displacement range (1.903 mm, 2.409 mm), the derived values of $\Delta W_{ext}/\Delta A$ scale to 76.12 mJ/m^2 and 96.36 mJ/m^2, respectively, for experiment E240. These scaled estimates yield similar magnitudes to the $W_{prop}/\Delta A$ estimated from external force for this experiment (104±60 mJ/m^2) [*Herbert et al.*, 2015]. As expected, these values for fault growth in dry sand are orders of magnitude lower than W_{prop} estimates for crustal faults [e.g., *Chester et al.*, 2005; *Wilson et al.*, 2005; *Pittarello et al.*, 2008]. The consistency of these results, as well as the agreement between the predicted and observed thrust geometry, and the numerical and physical fault slip distribution, indicates that these numerical accretion simulations closely represent deformation of the physical wedge, which facilitate the calculation of work done within the system and so provides insight into the processes that control fault evolution.

2.7. Conclusions

The planar through-going fault configurations that produce the largest changes in external work per new fault area, $\Delta W_{ext}/\Delta A$, within simulations of two stages of a physical sandbox accretion experiment closely match the observed geometries of new forethrust-backthrust pairs in the two simulated stages. At the position of the observed thrusts, the dips of the most efficient backthrust and forethrust match within 4º of the observed dips, and consistently more closely match the observed orientation than the planes with maximum Coulomb stress. Fault planes that maximize the average Coulomb stress along the faults at the position of the observed thrusts more closely match the dip of the most efficient thrusts and the observed thrusts. For both stages of faulting, the

ranges of highly efficient forethrusts overlap the region of high shear strain along the observed forethrusts. In the first stage of faulting, the geometry of the highly efficient backthrust overlaps the observed thrust when the numerical wedge contains a pre-existing forethrust. The match of the backthrust prediction in simulations that include a pre-existing forethrust, and the strain evolution of the physical experiment, revealed with digital image correlation (Fig. 2.1), suggest that forethrust development precedes backthrust growth in the first stage of faulting. Using work optimization to assess the order of thrust development may provide additional insight into the mechanics of frontal accretion thrust vergence, which could indicate the likelihood of shallow megathrust rupture [*Cubas et al.*, 2016]. The elevated $\Delta W_{ext}/\Delta A$ due to the propagation of the first backthrust-forethrust pair, as compared to the second pair, indicates that if pre-existing thrusts continue to slip, the propagation of new thrusts may lead to increasingly smaller gains in efficiency relative to new fault area as the accretionary wedge evolves. The similar estimates of experimental $W_{prop}/\Delta A$ and numerical $\Delta W_{ext}/\Delta A$, and similar evolution of experimental force drops and numerical ΔW_{ext} due to fault development suggest that analysis of evolving work budget components may be exacted with confidence in both numerical and physical experiments. In this contribution, integrating these methodologies enabled the comparison of predictions of work minimization and Coulomb stress with the observed, physical faults. These comparisons provide additional support to the concept that tectonic systems evolve in order to minimize the total work of the system. Furthermore, tracking the individual and evolving components of the total system work budget lends detailed insight into the primary deformation mechanisms controlling system efficiency. In these simulations, the energy expended in frictional slip

and off-fault deformation controls the efficiency of the system. This analysis suggests that field observations of the distribution and magnitude of energy expended in frictional slip (i.e., pseudotachylite, silica gel) or internal host rock deformation (i.e., calcite twinning, grain boundary migration) could be used to quantify the efficiency of a tectonic environment, and perhaps to predict the growth and interaction of faults within crustal systems.

Acknowledgements

This work was supported in part by two Geological Society of America student research grants, an International Association of Mathematical Geologists Computers & Geosciences student research grant to JM, as well as a National Science Foundation grant EAR-1019747 to MC. All data used are listed in the references, tables and supplements.

2.8. Figures

Figure 2.1

Strain localization revealed by DIC analysis of physical experiment. Horizontal incremental displacement field (mm) calculated from DIC increments immediately before (A), immediately after (B), and shortly after (C) first backthrust-forethrust pair is observed. Horizontal incremental displacement field calculated in DIC increments immediately before (D), immediately after (E), and shortly after (F) second backthrust-forethrust pair is observed. Curl (rad/5s) field (G-L) derived from incremental displacement fields. Black lines show numerical model boundaries. After both stages of new thrust pair development, the forethrust has more localized strain than the backthrust, which is shown by elevated curl.

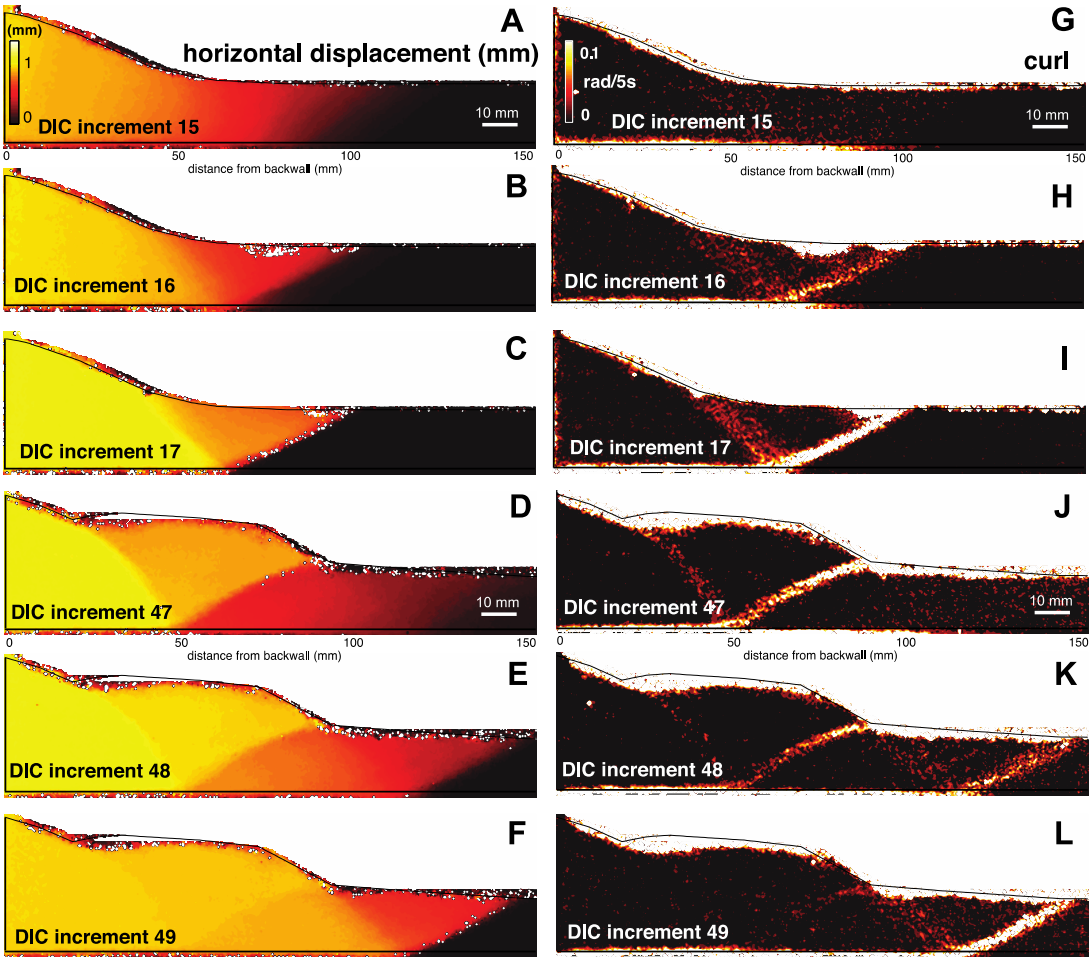

Figure 2.2

Boundary conditions of models determined from DIC of physical experiment. Horizontal incremental displacement field immediately preceding development of first (A) and second (B) backthrust-forethrust pair. Horizontal black line shows location of transect that samples displacement field near physical detachment. Vertical incremental displacement field immediately preceding development of first (C) and second (D) backthrust-forethrust pair. Horizontal and vertical incremental displacements along transect near base of physical experiment for first (E) and second (F) stages of faulting. Blue dots show raw displacements calculated with DIC analysis. Red dots show displacements after median filter performed. Dark blue lines show smoothed displacements. Light blue lines show filtered, smoothed, scaled displacements, in which the maximum horizontal displacement is 0.5 mm. Numerical model boundaries and loading conditions for first (G) and second (H) stages of faulting. Coordinate system of loading conditions is relative to boundary elements, and shown with gray arrows (G). Horizontal displacement field within numerical simulations of first (I) and second (J) stages of faulting. Rightward displacements are positive. Vertical displacement field within numerical simulations of first (K) and second (L) stages of faulting. Upward displacements are positive.

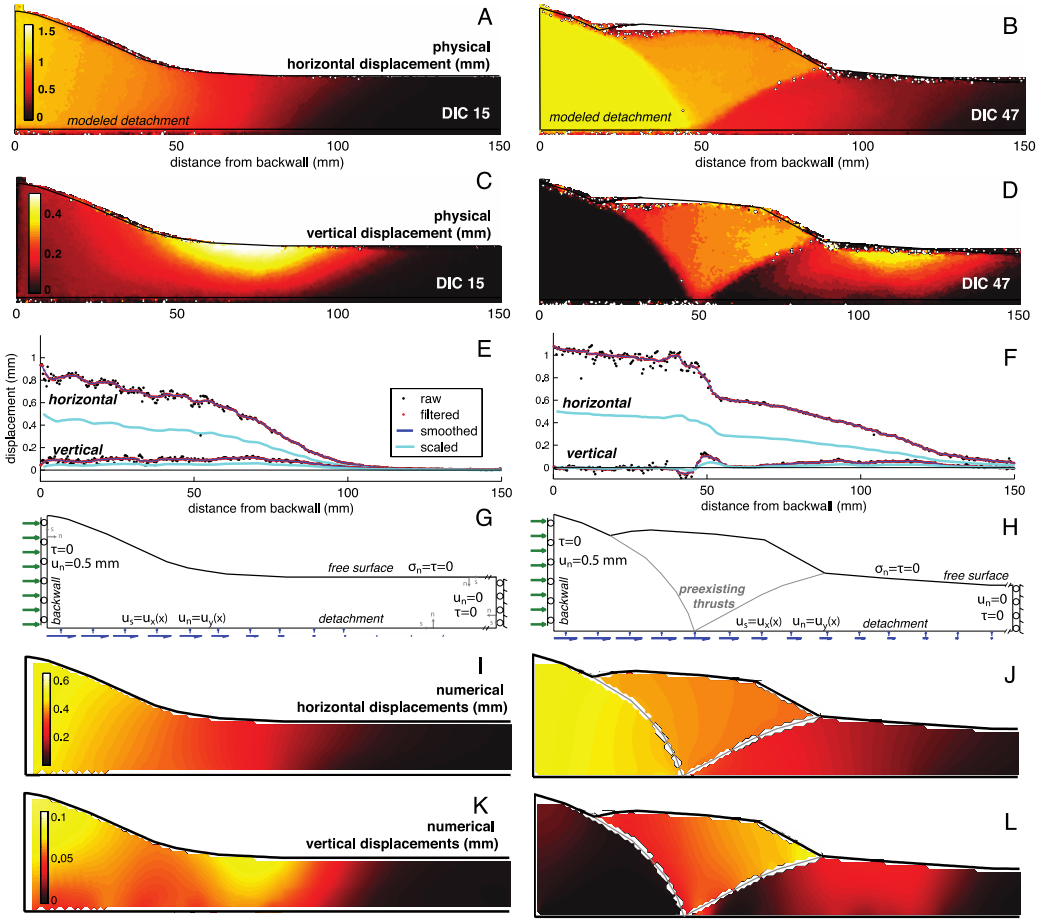

Figure 2.3

Results of work optimization search for geometry of pair. A) First and B) second forethrust-backthrust pair to develop in wedge. A-B) Change in external work divided by new fault area, ΔW_{ext} /ΔA, for all geometries. Large ΔW_{ext} /ΔA indicates that added faults increase the efficiency of the system. Black circles indicate most efficient backthrust and forethrust geometries. Black contour lines show 10% increments of $\Delta W_{ext}/\Delta A$ relative to $\Delta W_{ext}/\Delta A$ of the most efficient backthrust or forethrust. $\Delta W_{ext}/\Delta A$ of optimal backthrust and forethrust in second stage are lower than $\Delta W_{ext}/\Delta A$ of optimal thrusts in first stage. The larger range of positions that produces >90% $\Delta W_{ext}/\Delta A$ of the optimal forethrust in second stage compared to the first stage suggests a reduced sensitivity of $\Delta W_{ext}/\Delta A$ to position in the second stage

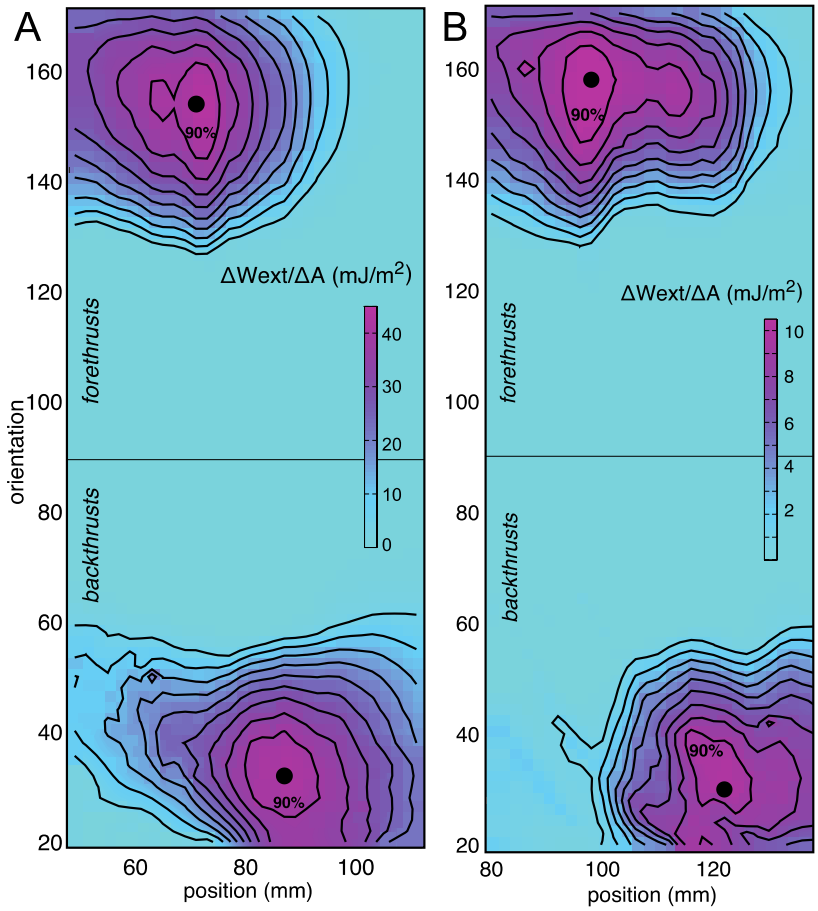

Figure 2.4

Comparison of observed thrusts to efficient thrusts. A-B) First and (C-D) second stages of faulting. Regions of high curl indicate enhanced rotation of sand grains, and localization of shear strain along faults. A, C) Location of most efficient backthrust (thickest line), extent of backthrusts that produce >90% of the maximum $\Delta W_{ext}/\Delta A$ (thinner lines), and extent of backthrusts that produce >80% of the maximum $\Delta W_{ext}/\Delta A$ (thinnest lines). B, D) Locations of efficient forethrusts. The backthrust geometries that produce >80% of the maximum $\Delta W_{ext}/\Delta A$ overlap regions of high curl along the observed backthrust in the first and second stages of faulting (B,D). The forethrust geometries that produce >90% of the maximum $\Delta W_{ext}/\Delta A$ overlap regions of high curl along the observed forethrust in the first and second stages of faulting (B,D).

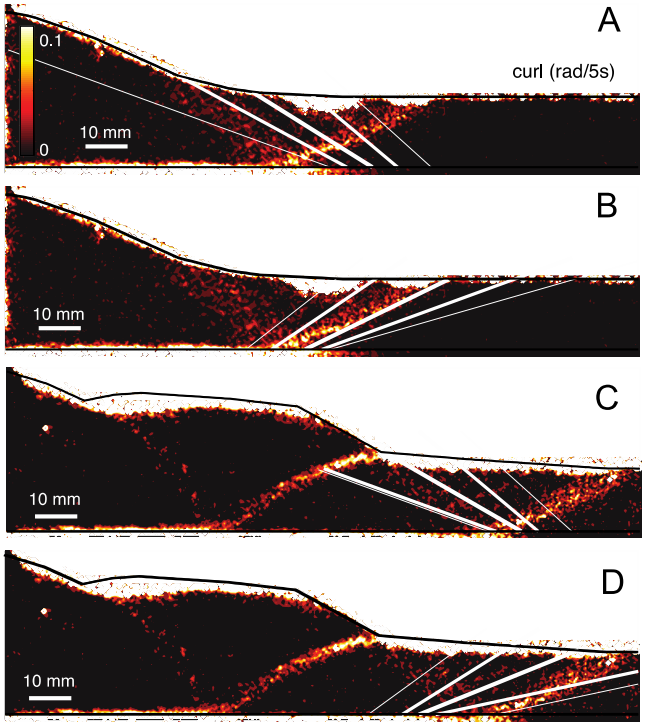

Figure 2.5

Comparison of work optimization and Coulomb predictions. A-D) First and (E-F) second stages of faulting. A, E) Coulomb stress along planar faults at the observed location. B, F) Orientation of planar faults vs. maximum and average Coulomb stress along faults. Black vertical lines indicate observed orientations of backthrust and forethrust. Gray rectangles indicate extent of relatively high curl surrounding observed thrusts. Circles show maximum Coulomb stress of elements of planar fault at each orientation. Squares show average Coulomb stress of elements of planar fault at each orientation. Black circle and square indicates maximum of the maximum Coulomb stress and of the average Coulomb stress, respectively. C) Gain in efficiency, $\Delta W_{ext}/\Delta A$, produced by faults with various orientations at the position of the first observed backthrust-forethrust pair (65 mm). Black triangles indicate ends of optimal thrusts. Dashed lines show approximate geometry of observed thrusts. D) Orientation of faults at 65 mm from backwall vs. $\Delta W_{ext}/\Delta A$. G) Gain in efficiency, $\Delta W_{ext}/\Delta A$, produced by faults with various orientations at the observed position of the second backthrust-forethrust pair (114 mm). H) Orientation of faults at 114 mm from backwall vs. $\Delta W_{ext}/\Delta A$.

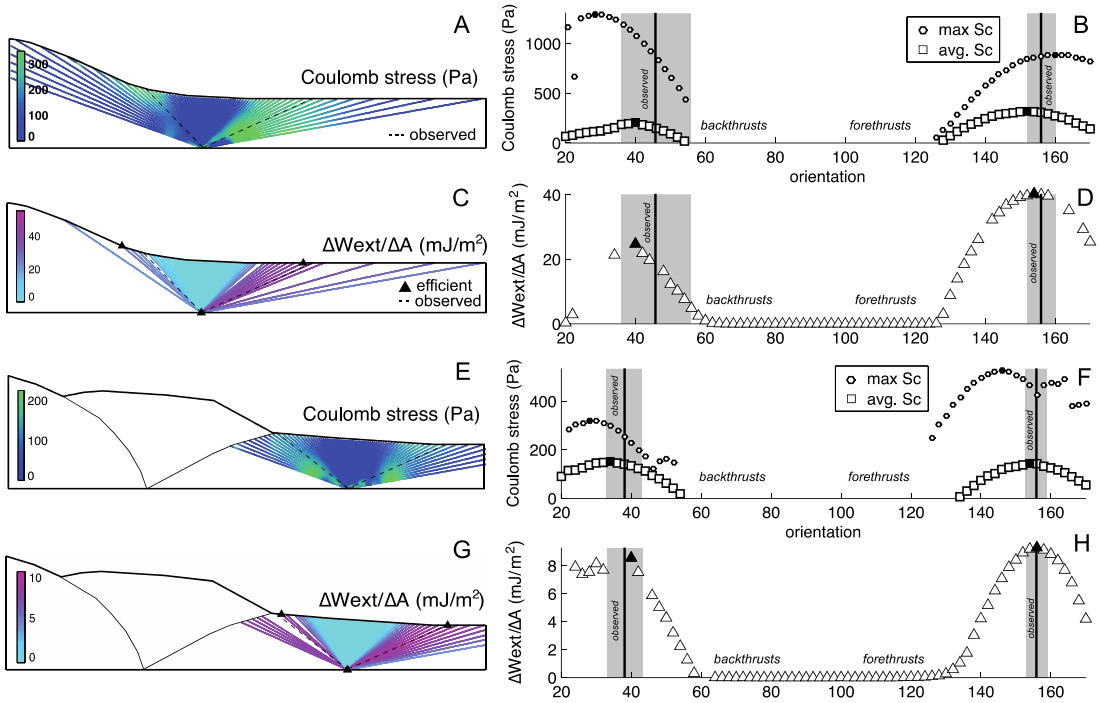

Figure 2.6

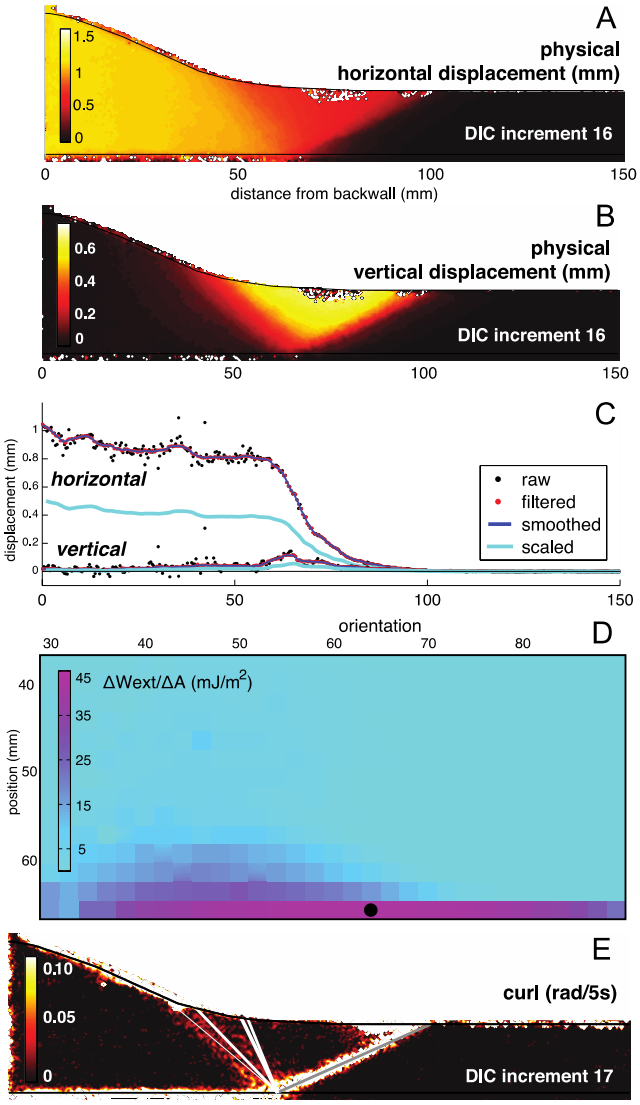

Work optimization search after first forethrust develops. A-C) Development of loading conditions for numerical wedges that represent immediately after the first forethrust develops. Format and notation identical to Fig. 2.2. D) Results of work optimization search for geometry of first backthrust, after first forethrust forms. Format and notation identical to Fig. 2.3. Contour intervals of $\Delta W_{ext}/\Delta A$ are not shown here for the sake of clarity. The 90% and 80% contour intervals only include fault geometries at 65 mm. E) Comparison of predicted and observed geometries of backthrust. Gray line shows pre-existing forethrust included in the model, otherwise the format is identical to Fig. 2.4. Fault geometries that produce >90% $\Delta W_{ext}/\Delta A$ of optimal backthrust completely overlap observed backthrust. These backthrusts share a common root with the pre-existing forethrust in the model.

Figure 2.7

Coulomb predictions after first forethrust develops. Comparison of predictions of work optimization and Coulomb failure planes for first stage of faulting that includes the new forethrust. Format and notation is identical to Fig. 2.4. D) Backthrust orientations that produce >90% $\Delta W_{ext}/\Delta A$ of the maximum are shown with gray triangles, and include the observed orientation of 45°.

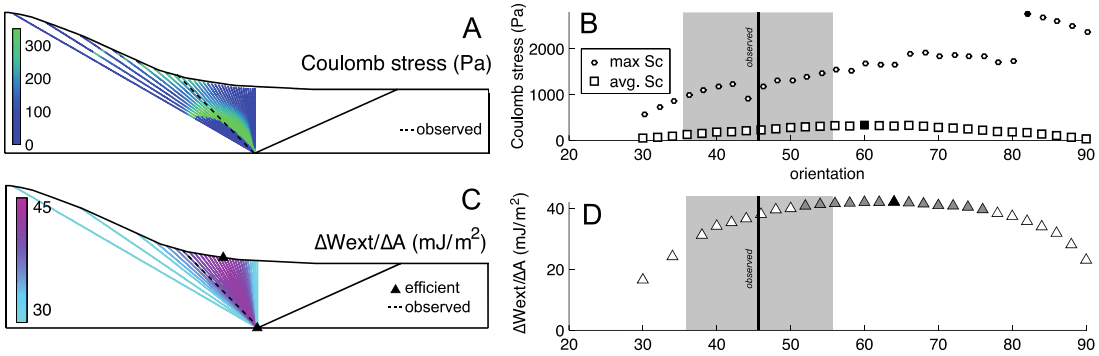

Figure 2.8

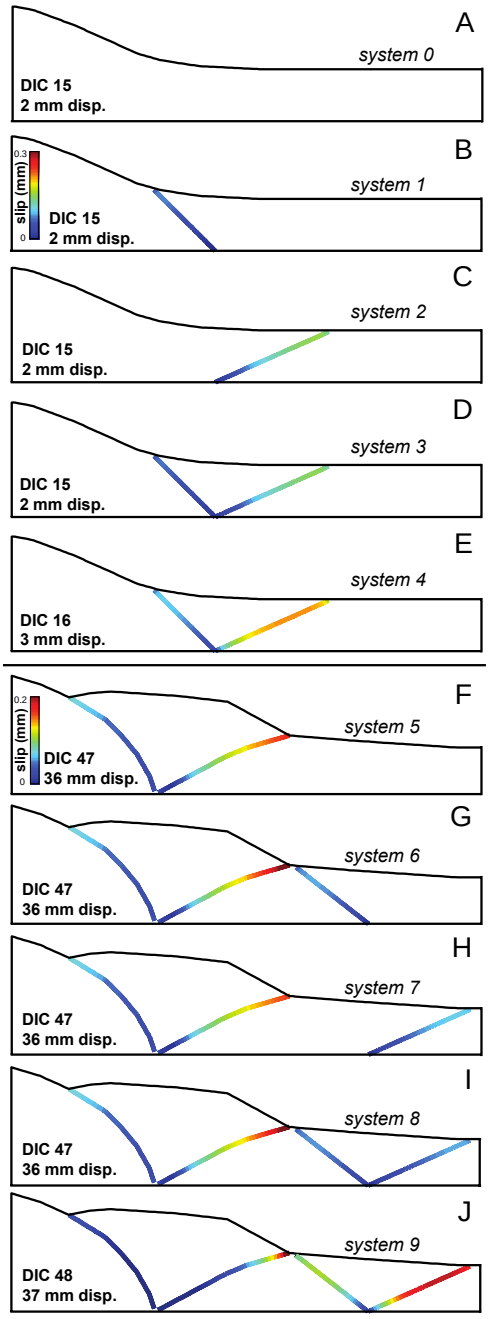

Stages of wedge development with fault slip in numerical wedges. Stages of wedge development include backthrust and forethrust geometries that represent the observed thrust geometries. A-E) Systems 0-3 represent the first stage of faulting, and use the displacements observed immediately before the first thrusts develop (DIC increment 15, ~10 mm cumulative backwall displacement), and immediately after the first thrusts develop (system 4, DIC increment 16, ~11 mm cumulative backwall displacement). F-J) Systems 5-9 represent the second stage of faulting, immediately before thrusts in the second new pair develop (5-8, DIC increment 47, ~45 mm cumulative backwall displacement), and immediately after the thrusts develop (9, DIC increment 48, ~46 mm cumulative backwall displacement).

Figure 2.9

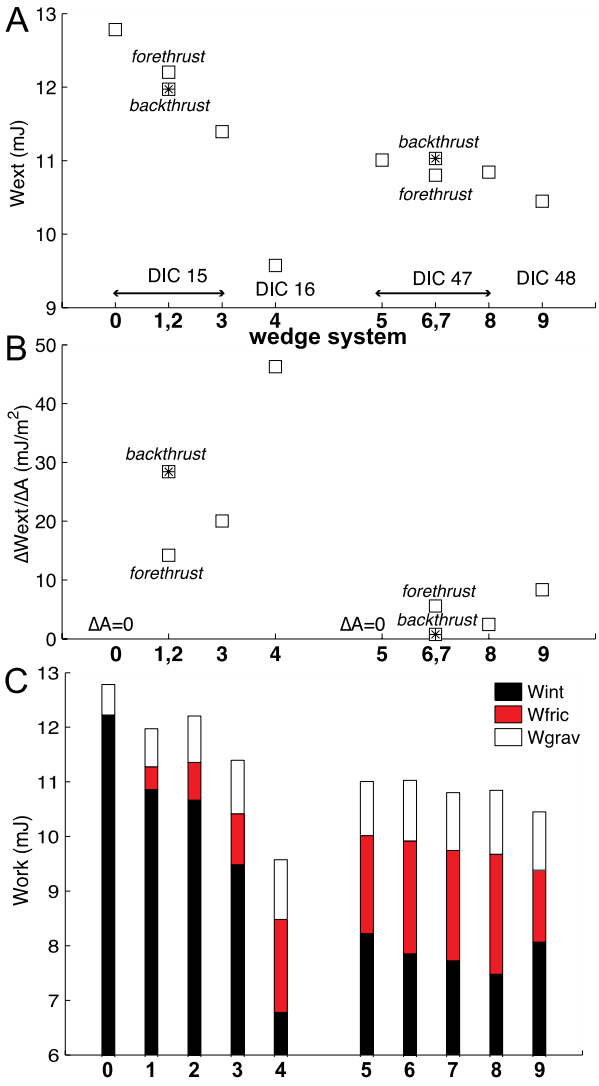

Evolution of efficiency. W_{ext} (A), gain in efficiency relative to newly propagated fault, $\Delta W_{ext}/\Delta A$ (B), and evolution of internal work (W_{int}), frictional work (W_{fric}) and gravitational work (W_{grav}) (C) for various stages of wedge development shown in systems in Fig. 2.8.

Figure 2.10

Evolution of work budget and backwall force, Evolution of internal work (W_{int}), frictional work (W_{fric}) and gravitational work (W_{grav}) for stages of wedge development with force curve measured throughout physical accretion experiment E240. Consistent with the larger ΔW_{ext} produced by the development of the first pair relative to the second pair, the drop in force associated with the development of the first pair is larger than the drop associated with the second pair. Consistent with the increase in W_{ext} from system 4 to system 5, the force gradually rises following the development of the first pair to the second pair.

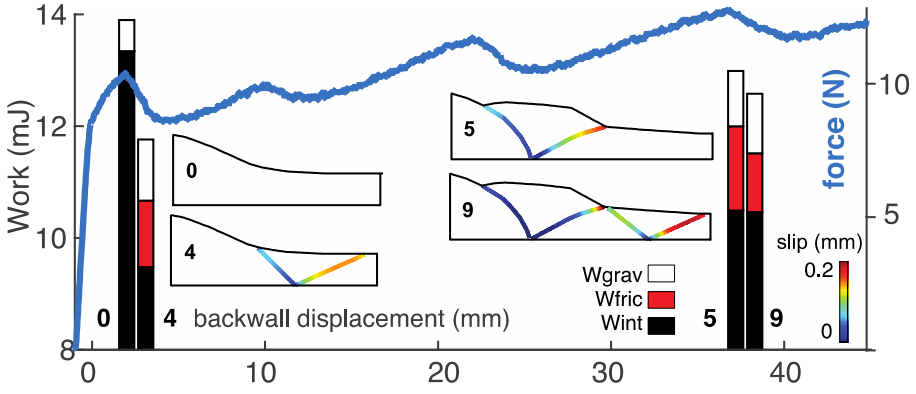

Figure 2.11

Strain energy density (SED) in numerical wedges**.** SED produced in numerical wedges representing first (A) and second (B) stage of faulting. White lines indicate geometries of most efficient forethrust (thickest line), forethrusts that produce >90% of maximum forethrust $\Delta W_{ext}/\Delta A$ (thinner lines), and forethrusts that produce >80% of maximum forethrust $\Delta W_{ext}/\Delta A$. C) Horizontal and vertical displacements applied to base of numerical wedges. Region of high SED is more localized in first stage than region in second stage. Range of predicted positions of efficient forethrust geometries is smaller in first stage. Gradient in applied horizontal displacements is larger in first stage than in second stage near the position where the observed thrusts develop.

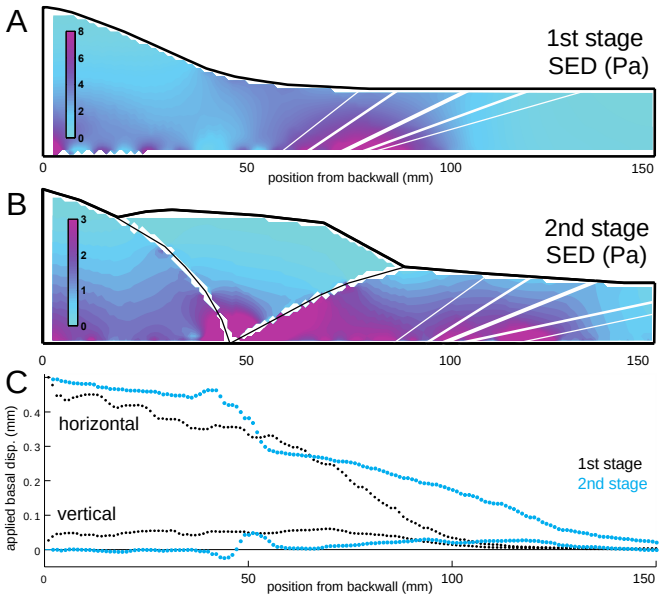

2.9. Table

Table 2.1

Property	Value
Poisson's ratio	0.2
Young's modulus	0.25 MPa
Mode-I fracture toughness	2.5 MPa*$m^{1/2}$
Density	1700 kg/m^3
Cohesion	0 MPa
Static friction coefficient	0.65
Dynamic friction coefficient	0.17
Slip-weakening distance	0.25 mm

Intact and fault properties used in numerical models. Intact properties are representative of CV32 sand used at UCP [*Herbert et al*., 2015; *Maillot,* 2013]. Poisson's ratio value is typical for dry sand [e.g., *Lambe and Whitman*, 1969]. Sandpacks constructed with UCP sedimentation device produce uniform sandpacks with density of 1700 kg/m^3 [*Cubas et al*., 2010; *Maillot*, 2013]. Young's modulus is calculated from force measurements on backwall of experimental device [*Herbert*, 2014]. Casagrande shear box tests determine an intact coefficient of friction of 0.96 and dynamic friction of 0.72 [*Maillot*, 2013]. Friction coefficients slightly below these values are used in order to represent failure along more evolved failure surfaces that include sand grains that are more favorably aligned for slip. The chosen slip-weakening distance matches the median diameter of the CV32 sand grains.

2.10. Supplemental information

Supplemental Figure S.2.1

Observed planar thrust geometries. Planar geometries used to compare physical and numerical results derived from incremental curl field of experiment in the first (A-B) and second (C-D) stages of faulting. Median reported position and dip of observed thrusts shown in solid white lines. Thrust geometries produced by range of observed dips (A, C) and positions (B, D) shown in dashed white lines. Range of observed dips derived from maintaining the median position and increasing or decreasing the dip. Range of observed positions derived from maintaining the median dip and increasing or decreasing the position. Range of observed geometries is reported, rather than one position and dip for each thrust, because regions of high curl (shear strain) in the experiment are not perfectly planar, nor sufficiently localized, so that regions of high curl persist in regions surrounding the thrusts.

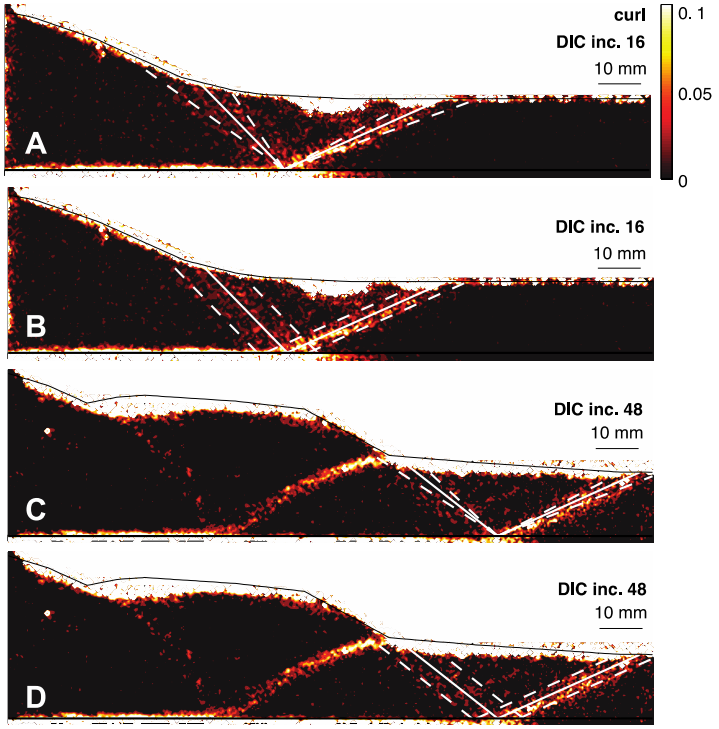

Supplemental Figure S.2.2

Condition numbers of models. Condition numbers for models analyzed in search for optimal geometry in the first stage of faulting (A), second stage of faulting (E), and first stage of faulting after forethrust develops (I). Low condition numbers indicate robust, reliable numerical results. White circles indicate the most efficient systems. Models with backthrusts often have high condition numbers because the intersection of the upper tip of the backthrust with the wedge topography produces irregular element sizes and/or closely spaced element nodes. Histogram of condition numbers for models in first stage of faulting (B), second stage of faulting (F) and first stage of faulting after forethrust develops (J). Models with anomalously high condition numbers that exceed 125% of the condition number mode are removed from the search for the most efficient thrust geometry. Un-interpolated results of work optimization search for geometry of first (C) and second (G) forethrust-backthrust pair to develop in wedge, and geometry of first backthrust to develop after forethrust forms (K). White squares reveal models with relatively high condition numbers. D, H, L) Results with interpolated values of $\Delta W_{ext}/\Delta A$. The most efficient thrust geometries are identified from the un-interpolated data.

Small differences between models, including the irregular spacing of element nodes at the intersection of faults to the model boundaries, influence the robustness of the solution found when Fric2D inverts the influence coefficient matrix, which relates the displacements and tractions of each element on every other element in the model [*Cooke and Pollard*, 1997]. To assess the reliability of the model inversion, we compare the condition number, which is the product of the norm of the influence coefficient matrix and the norm of its inverse for the numerical wedges assessed in the analysis of each stage of faulting. Condition numbers reveal the sensitivity of a solution to perturbations in the system. When the condition number of a model is 125% higher than the mode of the condition numbers for that stage of faulting, we do not report the results and instead interpolate values of $\Delta W_{ext}/\Delta A$ from similar geometries to approximate the efficiency of this system following the interpolation methodology of *Errico* [2008].

Supplemental Figure S.2.2

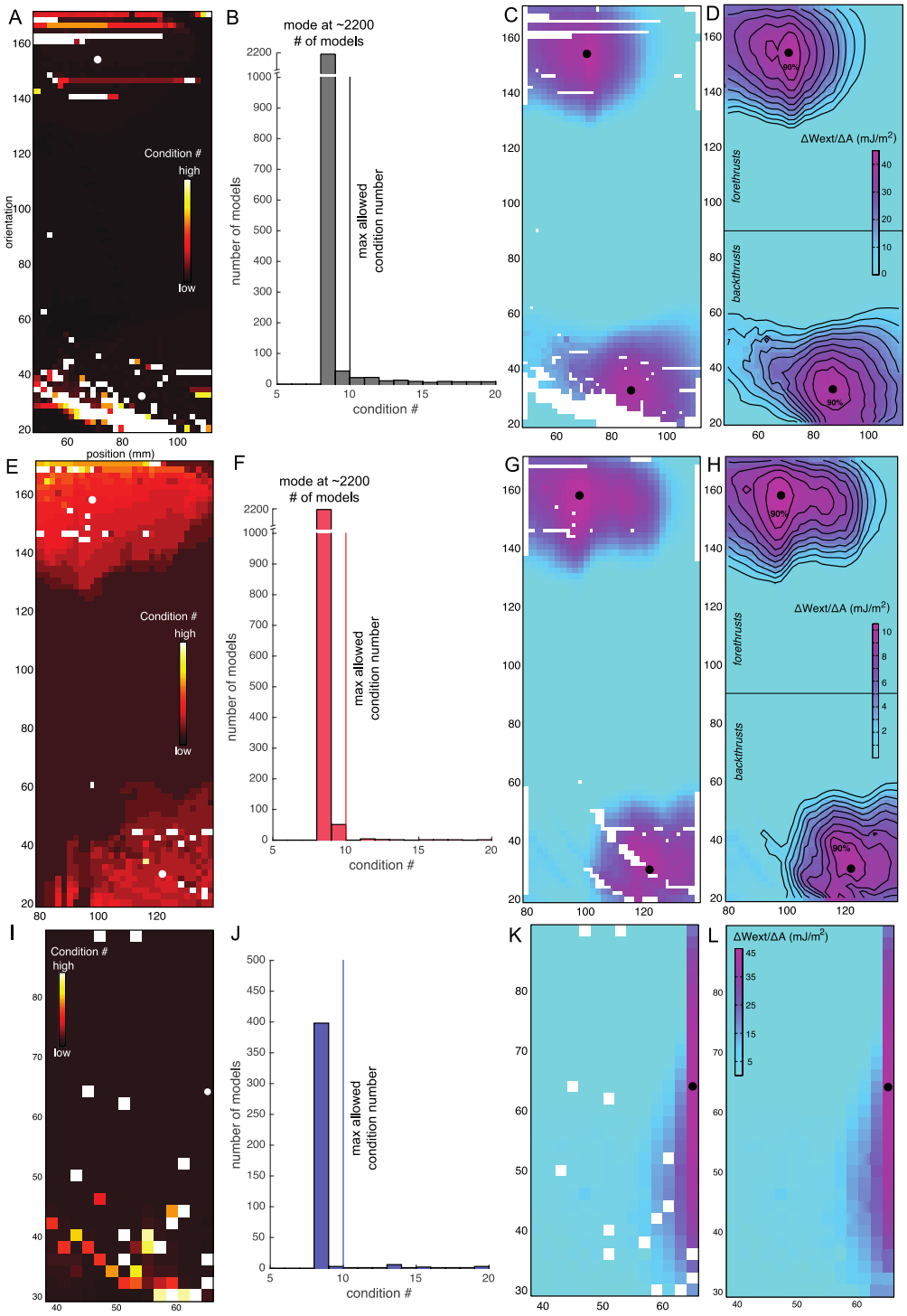

Supplemental Figure S.2.3

Properties dominating work budget components. A) Frictional work calculated from slip along faults. B) Internal work may be calculated from strain energy density (SED) field. C) Gravitational work calculated with uplift. Slip along thrusts in system 1 and 2 appear similar to slip along thrusts in system 3, indicating that the presence of one thrust does not strongly control slip along the other thrust when the applied displacements simulate immediately before the first pair forms (DIC 15). When the applied displacements simulate the wedge immediately after the pair forms (system 4, DIC 16), slip increases on both thrusts. This pattern of slip distribution along the new thrusts occurs in the second stage of faulting as well: the slip distribution along the backthrust and forethrust are relatively similar with (system 8) or without (system 6 and 7) the other thrust, when the displacements represent the wedge before the new pair forms, and slip is promoted on the new thrust pair when the displacements represent the wedge after the new pair has formed. The SED field produced by the addition of the first forethrust (system 2) is very similar to the SED field of the wedge with both thrusts (system 3 and system 4), whereas the SED field of the wedge with only the backthrust (system 1) looks more similar to the pre-faulted wedge (system 0). These changes in the SED field are captured in the evolution of internal work, which decreases by a greater degree due to forethrust development than backthrust development (Fig. 8). When the applied displacements simulate DIC 16 (system 4), the region of high SED near the base of the forethrust present in system 3 shrinks. This reduction in internal strain is mirrored in the larger reduction of internal work in system 4 than system 3 (Fig. 8). In contrast to the relatively weak influence of the other thrust on fault slip, in the second stage of faulting, the thrust pair (system 8 and 9) shrinks the regions of high SED present without the new thrusts (system 5) to a greater extent than the addition of either the backthrust or forethrust. This shrinkage in high SED is revealed in the work budget as the greater decrease in internal work due to the addition of the pair compared to the reduced decrease in internal work due to backthrust or forethrust propagation. In the first stage of faulting, an increasing amount of uplift is accommodated by the addition of each thrust, thrust pair, and updating of the applied displacements. The progressive increase in gravitational work captures this evolving uplift field. In this stage, backthrust propagation produces a more pronounced change in the uplift than in the SED field. In particular, the SED field of system 1 appears relatively similar to system 0, whereas the uplift field of system 1 shows distinct changes in magnitude and distribution from system 0. Although the change in uplift due to backthrust propagation is more pronounced than the change in SED within this representation, the signal of the change in uplift within the work budget (i.e., the change in gravitation work) is smaller than the signal of the change in SED (i.e., the change in internal work). For the second stage, similar to the relatively small changes in slip produced by the addition of the other thrust in the pair (systems 6-8), the changes in the uplift field following the addition of both thrusts appear relatively similar to the uplift field following the addition of a single pair. After updating the applied displacements, uplift is reduced in the triangle zone between the first pair, and increased in the zone between the second pair. This shift in the uplift nucleus reduces the total gravitational work, increasing the mechanical efficiency of the system.

Supplemental Figure S.2.3

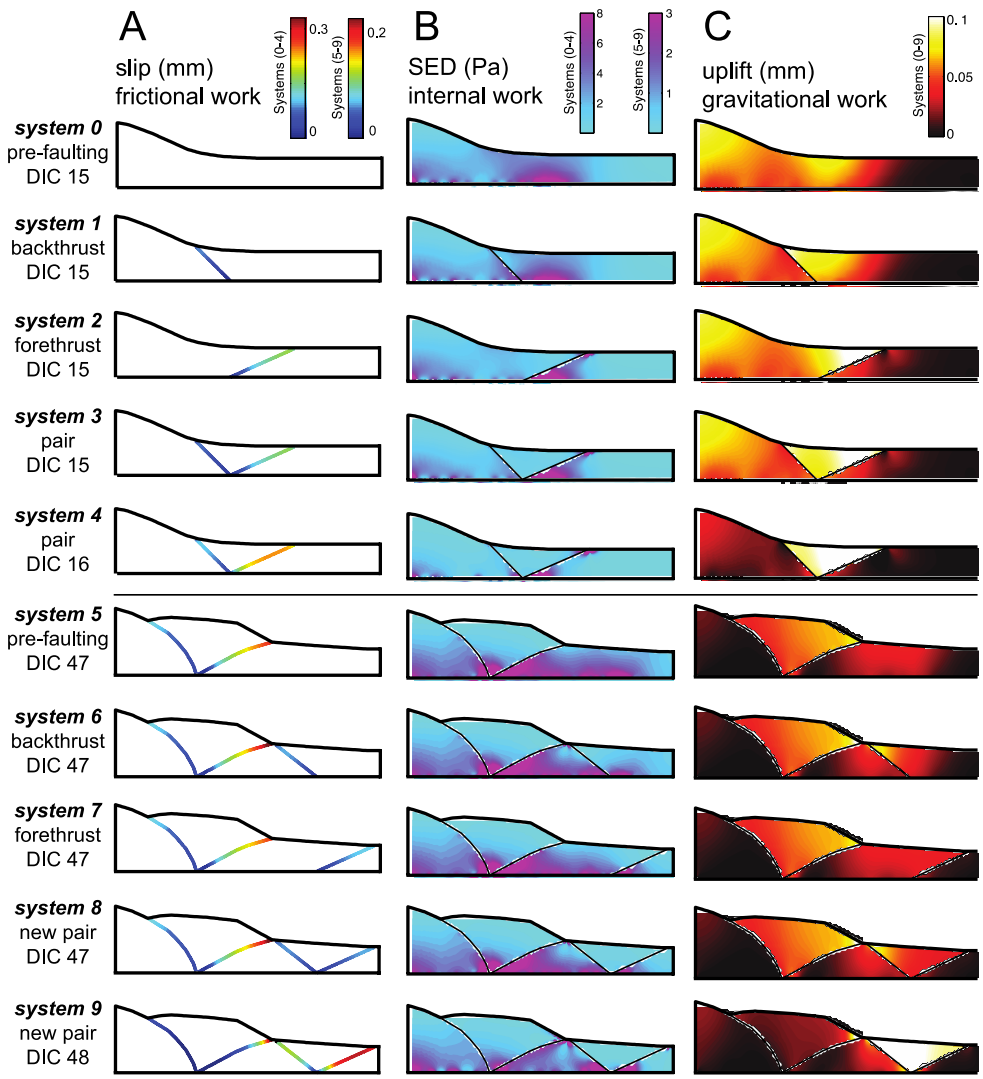

Supplemental Figure S.2.4

External work with multiple loading steps. A) External work at each stage of loading of the numerical wedge with the observed geometry of the backthrust-forethrust pair in the first stage of faulting (Fig. 9, system 3). W_{ext} increases approximately linearly throughout the loading steps when slip occurs along the entire length of both faults (steps 5-10), with a linear line of best fit where R^2=0.9988. B) Slip along faults for each loading step. Steps 5-10 are the loading increments in which significant slip occurs along the full length of both faults. In steps 1-4, slip does not occur on some portions of the faults.

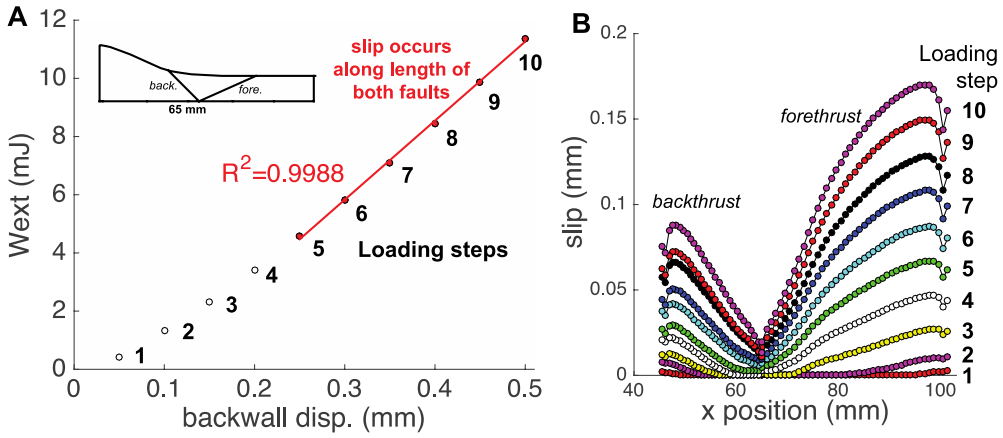

CHAPTER 3

SYNTHESIZING NUMERICAL AND PHYSICAL EXPERIMENTS TO CONSTRAIN THE EVOLVING DEFORMATIONAL ENERGY BUDGET OF ACCRETIONARY FAULTING

3.1. Abstract

Tracking the evolution of deformational energy partitioning within accretionary systems provides insight into the driving mechanisms that control fault development. To quantify the impact of these mechanisms on fault development, we constrain energy budget components with the development of the first thrust fault pair in physical dry sand accretion experiments, and in numerical simulations of snapshots of the physical experiments. To assess the impact of detachment strength on fault development and the energy budget, we track energy budget components in experiments that include and exclude a basal layer of glass beads. To correct for the influence of sidewall friction drag on the calculated energy budget components, we synthesize observations from experiments with opposing apparatus configurations. To identify the effective elastic moduli and friction coefficients of both the detachment and thrust faults that enable the numerical simulations to reproduce the deformation observed in the physical experiments, we perform a misfit analysis that minimizes the difference between both the force exerted on the backwall, and the extent of the slipping portion of the detachment fault in the numerical and physical experiments. The evolving energy budgets of the numerical wedges indicate that fault development increases the total system efficiency by reducing the energy expended in pervasive off-fault deformation. Although fault development increases the work done against frictional slip and the work expended in

uplift against gravity, the reduction in the energy consumed in internal deformation is greater than the increase in frictional work and gravitational work. Similar to the numerical simulations, in the physical experiments, thrust faulting increases the gravitational and frictional work while reducing the external work. Following the conservation of energy, these trends indicate that internal work should decrease due to thrust fault development. In contrast, the estimates of incremental internal work in the physical experiments suggest that internal work increases consistently throughout each experiment. Spurious noise in the displacement fields calculated from DIC likely contributes to this unexpected result. The rate of increase in physical internal work decreases following thrust fault development. The agreement of the work budget components in the physical experiments and numerical wedges suggests that the numerical models closely capture the uplift, fault slip and distributed off-fault deformation produced in the physical experiments. Low slip on the backthrust in the physical experiments including the glass bead layer suppresses the decrease in external work and increase in frictional work due to fault development compared to the experiments excluding the glass bead layer. Comparison of the work budget of numerical simulations representing the sides of the physical experiments to the simulations representing the center of the experiments suggests that physical work components calculated from the incremental displacement fields of the sides of the sandpack, including the frictional, gravitational, and internal work, may underestimate the work done within the center of the wedge. The shallower thrust dips on the sides of the apparatus may produce lower estimates of frictional and gravitational work than the work done within the center of the wedge, where the thrust dips are steeper.

3.2. Introduction

In accretionary prisms, margin-perpendicular convergence produces diffuse compaction until strain localizes into discrete frontal thrust faults. Following thrust development, convergence promotes slip on preexisting faults and triggers new fault propagation. Constraining the factors that control the transition from diffuse compaction to discrete slip, and from preexisting slip to fault propagation is critical to understanding fault development and interaction in accretionary systems.

The relatively inaccessible tectonic setting of crustal accretionary wedges enhances the need of scaled, quantitatively monitored physical experiments, and carefully calibrated numerical simulations in understanding the evolution of faulting in accretionary systems. Similarity in accretion deformation inferred or observed with these different approaches lends confidence to the corresponding predictions [e.g., *Buiter et al*., 2016].

Previous studies suggest that understanding the energetic tradeoffs between fault development and other deformation mechanisms, such as pervasive internal strain, can help predict the timing and geometry of new frontal accretion thrust faults [e.g., *Del Castello and Cooke,* 2007; *McBeck et al*., in rev.]. Constraining the energy available for creating new fault surfaces suggests that new frontal accretion faults may only develop when the system has stored sufficient energy available for fault growth [*Del Castello and Cooke,* 2007]. Estimating the work consumed in fault propagation in physical accretion experiments indicates that this component of the work budget depends on material properties as well as the overburden stress [*Herbert et al*., 2015]. These and other efforts

demonstrate the powerful insights provided by assessing fault development and interaction using energy criteria [e.g., *Masek and Duncan,* 1988; *Hardy et al.*, 1998; *Burbidge and Braun,* 2002; *Cubas et al.*, 2008; *Marshall et al.*, 2010; *Dempsey et al.*, 2012; *Mary et al.*, 2013; *Yagupsky et al.*, 2014; *Cooke and Madden,* 2014; *McBeck et al.*, 2016]. However, the attempts to quantify the energy budget of physical accretion experiments have thus far focused on one component of the energy budget [*Herbert et al*., 2015]. In addition, the efforts to derive the components of the complete energy budget in numerical wedges use simulations representing the sides of physical accretion experiments observed through the sidewalls [*Del Castello and Cooke,* 2007; *McBeck et al*., in rev.], which may suffer from the influence of sidewall friction. Moreover, these numerical modeling efforts focus on physical accretionary wedges composed entirely of dry sand.

Building from the analysis of the energy required to propagate new thrust faults in a physical accretion experiment [*Herbert et al*., 2015], and the evolution of the complete work budget in numerical simulations of physical experiments [*Del Castello and Cooke*, 2007; *McBeck et al.*, in rev.], we track the complete work budget from the onset of displacement to the formation of the first thrust pair throughout four physical accretion experiments performed at the University of Cergy-Pontoise (UCP). Digital image correlation (DIC) and backwall force measurements enable estimation of the energy expended in uplift against gravity, work done against frictional slip, energy consumed in pervasive off-fault deformation and total external work done in the physical accretion experiments. These quantitative observations also provide constraints on the stress-strain relationship of the physical accretion wedges, which we use to estimate the effective

elastic moduli of the wedges. To assess the impact of detachment strength on energy partitioning, we track the energy budget in physical experiments that include and exclude a basal layer of glass beads. Sliding of the sandpack sides against the apparatus sidewalls exerts shear stresses perpendicular to thrust strike that produce changes in the fault geometry closer to the sidewalls. To remove the influence of sidewall friction on the estimates of work budget components in the physical experiments and numerical simulations, we perform experiments with opposing apparatus configurations.

The rich data gathered throughout the physical experiments enable the robust development of numerical simulations of stages of the physical experiments. To constrain the effective elastic modulus and the friction coefficients of the detachment and thrust faults in the numerical wedges, we exact a misfit analysis that minimizes the differences in both in the normal force exerted on the physical and numerical backwall, and the length of the active detachment preceding faulting. The misfit analysis constrains the appropriate numerical parameters within the ranges of laboratory measurements, minimizing differences between the numerical and physical wedges due to the prescribed value of the material or fault property. Using the resulting elastic moduli and friction coefficients, we track the components of the energy budget in numerical simulations representing potential cross sections of the center, as well as the sides of the physical experiments observed through the glass sidewalls. We assess differences in the evolving work budget within the center and on the sides of the sandpack to gain a more complete understanding of the evolving system efficiency throughout the volume of the physical accretion experiment. Tracking the work budget only within the center or on one side may provide a biased representation of the overall system efficiency if the thrust fault

geometry changes significantly along strike. The evolving energy budget provides insights into how fault development contributes to the evolving efficiency of the system, and how energy partitioning between deformation mechanisms improves our understanding of strain localization and fault development.

3.3. Background

Here, we discuss the evolution of accretion deformation inferred from field observations, physical analog experiments and numerical simulations. We discuss efforts to understand the behavior of accretionary systems using energy criteria with these approaches.

3.3.1. Onset of strain localization in accretionary systems

Field evidence, physical experiments and numerical simulations suggest that discrete faulting occurs after compaction has sufficiently strengthened the wedge so that strain concentrates along discrete thrusts [e.g., *Koyi*, 1995**;** *Ghisetti et al.*, 2016]. The transition from diffuse volumetric contraction to localized strain may lend insight into the timing of new fault propagation at the front of accretionary prisms. Field observations suggest that internal, off-fault deformation within accretionary prisms, such as distributed microcracking and ductile deformation, produce diffuse thickening of strata that accommodates a significant proportion (30-40%) of total shortening [e.g., *Lundberg & Moore*, 1986; *Morgan et al*., 1994; *Morgan & Karig*, 1995; *Moore et al*., 2011]. Recent retro-deformations of seismic profiles from the central Hikurangi Margin suggest that macroscopic thrust faults and folds accommodate <50% of the margin-perpendicular

shortening due to plate convergence [*Ghisetti et al*., 2016]. Similarly, physical accretion experiments reveal distributed layer-parallel shortening prior to localization of slip on faults [e.g., *Mulugeta & Koyi*, 1992; *Koyi*, 1995].

High-temporal resolution experiments capture the initial stages of fault development in physical accretionary wedges. Displacement fields of the sides of physical wedges indicate that short-lived shear bands episodically develop until strain localizes onto a single frontal forethrust [e.g., *Bernard et al*., 2007; *Dotare et al.*, 2016]. These shear bands form near the tip of the detachment, in the region where the frontal forethrust ultimately develops [*Bernard et al*., 2007; *Dotare et al.*, 2016]. Incremental displacement fields of a UCP physical wedge reveal that preceding frontal thrust development, slip along the detachment accompanies horizontal compaction within the wedge, which then promotes forethrust development above the detachment tip [*McBeck et al*., in rev.]. When the curl of the incremental displacement field first reveals localized slip on the forethrust, the curl field remains diffuse in the region where the backthrust forms, suggesting that the forethrust has more slip than the emerging backthrust at this early stage of the experiment.

Seismic imaging of crustal accretion prisms suggests that the partitioning of slip between forethrusts and backthrusts in crustal settings may be similar to the partitioning observed in physical experiments. The majority of tectonic accretionary prisms grow via forward accretion along forethrusts [e.g. *Von Huene and Scholl,* 1991; *Morgan and Karig*, 1995; *Gutscher et al.,* 1998], whereas seismic imaging has revealed accretion via backthrust propagation in only a few prisms [e.g. *McKay et al*., 1992; *Adam et al.,* 2004; *Singh et al.,* 2010]. The correlation of backthrusts within the Cascadia margin with

regions of high rates of glacial sediment input from the Columbia and Frazer rivers led to the postulation that low detachment strength in the southern Washington and northern Oregon portion of Cascadia may drive the development of accretionary backthrusts rather than forethrusts [*Seely*, 1977; *Byrne et al*., 1993; *MacKay*, 1995].

Following the Coulomb failure criteria, diminishing detachment strength should promote slip on backthrusts because as the detachment weakens, the orientation of maximum compression approaches the dip of the detachment [e.g., *MacKay*, 1995]. This shift of maximum compression from oblique to subparallel to the detachment dip decreases the backthrust dip predicted by Coulomb shear failure criteria. This decrease in backthrust dip allows the backthrust to accommodate a larger portion of horizontal shortening, increasing slip. However, the majority of physical analog experiments that include a weak basal layer simulating low detachment strength accrete material through the development of forethrusts [e.g., *Huiqi et al.*, 1992; *Lallemand et al.*, 1994; *Cruz et al.*, 2010]. The physical accretion experiments that provide exceptions to this trend, in which in-sequence backthrusts accommodate convergence, simulate weaker detachments with silicone putty [*Bonini*, 2007], whereas the physical experiments that do not produce in-sequence backthrusts use low friction granular material.

A benchmark study of eleven numerical codes reveals that accretion deformation produced in numerical accretion simulations closely match deformation observed in physical experiments [*Buiter et al*., 2016]. In the eight codes that participated in the benchmark experiment of long-term accretion evolution, deformation initiates as a thrust pair near the mobile wall (backwall) [*Buiter et al*., 2016]. In two of the eight simulations, the forethrust has more slip than the backthrust in the initial thrust pair, consistent with

the higher slip along the forethrust observed in a physical UCP experiment [*McBeck et al.*, in rev.]. After the formation of the first thrust pair, deformation continues with forethrust propagation, or in-sequence thrust pair development, or a combination of these styles [*Buiter et al*., 2016]. Similar to episodic shear band development observed in physical experiments [e.g., *Bernard et al*., 2007; *Dotare et al*., 2016], in the numerical simulations, incipient shear zones form and sometimes fade without fully localizing into discrete thrust faults [*Buiter et al*., 2016]. The similarity in incipient strain localization from shear bands to discrete thrusts, and enhanced slip along the forethrust relative to the backthrust in the numerical simulations and physical experiments suggests that numerical approximations of physical accretion wedges capture the mechanics that control fault initiation and thrust slip partitioning.

3.3.2. Energy budget of accretionary systems

Recent investigations of fracture propagation and interaction in accretionary systems indicate that tracking the evolution of various components of the work budget of a deforming fault system sheds insight into mechanics that control fault development [e.g., *Del Castello and Cooke*, 2007; *Dempsey et al.*, 2012; *Cooke and Madden*, 2014; *Herbert et al*., 2015; *McBeck et al.*, in rev.]. The energy budget of a deforming fault system includes the internal work of deformation, W_{int}, the work of uplift against gravity, W_{grav}, the work done against frictional sliding along fractures, W_{fric}, the work required to create new fracture surfaces, W_{prop}, and the work released as seismic energy, W_{seis}.

The components of the work budget may be calculated using the principle that work equals force applied through a distance [e.g., *Cooke and Madden*, 2014]. The total

external work is the area under the force-displacement curve from the onset of loading to the particular stage of interest. Assuming a linear loading path, the external work of the system may be calculated directly from the shear tractions and displacements, τ and u_s, and normal tractions and displacements, σ_n and u_n, integrated along the boundaries of the system, B, as

$$W_{ext} = \frac{1}{2} \oiint_B (\tau u_s + \sigma_n u_n) dB \qquad \text{Eq. 3.1}$$

The factor of ½ assumes that the system responds linearly, so that an increase in applied boundary displacements (or tractions) produces a proportional increase in tractions (or displacements). If the system does not respond linearly, then the total loading of the system should be applied in multiple loading steps, and the W_{ext} done in each loading step must be summed to constrain the total W_{ext}. In a linear elastic system, the total W_{ext} calculated by integrating over multiple loading steps equals the total W_{ext} calculated using the factor of ½. In a system with frictional sliding faults, the behavior of the system may not be perfectly linear because frictional slip is path dependent. The non-linear trend of physical force-displacement curves [e.g., *Herbert et al.*, 2015] reveal the deviation from linear behavior due to the development of thrust faults, and frictional slip on these faults.

The work of internal deformation surrounding faults, W_{int}, may be calculated from the integral of strain energy density as in a two-dimensional numerical model, in x-y space,

$$W_{int} = \frac{1}{2} \iint \sigma_{xx}\varepsilon_{xx} + \sigma_{yy}\varepsilon_{yy} + \sigma_{xy}\varepsilon_{xy} \, \mathrm{dxdy} \qquad \text{Eq. 3.2}$$

W_{int} calculates the energy of elastic strain, but may also provide an energy source for inelastic processes within physical experiments and the crust.

The work of uplift against gravity, W_{grav}, is a function of the depth of each specified point in the model, d, the upward displacement at each point, U_Y, the acceleration due to gravity, g, and the density of the material, ρ, where x and y are the horizontal and vertical positions and directions,

$$W_{grav} = \iint \rho g d U_Y \mathrm{dxdy} \qquad \text{Eq. 3.3}$$

The contribution of W_{grav} at each specified point is integrated over the column of material overriding the point, which is a rectangle with a height dy and width dx. The depth to the point is dy, and the horizontal spacing between specified points is dx. Contractional systems will produce a net positive W_{grav} and extensional systems will produce a net negative W_{grav} [*Cooke and Madden*, 2014; *Dempsey et al*., 2012]. The sum of W_{grav} and W_{int} is the mechanical work done in the system, which is reversible.

Frictional work, W_{fric}, is the work of fault slip against friction [e.g., *Cooke and Madden*, 2014]. W_{fric} along a single fault segment may be calculated from the shear stress along a fault during sliding, τ, the slip along the fault, s, and the area of the fault that slipped. In this two-dimensional plane-strain formulation, we consider the fault to have one unit dimension in and out of the plane so that fault area is the two-dimensional length of the fault, L. In one loading increment of a numerical model, the work consumed in frictional sliding is integrated over the surface area of the slipped fault,

$$W_{fric} = \frac{1}{2}\int \tau s \, \mathrm{dL} \qquad \text{Eq. 3.4}$$

The energy to grow a new fracture, W_{prop}, is the energy consumed to produce new discontinuities within a material. The energy required to generate new fault surface, W_{prop}, and the energy available for ground shaking, W_{seis}, depend on the shear stress drop, and the amount of slip, s, relative to the slip weakening distance, which is the distance over which shear stress drops from its static to sliding value [*Cooke and Madden*, 2014]. When a fault has not slipped past the slip weakening distance, the energy available for W_{prop} and W_{seis} is fully expended as W_{prop}. In this scenario, W_{prop} is

$$W_{prop} = \oint \frac{1}{2}\Delta\tau\Delta s \, \mathrm{dL} \qquad \text{Eq. 3.5}$$

where $\Delta\tau$ is the shear stress drop ($\Delta\tau = \tau_0 - \tau$), and Δs is the change in slip during the loading increment. When a fault slips beyond the slip weakening distance, the associated work is partitioned between W_{seis} and W_{prop}, as

$$W_{prop} = \oint \frac{1}{2}\Delta\tau s_L \, \mathrm{dL} \qquad \text{Eq. 3.6}$$

$$W_{seis} = \oint \frac{1}{2}\Delta\tau(\Delta s - s_L) \, \mathrm{dL} \qquad \text{Eq. 3.7}$$

where s_L is the slip weakening distance.

Herbert et al. [2015] estimate W_{prop} for fault slip beyond the slip weakening distance in dry sand using force data from physical experiments of accretionary wedges. This

analysis indicates that both material properties and normal stress influence W_{prop} and that relationship between normal stress, σ_n, and W_{prop} is

$$W_{prop}\left(\frac{\mathrm{J}}{\mathrm{m}^2}\right) = 2.0 * 10^{-4}(\mathrm{m})\,\sigma_n(\mathrm{Pa}) \qquad \text{Eq. 3.8}$$

For the physical accretion experiments used in this study, with a 4 cm thick sandpack, this relationship indicates that W_{prop}/A is 0.13 J/m^2 [*Herbert et al*., 2015]. For slip less than the slip-weakening distance of dry sand (2 mm), this value can be linearly scaled as s/s_L.

The sum of the components of the work budget equals the external work of the system:

$$W_{ext} = W_{int} + W_{grav} + W_{fric} + W_{prop} + W_{seis} \qquad \text{Eq. 3.9}$$

Directly calculating W_{ext} provides an alternative way to estimate work terms such as internal work, which are sensitive to sample errors near the stress singularities around fault tips in the numerical solution [*Cooke and Madden*, 2014]. When direct calculation of W_{int} from numerical results is unreliable, W_{int} can be estimated as

$$W_{int} = W_{ext} - (W_{grav} + W_{fric} + W_{prop} + W_{seis}) \qquad \text{Eq. 3.10}$$

Quantifying the evolving energy budget of accretionary systems can help predict the spatiotemporal development of accretion faults [*Del Castello and Cooke*, 2007; *McBeck*

et al., in rev.]. *Del Castello and Cooke* [2007] show that accretionary faults evolve to optimize the total work done in the system, even as individual components of the work budget increase. In these numerical accretion simulations, during underthrusting, W_{grav}, W_{int} and W_{fric} increase, which causes W_{ext} to increase as well. The development of the forethrust increases W_{int}, but decreases W_{fric} by a greater degree, which correspondingly decreases W_{ext} [*Del Castello and Cooke*, 2007]. The development of the forethrust decreases W_{fric} because the forethrust has less overburden thickness than the formerly active underthrust, which provides less resistance to frictional sliding [*Del Castello and Cooke*, 2007]. *Del Castello and Cooke* [2007] also propose that a fault will propagate only when the gain in efficiency exceeds the energetic cost ($W_{prop} + W_{seis}$) of propagating the fault.

Quantifying individual components of the work budget in physical analog experiments provides additional constraints on the impact of fault development on system efficiency. Comparison of the energy expended in the propagation of new fault area, W_{prop}, in UCP accretionary wedges with different thicknesses and built of different materials indicate that W_{prop} is not only a material property, but also depends on normal stress [*Herbert et al*., 2015]. Fault propagation in thicker sandpacks requires larger W_{prop} [*Herbert et al*., 2015]. Fault propagation in physical wedges built of material with lower frictional strength than dry quartz sand (glass beads) requires lower W_{prop} [*Herbert et al*., 2015].

Following this approach, *McBeck et al.* [in rev.] calculate the components of the evolving energy budget in numerical simulations of stages of a UCP experiment immediately preceding and following the development of the first and second thrust pair.

Before any faults develop in the wedge**,** >90% of the total external work is done in internal deformation of the host material, W_{int} [*McBeck et al.*, in rev]. After the first thrust pair forms, W_{fric} and W_{grav} increase as W_{int} decreases. The decrease in W_{int} is larger than the increase in W_{fric}+W_{grav}, causing the total W_{ext} of the system to decrease following fault development. Consistent with *Del Castello and Cooke* [2007], fault development leads to gains in overall efficiency (W_{ext}), as individual components of the energy budget increase (W_{grav}, W_{fric}).

3.4. Methods of physical analysis

Here, we describe the set up and quantitative post-processing of the physical accretion experiments. Then, we describe the method of constraining the effective elastic moduli of the physical wedges and the calculation of the work budget components using observations from the physical experiments.

3.4.1. Design of physical experiments

To gain insight into the impact of fault development on energy partitioning, we estimate components of the energy budget in four physical accretion experiments performed at the University of Cergy-Pontoise (UCP). In these experiments, an electric screw motor translates one wall of an experimental apparatus toward the other in order to contract the dry sand wedge. Throughout the duration of each experiment, three cameras capture photos of different views of the sandpack each second (Fig. 3.1, Fig. 3.2). One camera is positioned above the sandpack and takes photos of the top of the sandpack. Two other cameras are positioned to the sides of the apparatus and take photos through

both of the glass sidewalls of the sandpack cross section. The sets of photos gathered from the cameras allow three views of accretion deformation throughout the experiment (Fig. 3.1, Fig. 3.2). In addition, uniaxial strain gauges mounted on the backwall of the experimental apparatus record changes in normal force exerted on the backwall throughout the experiment. Previous physical experiments performed at UCP indicate that variations in normal force on the backwall occur coincident with fault development [e.g., *Herbert et al*., 2015; *Souloumiac et al.*, 2012].

To construct the homogeneous sandpack, a sedimentation device, designed and built at UCP, sieves the sand two or three times before deposition [*Maillot*, 2013]. The sand deposition method strongly controls the frictional properties of the system, and thus how the sandpack accommodates strain [e.g., *Krantz,* 1991; *Lohrmann et al.*, 2003; *Maillot*, 2013]. The UCP sedimentation device produces homogeneous, isotropic and dense sandpacks consisting of planar layers [*Maillot*, 2013].

In this study, we constrain the evolving work budget in four accretion experiments performed at UCP (Fig. 3.3). To investigate the impact of a weaker detachment on the evolution of the energy budget, two of the experiments include a 0.5 cm thick layer of glass beads, while the other two experiments do not include this layer. In the experiments including the basal glass bead layer, a 3.5 cm thick layer of CV32 sand overlies a 0.5 cm thick layer of glass beads. In the experiments excluding the glass bead layer, the initial rectangular sandpack is a 4 cm thick layer of sand. For both experiments, we add a protowedge of sand on top of the rectangular sandpack to concentrate deformation away from the backwall of the experimental apparatus. The protowedge slope is the angle of repose of the sand (30°), and the base of the protowedge is 10 cm long.

The two experiments that either include or exclude the glass bead layer are identical except for the configuration of the experimental apparatus, which we modify in order to remove the bias in experimental observations arising from sidewall friction [e.g., *Souloumiac et al*., 2012]. Frictional sliding of the sides of the sandpack along the glass sidewalls produces a net force vector that has a different direction depending on whether the base is fixed or moving [*Souloumiac et al*., 2012]. The drag of the sidewall produces a curvature in the strike of thrusts that is expected to be concave to the motor direction. The magnitude of the curvature in the thrust strike depends on the amount of lubricant applied to the glass sidewalls and base, and the proportion of the sandpack in contact with the base and in contact with the sidewalls [*Souloumiac et al*., 2012]. By switching the position of the backwall with respect to the motor, we can change the direction of the sidewall friction drag. By synthesizing observations from experiments with opposing sidewall friction force vector directions, we remove the bias in the experimental observations that arise from sidewall friction.

In two experiments (E373, E374), the glass base slides under the fixed backwall (Fig. 3.3A). In the other experiments (E375, E376), the glass base of the apparatus is fixed, and the screw motor pushes the backwall so that the sand slides over the stable glass base (Fig. 3.3B). In the remaining text, we will refer to the different configurations as the moving base (E373, E374) and moving backwall (E375, E376) experiments. The opposing apparatus configurations are expected to produce only minimal differences in the position of the thrusts with respect to the backwall at the sides of the experiment because the proportion of the area of the sandpack in contact with the sidewalls and in contact with the base is low (~8/100) in these experiments [*Souloumiac et al.*, 2012].

Souloumiac et al. [2012] find that when this ratio is <0.1, the influence of sidewall friction produces negligible changes in the thrust geometry along-strike. Consequently, the opposing configurations are expected to produce minimal changes in the calculated work budget components.

3.4.2. Physical incremental displacement fields

To identify regions undergoing diffuse compaction and constrain the active fault geometry throughout each experiment, we use digital image correlation (DIC) to calculate the incremental displacement field of the top and sides of the sandpack (Fig. 3.2). For every two sequential photos, particle image velocimetry analysis determines the instantaneous displacement field at a grid of points through the DIC of pixel constellations [e.g., *Adam et al*., 2005; *Hoth*, 2005]. The incremental displacement fields aid identification of active thrusts because slip along thrusts produces sharp gradients in the displacement field (strain) (Fig. 3.2). Broad regions of incremental displacement gradients can indicate regions in the wedge undergoing diffuse compaction or distributed shear.

From the incremental displacement fields, we calculate the incremental curl fields of each of the views of the sandpack. The incremental curl field reveals rotation, and high rotation indicates localized slip along thrust faults. The curl field may be calculated from the incremental displacement (velocity) field, $\boldsymbol{U}$, as the cross product of the gradient operator with $\boldsymbol{U}$:

$$\nabla x U = \left(\frac{\partial U_y}{\partial x} - \frac{\partial U_x}{\partial y}\right)\hat{z} \qquad \text{Eq. 3.11}$$

3.4.3. Physical force measurements

To capture fluctuations in normal force exerted on the physical backwall throughout each experiment arising from strain hardening and softening of the sandpack, as well as the localization of deformation along discrete thrusts, we use 16 uniaxial strain gauges mounted on the backwall. Four plaques each containing four uniaxial strain gauges are connected in series so that the mean strain of the 16 sensors are reported (Fig. 3.4). Throughout each experiment, uniaxial strain is recorded each 0.1 second. Calibration of the strain gauges to known weights produces a linear (R^2=0.99) relationship of machine strain units to applied weights (Fig. 3.4). Following each experiment, the machine strain measurements are converted to weight using the relationship identified in the calibration.

In order to calculate the physical external work using the physical force data, we remove noise from the force data with a median filter. We use a median filter with 31 data points (0.031 mm increments of applied motor displacement) that removes noise without over-smoothing the peaks and troughs of the force curve.

3.4.4. Constraining effective elastic modulus with physical force

Although confined laboratory uniaxial tests indicate that the stiffness of aggregates of sand grains are hundreds of MPa [e.g., *Klinkmuller et al*., 2016], the effective elastic modulus of UCP physical accretionary wedges may differ from the confined laboratory measurements because the top boundary of the physical wedge is unconfined. The unconfined boundary of the physical wedge allows vertical deformation (uplift) of the sandpack that may result in effective elastic moduli that are lower than values found from

confined laboratory tests. In addition, empirical relationships of cone resistance to elastic modulus provide estimates of ~10-50 MPa for aggregates of sand [e.g., *Robertson and Campanella*, 1983; *Baldi et al*., 1981]. Because cone resistance tests are typically more confined that laboratory tests, estimates derived from these tests may be larger than the effective elastic modulus of UCP physical accretionary wedges.

To constrain the effective stiffness of the UCP physical wedges, we use measurements of the physical normal force exerted on the backwall and the incremental displacement fields of the sides of the sandpack. We consider the slope of the resulting stress-strain relationship at 50% of the peak stress as the effective elastic modulus of the physical wedge. We consider this parameter to represent the stiffness of physical UCP wedges, but we acknowledge that contracting aggregates of sand grains are not classical linear elastic systems. The estimates of effective stiffness of the UCP wedges provide an approximation of how the plastic deformation of compacting sand grain aggregates respond to applied contraction.

The applied backwall normal force has an unknown distribution across the height of the sandpack against the backwall. The area of the sandpack that exerts significant normal force on the backwall may range between the height of the rectangular sandpack thickness (4 cm) and the total height of the sandpack in contact with the backwall (9.5 cm). This difference can impact the compressive stresses calculated from force measurements. Consequently, we calculate the effective elastic moduli using a minimum (4 cm) and a maximum (8 cm) range of potential load-bearing height of the sandpack. In the moving base experiments, the potential load-bearing height is likely closer to the height of the rectangular sandpack (4 cm) because the motor displaces the glass wall that

is fixed to the moving base and is in contact with the 4 cm thick sandpack. In contrast, in the moving backwall experiments, the potential load-bearing height is likely closer to the height of the sandpack in contact with the backwall because the motor displaces the backwall directly in this configuration.

The incremental displacement fields of the sandpack sides constrain the incremental horizontal strain. To estimate the cumulative horizontal strain preceding the development of the thrust faults, we sum the incremental strain from the onset of displacement to the stress peak for each side of each experiment. We estimate the incremental strain using the incremental displacements, U_x, calculated through DIC, and the length of the compacting region within the sandpack, L. To identify the compacting region, we examine gradients in the horizontal displacement fields of the sandpack sides, which reveal horizontal compaction within the wedge. We calculate the incremental horizontal strain ($\Delta U_x/L$) done within the compacting region by finding ΔU_x as the difference between the maximum U_x at one end of the compacting region and the maximum U_x at the other end of the compacting region.

An alternative method of estimating the physical effective elastic modulus of the sandpack constrains the effective longitudinal strain at each increment from the applied motor displacement (supp. Fig. 3.1). Because the strain gauge arms flex and accommodate some strain as the motor displaces the base or backwall, the total effective horizontal displacement applied to the sandpack will be smaller than the applied motor displacement (supp. Fig. 3.1A). The magnitude of the strain gauge arm displacement depends on the force exerted on the backwall. Consequently, we can derive a linear relationship between an applied stress and the resulting strain gauge arm displacement

(supp. Fig. 3.1B). To estimate the effective horizontal displacement within an increment of the experiment, we can then subtract the expected strain gauge arm displacement from the applied motor displacement. Considering the displacement of the strain gauge arms using linear calibrations produces stress-strain curves for the sandpack that have negative slopes at 50% of the peak stress (supp. Fig. 3.1C-F). The resulting nonphysical estimates of effective elastic modulus indicate that the calibration of the strain gauge arm displacement to applied stresses was not sufficiently precise to determine the strain gauge arm displacement as the sandpack is loaded. In particular, the calibration overestimates the displacement of the strain gauge arms, which results in underestimates of applied displacement and longitudinal strain, and overestimates of effective elastic modulus. Due the insufficiently precise calibration of the strain gauge arm displacement to an applied stress, we constrain the effective elastic modulus using the observed incremental displacements derived through DIC.

3.4.5. Estimation of physical work budget components

In order to assess the impact of thrust fault development on system efficiency, we estimate the gravitational, frictional and external work at increments of the physical experiments using the 2D incremental displacement field of the wedge cross section calculated from digital image correlation of photos taken through both glass sidewalls, as well as the force exerted on the physical backwall. The motor speed (0.1 mm/s) and rate of photo capture (1 second) should produce incremental displacement fields of 0.1 mm of applied motor displacement. However, we observe inconsistencies in the rate of backwall movement on the order of 0.1 mm of applied displacement by the motor. These

inconsistencies cause the calculated displacement fields to fluctuate from relatively large net displacements to nearly zero net displacements at the frequency of about every other incremental displacement field. The estimates of the physical work budget components depend on the applied normal displacement of the backwall, and the resulting displacement field of the sandpack. In order to compare physical work budget components through each experiment, and between each experiment, we sum sequential incremental displacement fields, producing incremental displacement fields representing 0.2 mm of applied displacement of the motor. This summation reduces discrepancies in the physical work budget estimates that arise from inconsistencies in the rate of applied displacement of the backwall.

To assess the range of each physical work budget component near the increments of interest preceding and following faulting, we find the mean and standard deviation of the work budget components calculated within 0.5 mm of motor displacement of the stage of interest. For the stage preceding fault development, we find the mean and standard deviation of work budget components of the increments preceding 0.5 mm of that stage. For the stage following fault development, we find the mean and standard deviation of work budget components of the increments following 0.5 mm of that stage.

To calculate the change in external work done in increments of the physical experiment, we use the displacement of the motor within that increment (0.2 mm) and the force exerted on the backwall. The total external work done from the onset of applied displacement to the stage of interest is the area under the force-displacement curve. Correspondingly, the external work done in an increment of an experiment may be considered to be the area under the force-displacement curve within that increment. This

area can be approximated as the area of a rectangle with a height equal to the force on the backwall at the beginning of the experiment increment, and a triangle with a height equal to the difference between the backwall force at the end of the experiment increment and the beginning of the increment. The width of both the rectangle and the triangle is the backwall displacement that occurs in the experiment increment (0.2 mm). When we compare the change in external work to the changes in W_{int}, W_{fric} and W_{grav} calculated from the DIC measurements, which record changes in the displacement fields between successive photos, we estimate the incremental physical W_{ext} as the area of the triangle under the load-displacement curve. This value approximates the change in W_{ext} produced in that increment. When the backwall force increases, the physical incremental W_{ext} is positive, and when the force on the backwall decreases, the incremental W_{ext} is negative.

To estimate the physical internal work, W_{int}, done in each increment of each experiment, we use the incremental strain calculated from the DIC displacement fields, and we implement Hooke's elasticity laws in order to estimate the incremental stress from the observed incremental strain field. To reduce the impact of noise within the incremental strain field, we first integrate the incremental strain field for each of the components of the strain tensor. Next, we use Hooke's elasticity laws to convert the integrated strain tensor components to integrated stress tensor components. Hooke's formulations for 2D linear elastic systems relate the components of the stress tensor, σ_{ij}, to the strain tensor, ε_{ij}, by Young's modulus, E, and Poisson's ratio, v, as

$$\sigma_{xx} = \frac{E}{(1-2v)(1+v)}\left[(1-v)\varepsilon_{xx} + v\varepsilon_{yy}\right],$$

$$\sigma_{yy} = \frac{E}{(1-2v)(1+v)}\left[v\varepsilon_{xx} + (1-v)\varepsilon_{yy}\right], \qquad \text{Eq. 3.12}$$

$$\sigma_{xy} = \frac{E}{2(1+\upsilon)} 2\varepsilon_{xy}$$

Poisson's ratio for dry sand has been well-characterized, and ranges from 0.2-0.4 [*Gercek*, 2007]. We set Poisson's ration as 0.2 in the above equations. We use estimates of the effective elastic modulus of the sandpacks from the force measured on the backwall and the incremental strain observed through PIV to specify the Young's modulus in the above equations (1 MPa).

To calculate the gravitational work done in increments of each physical experiment, we use measurements of the density of sandpack produced with the UCP distributor [*Maillot*, 2013], and the vertical incremental displacement fields of the sandpack sides.

The frictional work done along faults in the physical experiment depends on the slip along faults in the physical experiment. We estimate the incremental slip along the physical detachment fault using the horizontal velocity of the sand at the base of the physical experiment calculated through DIC. We constrain the incremental slip along the backthrust and forethrust by integrating the curl rate field near the observed thrusts. In particular, we use the curl field to construct fault maps of each incremental displacement field of each experiment. To build these fault maps, we first identify areas of the sandpack with curl above a critical value (0.001 rad/2s), which indicates localized slip. Next, in order to eliminate noise in the fault maps, we find the subset of the high curl regions that have the degree of connectivity we would expect associated with a thrust fault in the accretion experiment. With the fault maps of connected, high curl regions, we calculate the slip along the thrust as the integral of the curl field.

To calculate the physical frictional work, we assume that the normal tractions on the physical faults closely match the lithostatic stresses. Assessment of normal tractions

produced on faults in the numerical models due to lithostatic loading and 0.5 mm of moving wall displacement reveal <0.05 kPa differences in the normal tractions along the faults produced in the model, and the normal tractions arising only from lithostatic stresses (supp. Fig. 3.2). The difference of 0.05 kPa corresponds to 5-10% of the lithostatic tractions along most of the forethrust, and 5-25% along most of the backthrust. Alternatively, we could use the normal tractions on thrust faults in numerical simulations of stages of the physical experiments to calculate the physical frictional work. However, we wish to isolate the estimates of the physical work budget components from the calculation of the numerical work budget components. In addition, the difference between the numerical normal tractions along the thrust faults and the physical normal tractions could be greater than the difference between the normal tractions derived from the lithostatic assumption and the physical normal tractions.

For each increment of an experiment, the gravitational, frictional and internal work calculated from the incremental displacement field of one side of the sandpack may differ from the work calculated from the opposite side of the sandpack. These differences arise from changes in the fault geometry along strike, as well as in the quality of the incremental displacements calculated through DIC. To derive a representative value of work for each increment of each experiment, we average the work budget values calculated for each of the sandpack sides.

3.4.6. Kinematic compatibility assessment

Due to slight differences in illumination, focal depth and camera positioning between each experiment, and between each side of one experiment, the incremental displacement

field calculated through DIC is more reliable for some experiments than others. To assess the robustness of each velocity field, we calculate the 2D kinematic compatibility field of each velocity field. For each incremental displacement (velocity) field of the sandpack sides, we solve the 2D kinematic compatibility equation at all specified points from the horizontal strain, ε_{11}, vertical strain, ε_{22}, and shear strain, ε_{12}, as

$$K = \frac{\partial^2 \epsilon_{11}}{\partial x_2^2} + \frac{\partial^2 \epsilon_{22}}{\partial x_1^2} - 2\frac{\partial^2 \epsilon_{12}}{\partial x_1 \partial x_2} \qquad \text{Eq. 3.13}$$

If the incremental displacement field is kinematically compatible, there will be no apparent movement of material in and out of the plane due to artificial noise, and K is zero throughout the field. To derive a representative measure of the artificial noise level throughout each displacement field, we find the mean plus one standard deviation of the K field, K^F (supp. Fig. 3.3). We consider displacement fields with K^F above one standard deviation from the mean of the K^F of all the fields as unreliable, and we remove these displacement fields from the calculation of the work budget components. In addition, we use the K^F of each field to apply a weighting scheme in the calculation of the mean and standard deviation of each work budget. The displacement fields with K^F closest to zero, and thus the highest 2D kinematic compatibility, are assigned higher weights. We calculate the weighted mean and standard deviation of each physical work budget component using weights derived from the ranking of the K^F across all the experiments.

Comparing K^F across all the incremental displacement fields from the experiments reveals that most of the incremental displacement fields contain an acceptable amount of artificial noise (Fig. 3.5), which is produced by the insufficient correlation of pixel

constellations between successive photos in the DIC analysis. The incremental displacement fields derived from the photos taken from the camera on the right side of experiment E375 have the highest noise levels, and consequently most of these incremental displacement fields are excluded from the work budget analysis.

3.5. Results of physical analysis

First, we present our correlations of the evolution of the normal force exerted against the backwall and faulting events observed in the top and side view displacement fields. Then we present constraints of the effective elastic modulus of the UCP wedges. Finally, we estimate the work budget components from increments of each physical experiment from the onset of motor displacement to beyond the first force drop.

3.5.1. Relationship of backwall force and faulting events

For each experiment, the normal force exerted on the backwall rises to a local maximum (peak) and falls to a local minimum (trough) coincident with fault development (Fig. 3.6). The three-dimensional view of the physical experiment enables identification of faulting events at the top of the sandpack and at both sides of the experiment (Fig. 3.1., Fig. 3.2). Correlation of the evolving backwall normal force with the three views of the sandpack reveals that for all the experiments, the faults emerge at the top of the sandpack 0.5-1 mm before the force peak, as the force curve transitions from the linear phase to the strain-softening phase (Fig. 3.6). As the force diminishes to a local minimum, fault development is observed at different times on either side of the box.

The local minimum in force occurs 0.5-4 mm after the first evidence of thrust fault development is observed on both sides of the experiment (Fig. 3.6).

3.5.2. Estimation of effective elastic modulus

Constraining the effective elastic modulus with the physical force measurements and incremental displacements yield estimates of effective elastic modulus of 0.57-1.15 MPa, with a preferred estimate of 0.99 MPa (Fig. 3.7). Quantifying the level of artificial noise in the incremental displacement fields with the 2D kinematic compatibility equation indicates that the right side data of experiment E375 have artificially high noise levels (Fig. 3.5). Consequently, we do not derive the stress-strain relationship for the right side data, and only consider the cumulative strain calculated for the left side displacement fields valid for experiment E375. We expect that the effective elastic modulus of each experimental sandpack should be similar to each other because each sandpack is built of the same material, and with the same deposition technique. Because the evolution of force is similar across each of the experiments throughout the development of the first thrust pair (Fig. 3.7A), differences in the effective stiffness estimates arise from the varying evolutions of the incremental horizontal displacement fields within the compacting region of the wedge (supp. Fig. 3.4A-B).

To constrain the elastic moduli of the physical wedges using data from each experiment, we find the tangent modulus at 50% of the peak stress for each experiment. We calculate the tangent with linear relationships between the horizontal change in strain, ε_{xx}, and change in normal stress on the backwall, σ_n, over an interval of 2 mm of backwall displacement at 50% peak stress (Fig. 3.7B). We consider the slope of these lines,

$\Delta\sigma_n/\Delta\varepsilon_{xx}$, to approximate the physical effective elastic modulus of the wedges. For each experiment, differences in the incremental strain field on opposing sides of the experiment produce the range in ε_{xx}. Differences in the potential load-bearing height of the sandpack, from 4 cm to 8 cm, produce the range in σ_n. We expect that the load-bearing height of the sandpack in contact with the backwall is closer to 4 cm for the moving base experiments, and closer to 8 cm for the moving backwall experiments. In the moving base experiments, the motor pushes a glass wall that is in contact with the 4 cm tall sandpack. In the moving backwall experiments, the motor pushes the backwall, which is in contact with the full height of the sandpack and protowedge. A larger portion of the protowedge likely rides passively along on top of the rectangular sandpack in the moving base experiments compared to the moving backwall experiments. In addition, the length of the compacting region, L, in the moving base experiments (20 cm) is twice as long as the moving backwall experiments (10 cm), suggesting that the height of the compacting region (i.e., the load-bearing height) in the moving base experiments should be approximately half as high as the height in the moving backwall experiments.

We calculate three linear regressions in order to account for uncertainty in the load-bearing height of the sandpack. The maximum and minimum load-bearing height of the sandpack (8 and 4 cm) produces best–fit lines with slopes (effective elastic moduli) of 0.57 MPa and 1.15 MPa, respectively. The linear regression through the data using the maximum load-bearing height for the moving backwall experiments, and the minimum load-bearing height for the moving base experiments (i.e., preferred heights), has a slope of 0.99 MPa. The best fit using the preferred heights for each set of experiments has a higher R^2 value (0.78) than the other linear regressions (-0.71). A negative R^2 indicates

that the linear regression fits the data worse than a horizontal line. Consequently, we consider the slope of the linear regression through the preferred heights (0.99 MPa) to provide the best estimate of the stiffness of the physical UCP wedges.

3.5.3. Work budget analysis

In this comparison of energy partitioning in the physical experiments, we estimate the energy expended or consumed in increments of displacement throughout each physical experiment. Each physical work budget component discussed is an incremental work budget component, rather than the total energy expended or consumed through the corresponding deformation mechanism from the initiation of contraction to the stage of interest. Consequently, the incremental work is the change in force multiplied by the incremental displacement. The energy budget at each increment of the physical experiments indicates that thrust fault development reduces the external work (incremental W_{ext}<0), reduces the incremental internal work, and increases the incremental frictional work and gravitational work (Fig. 3.8).

To investigate energy partitioning preceding and following faulting, we track the evolving physical energy budget throughout the development of the first thrust pair. In addition, we focus on the energy budget of the physical experiment before faults are observed in the top view of the sandpack (pre-faulting), and after the faults propagate at the sides of the experiment (post-faulting). We consider the pre-faulting stage of each experiment as the increments immediately preceding the observation of fault development at the top of the sand pack. We consider the post-faulting stage of each experiment as the increments at the trough in the force drop. At the force trough, the

faults are more fully localized across the width of the sandpack than in the increments of the experiment immediately after we observe their formation at the sides of the experiment.

The physical incremental external work, W_{ext}, rises from the onset of displacement to ~0.8 mJ, and then begins to fall preceding thrust fault development (Fig. 3.8A-B). This decrease corresponds to the onset of strain softening as the backwall force curve deviates from its initial linear trend at the onset of loading. After the faults are observed at the top of the sandpack (pre-faulting stage), the incremental W_{ext} becomes negative, indicating that the normal force on the backwall decreases. Following the force peak, the incremental W_{ext} becomes less negative. At the force trough, the incremental W_{ext} is close to zero, indicating relatively constant force on the backwall. The greatest incremental W_{ext} is done within 2 mm of the onset of backwall displacement, corresponding to the steepest portions of the force-displacement curve.

The physical incremental internal work, W_{int}, is elevated preceding thrust fault development, and falls as the thrusts develop (Fig. 3.8C-D). For each experiment, the most off-fault deformation occurs immediately preceding thrust fault development. The highest estimates of W_{int} are produced in the experiments with the highest measures of artificial noise in the displacement field (supp. Fig. 3.5), as determined by the kinematic compatibility criterion (Fig. 3.5). This correlation suggests that the estimation of W_{int} is more sensitive to the amount of noise in the incremental displacement fields compared to the other work budget components. Previous results suggest that internal work decreases with the onset of thrust faulting [*Del Castello and Cooke,* 2007; *McBeck et al.*, in rev.]. However, the consistently positive incremental W_{int} here suggests that internal work

monotonically increases throughout the experiment. The rate of increase in W_{int} decreases following thrust faulting.

For each experiment, thrust fault development increases W_{fric}. However, the change in incremental W_{fric} due to thrust fault development is larger in the experiments excluding the glass bead layer (1.04 mJ) than the experiments including the glass bead layer (0.83 mJ) (Fig. 3.8E-F). Preceding thrust fault development, the W_{fric} of the experiments including and excluding the glass bead layer are roughly equal (Fig. 3.8F). Following thrust fault development, the mean W_{fric} is larger in the experiments excluding the glass bead layer than the experiments including the glass bead layer.

For all the experiments, fault development increases the gravitational work (Fig. 3.8G-H). Although the mean W_{grav} at the stage preceding faulting is roughly equal to the mean W_{grav} at the stage following faulting, W_{grav} reaches its maximum levels as strain localizes along the thrust faults, before the force trough. For each experiment, W_{grav} is close to zero from the onset of motor displacement to ~6 mm of displacement. After this point, W_{grav} gradually increases as the thrust faults form. After thrust fault formation, W_{grav} remains elevated at ~1 mJ.

Prior to faulting, the increasing external work applied to the wedge is accommodated with increasing internal work, increasing uplift against gravity, and increasing work against frictional sliding along the detachment. The frictional and gravitation work budget components reach a peak in rate of increase with the minimum in incremental external work, which corresponds to the peak in backwall normal force. The development of the thrust faults decreases W_{ext}, and increases W_{int}, W_{fric} and W_{grav}.

3.6. Discussion of physical analysis

Synthesizing quantitative observations from physical experiments enables a robust analysis of energy partitioning. The incremental displacement fields of the top and sides of the sandpacks and force exerted on the physical backwall provide critical data that allow the estimation of the components of the evolving energy budget in physical accretion experiments. These data also help constrain the elastic moduli of the physical wedges. Here, we discuss efforts to estimate the effective elastic modulus of the physical wedges. We also discuss the evolving work budget of the physical accretion experiments.

3.6.1. Elastic moduli of accretionary wedges

These estimates of the effective elastic moduli (~1 MPa) exceed previous estimates (0.11-0.25 MPa) of the effective elastic moduli of wedges built with an UCP depositor [*Herbert*, 2014]. These estimates may be larger because the experiments presented here used the larger UCP depositor (~1.5mx1.5 m base), whereas *Herbert* [2014] use the smaller UCP depositor (0.65mx0.245 m base) to construct the analyzed sandpacks. The larger UCP depositor may produce sandpacks with more closely packed sand grains than the smaller depositor. Closer packing of grains would elevate the initial resistance of the sandpack to applied loads, and the effective bulk stiffness, because more densely packed grains inhibit grain rearrangement. Tests with the smaller UCP depositor demonstrate that the diameter, spacing, and number of holes in the depositor sieves, and the distance between the sand reservoir, adjacent sieves and the experimental box influence the resulting sandpack density and planarity [*Maillot*, 2013]. The density of sandpacks

produced by the larger depositor have not been systematically compared to the density of sandpacks produced by the smaller depositor.

Uniaxial laboratory uniaxial compression tests of dry sand aggregates produce estimates of elastic moduli that exceed the estimates derived from these UCP experiments. The stress-strain relationship of dry sand in uniaxial compression tests with 50 loading-unloading cycles indicate that the apparent elastic moduli range from 100-400 MPa in the first cycle, to 700-1500 MPa in the 50^{th} cycle [*Klinkmuller et al*., 2008, 2016]. These tests suggest that 50-90% of the total strain in the first loading cycle is inelastic compaction of the aggregate of sand grains as the packing of the sand grains change [*Klinkmuller et al*., 2008, 2016]. However, the estimates of bulk elastic moduli from these uniaxial compression tests will likely exceed the effective elastic modulus of physical wedges. Whereas the physical sandpack is unconfined, so that the top of the sandpack is free to uplift, *Klinkmuller et al*. [2016] constrain the elastic modulus of aggregates of sand grains using a steel jar with 10 mm thick steel walls that prevent the sand from deforming laterally. If the upward movement of the sand grains were restricted in the physical experiment, the applied normal displacement would produce greater normal force on the physical backwall than in the present unconfined configuration, producing higher estimates of effective elastic modulus.

Geotechnical engineering studies provide additional constraints on the expected effective elastic modulus of aggregates of sand grains [e.g., *Roberston and Campanella,* 1983]. Empirical relationships derived from normally consolidated sand produce estimates of effective elastic modulus at 50% failure stress from 10-50 MPa [*Baldi et al.,* 1981]. These estimates may remain higher than the effective elastic modulus of the UCP

physical accretionary wedges because they require some confining stress to keep the sand within the experimental apparatus.

In contractional confined laboratory experiments and physical accretionary wedges, force chains throughout the aggregate of sand grains resist applied contraction. When the experiment is confined, the confining walls limit the rearrangement of the sand grains and corresponding force chains. In contrast, in the physical accretion experiments, the sandpack can thicken perpendicular to the applied load, which allows constant reconfiguration of the force chain network. The longer-lived force chain network in the confined laboratory experiments cause the bulk measured stiffness to reflect the individual sand grain stiffness (i.e., quartz). Because the force chain network constantly evolves in the physical accretion experiments, the signal of grain rearrangement dominates the measured bulk stiffness to a greater degree than the stiffness of quartz.

3.6.2. Physical work budget evolutions

Assessing the tradeoffs of diverse deformation processes within the energy budget framework enables quantification of the impact of fault development on system efficiency. The incremental energy budget of the physical experiments indicate that fault development increases W_{int}, W_{fric} and W_{grav}, while decreasing W_{ext}. Thrust development increases fault length, increasing W_{fric}. Upward motion between the thrust faults increases uplift, increasing W_{grav}. Slip along the faults localizes strain so that the system becomes more efficient, reducing W_{ext}. Previous analyses of the work budget of other deforming numerical and physical accretionary wedges identified similar energy budget evolutions [*Del Castello and Cooke*, 2007; *McBeck et al.*, in rev.]. These analyses found that thrust

fault development reduces the energy consumed in off-fault deformation, whereas our new analysis indicates that internal work consistently increases throughout the development of the first thrust pair (positive incremental W_{int}). However, consistent with these previous analyses, the rate of internal work increase, incremental W_{int}, decreases following thrust development.

The vertical displacement fields of the sides of the physical sandpacks demonstrate that diffuse uplift precedes the development of discrete thrusts (Fig. 3.9). The evolution of the physical W_{grav} (Fig. 3.8) captures and quantifies the broad uplift preceding thrust development, and localization of uplift following thrust development (Fig. 3.9). At the onset of applied displacement, limited uplift accommodates the applied displacement, and W_{grav} is close to zero. After this initial stage, broad uplift increases W_{grav}, and then as diffuse shear bands evolve into localized thrust faults, W_{grav} decreases. After thrust fault formation, W_{grav} remains elevated at ~1 mJ because the thrust faults continue to promote uplift.

The increase in W_{fric} following thrust fault development (Fig. 3.8) illuminates the influence of thrust slip partitioning on energetic evolution within the physical accretion experiments. Thrust fault development produces greater increases in mean W_{fric} in the experiments excluding the glass bead layer (1.04 mJ), than the experiments including the glass bead layer (0.83 mJ). The curl of the incremental displacement fields of the physical experiments excluding the glass bead layer show clear evidence of localized slip on the backthrust at the force trough of the experiment (Fig. 3.10A). However, in the experiments including the glass bead layer, the curl rate is lower in the backthrust region at the force trough (Fig. 3.10B). The reduced slip on the backthrust in the experiments

including the glass bead layer diminishes the increase in W_{fric} arising from thrust fault development. The entrainment of glass beads at the root of the forethrust promotes slip on the forethrust at the expense of the backthrust (Fig. 3.10C). The incremental displacement fields of the physical experiments and the evolution of the physical W_{fric} captures differences in slip partitioning between the thrusts in the experiments including and excluding the glass bead layer.

In contrast to the predictions of *MacKay* [1995], reducing the strength of the physical detachment does not promote slip on the backthrust in these physical accretion experiments. Instead, the evolving curl of the incremental displacement fields of the sandpack sides indicate that reducing the strength of the detachment suppresses slip on the first backthrust that develops in the wedge (Fig. 3.10). This result is consistent with previous physical accretion experiments that simulate low detachment strength using granular material, and that do not observe a preference for backthrust development and slip over forethrust activity [e.g., *Cruz et al*., 2010]. These physical accretion experiments indicate that low detachment strength is not sufficient to promote accretion growth via backthrusting. This inference, as well as the observed backthrusting in physical accretion experiments that use silicone putty to simulate low detachment strength [e.g., *Smit et al.*, 2003; *Bonini*, 2007] suggest that other processes associated with high levels of sediment input, such as fluid expulsion from sediments resulting in volumetric contraction, may promote backthrusting. The observed difference between the preferred thrust vergence in experiments that simulate low detachment strength with granular material compared to experiments using viscous material may arise in part from the ability of the granular material to become entrained at the root of the thrusts, and the limited advection of the

silicone along the thrusts. The entrainment of the granular material at the root of the forethrust may promote slip on the forethrust, subsequently decreasing slip on the backthrust. This entrainment suppresses localized slip on the backthrust in part because it creates a smoother transition zone at the root of the thrusts.

We estimate the incremental internal work by integrating the strain field outside of the fault zones at each experiment increment. Tracking the evolution of the integrated strain tensor components provides insight into how different expressions of off-fault deformation, such as volumetric compaction and shear strain, contribute to W_{int} (Fig. 3.11). Preceding faulting, the wedge experiences increasing horizontal contraction and increasing vertical extension, while shear strain remains relatively constant (Fig. 3.11). In the experiments with the lowest estimates of artificial noise (E376, E375), the evolutions of the integrated strain tensor components indicate that increasing normal strains drive the increase in W_{int} immediately preceding thrust fault development, whereas off-fault shear strain provides smaller contributions. The development of the thrust faults reduces the off-fault horizontal contraction and vertical extension. These reductions suggest that the decreasing magnitudes of normal strains cause the decrease in the rate of internal deformation of the host material following fault development, and the corresponding reduction in incremental W_{int}.

Analyzing the integrated strain tensor components throughout the entire displacement field, including within the detachment and thrust fault zones, sheds insight into the impact of fault development and slip on the complete strain field (Fig. 3.12). Preceding faulting, the complete wedge experiences increasing horizontal contraction and increasing vertical thickening, similar to the evolution of the off-fault strain field (Fig.

3.11). Including the contribution of detachment slip causes the integrated shear strain to rise preceding thrust fault development. The development of the thrust faults causes the total horizontal contraction and shear strain to plateau. The relatively constant rate of horizontal contraction throughout the development of the thrust faults indicates that as contraction localizes from diffuse zones onto discrete thrusts, the total rate of horizontal contraction remains constant, despite the localizing spatial distribution. The total vertical dilation increases as the faults develop and then plateaus when the faults are more fully localized. The evolution of the integrated ε_{yy} is similar to the evolution of W_{grav} (Fig. 3.8) because the vertical displacement within the wedge contributes to both the integrated ε_{yy} and W_{grav}. Correspondingly, the evolution of the integrated ε_{yy} and W_{grav} reflect the broad uplift preceding faulting, and the concentration of uplift along thrust faults following thrust development. The evolution of the integrated ε_{xy} is similar to the W_{fric} evolution (Fig. 3.8) because fault slip increases both the integrated ε_{xy} and W_{fric}.

The incremental normal and shear strain fields as the thrusts develop (Fig. 3.13) provide further insight into the evolutions of the normal and shear components of the strain field outside of the fault zones (Fig. 3.11), and including the fault zones (Fig. 3.12). Preceding thrust faulting, high normal strains are dispersed through the wedge, while slip along the detachment localizes shear strain. With continued backwall displacement, horizontal contraction and vertical extension shift toward the region where the thrusts ultimately develop, and the zone of high shear strain surrounding the detachment extends further from the backwall. In the incipient stages of thrust development, horizontal contraction and vertical extension concentrate along the incipient thrusts, forming broad bands of high strain a few centimeters thick. At this stage, elevated zones of shear strain

highlight slip along the thrust faults. As strain continues to localize along the thrusts, the zones of high horizontal contraction and vertical thickening decrease in width. Shear strain along the forethrust increases while shear strain along the backthrust remains low. These detailed observations of strain localization preceding and throughout thrust fault development provide insight into fault development in these physical accretionary experiments. In addition, these observations suggest that similar precursors may arise in crustal accretionary wedge prior to discrete thrust fault development. This analysis of the evolving work budget and incremental strain field of physical accretionary wedges suggests that these precursors enhance the off-fault deformation within the wedge, and may include distributed micro-cracking, layer-parallel shortening, and fluid expulsion due to volumetric compaction.

3.7. Conclusions of physical experiment analysis

This study compares the energetic tradeoffs of frictional slip, uplift and distributed off-fault deformation in increments of physical accretion experiments in order to shed insight on the impact of fault development of diverse deformational processes within tectonic environments. Constraining the evolving physical energy budgets reveals that thrust fault development increases the overall system efficiency, producing smaller (and negative) changes in external work. The evolution of gravitational work in increments of the physical experiments highlights the broad uplift that begins prior to slip on localized thrust faults. Variations in the physical frictional work track the advance and retreat of the physical detachment and reveal differences in slip partitioning between the backthrust and forethrust in the experiments including and excluding the glass bead layer. Low slip

on the backthrust in the experiments including the glass bead layer, relative to the experiments excluding the glass bead layer, suppresses the increase in frictional work arising from thrust fault development.

3.8. Introduction to numerical analysis

Although the force measured on the backwall of the physical experiments constrains the evolving stress state within the wedge, with numerical simulations of the physical UCP wedges we may more directly assess the impact of fault development on pervasive internal deformation because we can sample the stress field throughout the numerical wedge. Previous investigations indicate that the energy consumed in off-fault deformation (W_{int}) comprises 50-90% of the total work done in numerical accretionary wedges preceding and following faulting, and consequently plays a critical role in assessing evolving system efficiency [*Del Castello and* Cooke, 2007; *McBeck et al.*, in rev.]. To better understand the transition from pervasive internal strain to localized slip along discrete faults, we must constrain the evolution of W_{int} as strain localizes. To assess the impact of diffuse deformation (W_{int}) on fault development and system efficiency, we develop numerical simulations of two stages of each physical UCP experiment: immediately preceding and following the development of the first thrust fault pair. The numerical simulations of stages of the physical experiments enable a more nuanced investigation of the sensitivity of the work budget to fault geometry, and material and fault properties than the analysis of the evolving physical work budget. Whereas unaccounted variations may persist between the physical experiments and lead to changes

in the work budget, differences in the work budgets of the numerical simulations arise only from prescribed differences.

3.9. Methods of numerical analysis

To help ensure that the numerical simulations closely capture the deformation observed in help physical experiments, we build the numerical fault geometries using the incremental displacement fields of both sides of the sandpack, as well as the top of the sandpack, and we constrain the numerical material and fault properties using the normal force exerted against the physical backwall and the observed length of the physical detachment. The incremental displacement field of the top of the sandpack constrains the fault geometry within the along-strike center of the sandpack, which is not as strongly influenced by sidewall friction as the fault geometry observed through the glass sidewalls. We search for the elastic modulus and detachment and thrust friction coefficients that minimize the misfit in the force exerted against the numerical and physical backwall, and the difference in the length of the slipping portion of the numerical and physical detachment fault.

3.9.1. Fric2D numerical simulations

We simulate two stages of the UCP accretion experiments with the two-dimensional, plane strain, linear elastic, Boundary Element Method (BEM) modeling tool Fric2D [*Cooke and Pollard*, 1997]. Fric2D solves the quasi-static equations of deformation to determine the displacements and tractions on each element and at specified points within the model, produced by a given set of boundary conditions and fracture geometry [e.g.,

Cooke and Pollard, 1997; *Cooke and Murphy*, 2004; *Cooke and Madden*, 2014]. The BEM approach of Fric2D only requires the discretization of fractures and boundaries, which are comprised of linear elements that may not interpenetrate. Additionally, Fric2D 3.2.7 can simulate slip-weakening behavior along pre-existing fractures and/or potential growth elements [*Savage and Cooke*, 2010]. As an element slips to a prescribed slip-weakening distance, the coefficient of friction along that element evolves linearly from its static, μ_s, to its dynamic value, μ_d.

The numerical simulations employed in this analysis represent cross sections of the physical accretion experiment sandpacks. The boundaries of the numerical model include the edge of the sandpack against the backwall, the topography of the wedge, the edge of the wedge against the fixed front wall, and the base of the wedge (Fig. 3.14). To simulate contraction in the numerical wedges, we apply displacement to the numerical backwall, simulating the moving backwall experiments. The numerical wedge includes a frictional sliding detachment fault located 1 cm above the modeled base that spans the length of the modeled sandpack from the backwall to the right fixed wall. The topography of the numerical wedge is derived from the topography of the physical wedge observed through the glass sidewalls at the simulated increments of the experiment. In the numerical simulations of the post-faulting stage, we include two planar thrusts in the model that represent a thrust fault geometry near the along-strike center of the sandpack. To assess the impact of along-strike changes in fault geometry on the energy budget, we build numerical models that represent the sides of each experimental sandpack. The models of the sides of the experiments are derived from fault geometries directly observed through the glass sidewalls.

3.9.2. Stages of faulting in experiments

The normal force exerted on the backwall rises to a local maximum (peak) and falls to a local minimum (trough) coincident with fault development (Fig. 3.6). For each experiment, we initially observe fault development at the top of the sand pack <1 mm before the peak in the force curve, and then we observe fault development at the sides of the sandpack immediately after the force peak, and before the force trough. To investigate energy partitioning preceding and following faulting, we simulate the physical experiment before faults are observed in the top view of the sandpack, and after the faults propagate at the sides of the experiment. To ensure that the post-faulting numerical simulations represent the stage of the physical experiments in which the faults are fully localized across the width of the sandpack, we use the fault geometry observed at the trough of the force curve to develop the numerical fault geometries.

3.9.3. Development of numerical simulation thrust geometries

We synthesize observations from the three cameras into a two-dimensional fault geometry that represents the fault geometry at a cross section within the center of the sandpack. To specify the position and dips of the backthrust and forethrust in each numerical simulation, we rely on the incremental displacement fields of the top and sides of the sandpack.

For each experiment, we use the horizontal incremental displacement field of the top of sandpack to constrain the along-strike position of the backthrust and forethrust at the increment of the experiment closest to the force trough. We calculate the horizontal

distance from the intersection of the thrust with the top boundary of the sandpack to the edge of the sandpack against the backwall (i.e., thrust position) in sub-millimeter increments along the strike of each thrust fault. The resulting set of positions provides a rich representation of the along-strike changes in thrust geometry. To quantify the range of thrust positions along strike, we construct histograms of the distance between the backthrust and forethrust position along strike observed in each experiment (Fig. 3.15).

Comparison of the distance between the mean thrust positions within the center 20-80 cm (dark gray) of the sandpack and outside the center 5-95 cm (light gray) of the sandpack indicates that the distance between the thrusts increases from the center toward the sidewalls (Fig. 3.15). This observation reveals that the thrusts have steeper dips within the center of the sandpack than the thrusts observed through the glass sidewalls.

To estimate the thrust dips within the center of the sandpack, we use the mean thrust position within the center 20-80 cm of the sandpack. We set the thrust positions in the numerical models as the observed mean positions within the center of the experiment, and find the position of the thrust root as the average of the root position of 1) a backthrust at the mean backthrust position and with the dip of the backthrust observed through the sidewalls and 2) a forethrust at the mean forethrust position with the dip of the forethrust observed through the glass sidewalls (Fig. 3.16). The resulting numerical thrust dips are steeper than the dips observed through the glass sidewalls by 1-3° (Fig. 3.16).

3.9.4. Misfit analysis

To determine the appropriate material and fault properties used in the numerical simulations, we identify the combination of effective elastic moduli and friction coefficients that minimize the misfits both between the force exerted on the numerical backwall and the physical backwall, and between the extent of slip on the numerical detachment and physical detachment. This two-step misfit analysis identifies a combination of effective stiffness, and detachment and thrust frictions that enable the normal force exerted against the backwall in the numerical simulations to closely match the normal force measured in the physical experiment at the stages preceding and following fault development, as well as allow the detachment fault in the numerical simulations to slip to the lengths observed in the physical experiments. In this way, the model parameters are tuned so that the boundary forces and displacements match the observations from the physical experiments. The linear elastic properties of the numerical simulations may neglect the inelastic processes within the deforming sandpack. Calibrating the simulations to experimental conditions allows the simulations to approximate the neglected processes.

In the pre-faulting step of the analysis, we search for the elastic modulus, and friction coefficient of the detachment fault that minimize the misfits in force and detachment length preceding fault development. In the post-faulting step of the analysis, we search for the elastic modulus, and static and dynamic friction coefficients of the thrust faults that minimize the misfit in force following fault development. Measurements of the static and dynamic friction of sand aggregates on a hard surface coated with Alkor foil indicate that the magnitudes of basal static and dynamic friction are comparable [*Klinkmller et al*., 2016]. Consequently, we prescribe only one friction value to the detachment. In contrast,

the slip behavior of the thrust faults will include distinct weakening from static to dynamic friction, over a slip-weakening distance of 0.1 mm for CV32 sand grains. We are not able to minimize the misfit in the detachment length in the post-faulting step of the misfit analysis because the maximum length of the active detachment in the numerical wedges is set by the position of the thrust faults included in the model.

In the physical experiment, we do not expect the detachment friction properties to change following the thrust development. Consequently, in the post-faulting step of the misfit analysis, we use the detachment friction identified in the pre-faulting step of the analysis. Similarly, the effective elastic modulus of the sandpack should not change significantly following fault growth. Although additional compaction of the sand may increase the stiffness of the wedge, dilation related to thrust fault development could reduce the effective elastic modulus of the sandpack. Because both of these influences are likely to be small relative to the bulk stiffness of the wedge, we use the effective elastic stiffness identified within the pre-faulting step of the analysis in the post-faulting step.

Although laboratory strength measurements provide estimates of the static and dynamic friction of thrust faults formed in dry granular material [e.g., *Lohrmann et al.*, 2003], fewer measurements constrain the static and dynamic friction of thrust faults formed in UCP experiments, which may differ from other laboratory measurements due to the unique UCP sandpack deposition method [*Maillot*, 2013]. Even fewer laboratory measurements constrain the effective elastic modulus of physical UCP wedges [*Herbert*, 2014] and the friction coefficients of the detachment fault.

In the physical accretion experiments, the physical detachment fault facilitates slip between sand grains and polished glass, or between glass beads and polished glass.

Measurements of the dynamic basal frictional strength of dry quartz sand on Alkor foil vary from 11.5-19º (0.20-0.32) [*Klinkmuller et al*., 2016]. Measurements of the dynamic basal frictional strength of glass beads on Alkor foil vary from 12-16° (0.20-0.26) [*Klinkmuller et al*., 2016]. Estimates of the basal dynamic friction of sand sifted or poured onto paper in a Hubbert-type shear box indicate that the sifted sand has higher basal dynamic frictions (0.48-0.53) than the poured sand (0.45) [*Lohrmann et al.*, 2003]. The higher estimates of dynamic basal friction found between sand and paper in this experimental set up (0.45-0.53) [*Lohrmann et al.*, 2003] compared to the lower ranges of dynamic basal friction found between sand and Alkor foil (0.20-0.32) [*Klinkmuller et al*., 2016], highlights that the material on which the sand is sliding influences the basal static friction. The dynamic strength of the physical detachment in UCP experiments may be less than these previous estimates of basal friction because the polished glass of the experimental apparatus base may provide less resistance to slip than other basal surfaces, such as paper and Alkor foil.

To compare the numerical backwall force to the backwall force measured in the physical experiments, we average the measured backwall force of the physical experiments with the differing box configurations. We use the difference in the forces of the two experiments with differing box configurations to define a range to which to minimize the numerical force. This average removes the effects of sidewall friction in the comparison of the force measured on the backwall in the 2D numerical simulations and 3D physical experiments. In the pre-faulting step of the misfit analysis, we vary the elastic modulus between 0.2-1.0 MPa, and the friction of the detachment fault from 0-0.4. In the post-faulting step of the misfit analysis, we use the detachment fault friction and

elastic modulus identified in the first step, and we vary the static and dynamic coefficient of friction of the thrust faults from 0.1-0.7. We specify that the static friction of the thrust faults must be greater than the dynamic friction. The range in elastic moduli includes values derived from the stress-strain relationship of the experiments. The range in detachment and thrust frictions encompass values measured in laboratory strength measurements [e.g., *Klinkmuller et al*., 2016].

To compare the numerical backwall normal force and active detachment length to the physical force and detachment length, we report the difference in the numerical and physical property as a fraction of the physical property. In particular, the misfit, *M*, in the numerical model property, *N*, and the physical property, *P*, is

$$M = (N - P)/P \qquad \text{Eq. 3.14}$$

With this formulation, positive misfit indicates that the numerical wedge overestimates the normal force on the physical backwall or the observed detachment length. Negative misfit indicates that the numerical wedge underestimates the physical property.

3.9.5. Work budget of numerical wedges

Similar to the physical work budget analysis, we calculate the gravitational work, frictional work, internal work and external work done in the numerical simulations. We apply 10 loading steps to the numerical wedges to ensure that the work budget captures any non-linear behavior introduced by frictional slip. During these loading steps, the

model is initially undeformed, and subsequently loaded to 0.5 mm of total displacement, and the effective friction of each thrust fault evolves with slip. To compare energy partitioning in the numerical simulations of the sides and center of each experiment, we calculate each work budget component throughout all of the applied loading steps.

To compare the work budget of the numerical simulations to increments of the physical experiments, we assess differences in the work done in the final (10^{th}) increment of the numerical simulations to the work done in each increment in the physical experiments. The energy expended or consumed in the final increment best reflects the incremental work done at the corresponding increment of the physical experiment because the faults have slipped beyond the prescribed slip-weakening distance in both the numerical simulation (supp. Fig. 3.6) and the physical experiment. Consequently, the non-linear behavior introduced by slipping faults is negligible, which allows increases in applied displacements to produce nearly proportional increases in stresses. This proportionality enables the scaling of the incremental work done in the final increment of each numerical simulation by the ratio of the displacement applied in the final numerical increment (0.05 mm) and the displacement applied by the motor in the increments of the physical experiments (0.2 mm). This scaling is required to compare the physical work budget components to the numerical work budget components because each work budget component depends on the amount of displacement applied to the system.

3.10. Results of numerical analysis

First, we present results of the two-step misfit analysis that constrain the elastic moduli, E, and static, μ_s, and dynamic, μ_d, coefficients of the detachment and thrust faults

in the numerical simulations. Next, we calculate the work budget components of the numerical simulations, and compare the estimates of the physical and the numerical work budget components.

3.10.1. Misfit analysis

Assessing the solution space of the effective elastic modulus, and the detachment friction in the numerical simulations of the experimental stage preceding fault development reveals that most of the tested parameter combinations produce numerical backwall force that exceeds the physical backwall force, yielding positive force misfit (Fig. 3.17). With increasing sandpack stiffness, the detachment friction that minimizes backwall force misfit decreases (Fig. 3.17A-B). With equal displacement of the backwall, stiffer wedges increase the normal compressive force on the backwall. Models with weaker detachment friction produce longer slip patches along the detachments, which reduces the normal compression on the numerical backwall.

The observed detachment length further constrains the parameters used in the numerical simulations (Fig. 3.17C-D). Increasing the friction provides more resistance to slip, and the active detachment length decreases. As elastic modulus increases, the length of the active detachment increases because the greater stiffness of the wedge promotes slip along the detachment. In infinitely stiff wedges, for example, detachment slip accommodates all of the displacement applied to the backwall. In wedges with non-infinite elastic moduli, off-fault deformation as well as detachment slip can accommodate the applied displacement.

Superposing the regions of parameter space that produce both normal force on the backwall and active detachment length constrains the numerical parameters that enable robust simulation of the physical experiments (Fig. 3.18A-B). Overlapping the successful parameter space regions of both suites of simulations highlights the parameter combinations that enable the agreement of the physical and numerical properties for both simulation suites (Fig. 3.18C). We expect that the effective elastic modulus of the physical experiments including and excluding the glass bead layer should be similar because each wedge is built of sand. Consequently, we select the detachment friction from the parameter combinations with constant elastic modulus. The specified constant elastic modulus is the average of the minimum and maximum moduli of the parameter combinations that produce agreement in the physical and numerical properties in both simulations. At this constant elastic modulus (0.615 MPa), the detachment friction for the simulations of the experiments including (μ=0.098) and excluding (μ=0.11) the glass bead layer is the average of the admissible minimum and maximum detachment friction of each simulation when E=0.615 MPa.

In the post-faulting step of the misfit analysis, we systematically vary the static and dynamic friction coefficients of the thrust faults. In this step of the analysis, the detachment friction coefficients are set at the values identified in the pre-faulting step because we do not expect the strength of the detachment to change preceding and following thrust faulting. Similarly, we do not expect the elastic modulus of the physical wedges to change significantly following fault development. Consequently, we use the elastic modulus identified in the pre-faulting step as the elastic modulus used in the post-faulting step.

In the post-faulting step of the misfit analysis, the backwall normal force is more sensitive to the dynamic friction of the thrust faults, μ_d, than the static friction, μ_s, because most of the thrust faults slip beyond the slip-weakening distance (Fig. 3.19). The sharp drop in the boundary between models with backwall normal force that exceed the admissible range (red) and models with backwall normal force within the admissible range (white and blue) from μ_s=0.6 to 0.7, indicate that smaller portions of thrust fault length achieve the slip-weakening distance when μ_s>0.6. The reduced slip and resulting higher effective strength of the thrust faults cause the backwall normal force to remain elevated. Whereas at lower strengths (lower μ_s and μ_d), the greater slip on the thrusts leads to a greater reduction in the backwall normal force.

Assessment of the parameter spaces in which the numerical and physical backwall force closely match in the simulations excluding and including the glass bead layer reveal the combinations of thrust static and dynamic frictions that minimize backwall force misfit for both suites of simulations (Fig. 3.19). In the physical experiments excluding the glass bead layer, the thrust faults form completely within dry sand. In the experiments including the glass bead layer, the frictional strength of the dry sand likely dominates the total frictional strength of the thrusts because only a small portion of the thrusts (<0.2 cm) intersects the glass beads. Laboratory measurements indicate that the static friction of faults formed within dry sand range from 0.50-0.58 [*Lohrmann et al*., 2003], to 0.48-0.57 [*Klinkmuller et al*., 2016]. When the thrust static and dynamic friction are 0.5 and 0.1, respectively, the numerical and physical backwall force closely match for both suites of simulations. Table 3.1 lists the resulting elastic moduli and friction coefficients of the detachment and thrust faults for the simulations.

3.10.2. Work budget analysis

To investigate the impact of fault development on deformational processes, we constrain the components of the energy budget in numerical simulations of stages of the physical experiments. To assess the sensitivity of the work budget to varying detachment frictional properties, we compare the evolving work budget of numerical simulations representing a cross section of the along-strike center of the experiments that include or exclude the glass bead layer. To assess the sensitivity of the work budget to differing fault geometries, and potential differences between the work done within the center of the physical wedge and on the sides of the wedge, we calculate the work budgets of numerical simulations representing the center of the sandpack, and both sides of the sandpack observed through the glass sidewalls. We compare differences in the incremental work budget components of the physical and numerical accretionary wedges.

3.10.2.1. Work budget preceding and following faulting

In the numerical simulations, the total external work, W_{ext}, is dominated by internal work, W_{int}, while frictional, W_{fric}, and gravitational, W_{grav}, work comprise smaller portions of the total work budget (Fig. 3.20). The development of the thrust fault pair increases W_{grav} and W_{fric}, and decreases W_{int} and W_{ext}. Preceding faulting, W_{int}, W_{fric} and W_{grav} comprise 80-81%, 17-18%, and 2.3-2.4% of W_{ext}. Following faulting, W_{int}, W_{fric} and W_{grav} comprise 73-74%, 23-25%, and 2.7-2.8% of W_{ext}.

The evolution of the work budget in the numerical wedges allows exploration of the sensitivity of each work budget component to varying detachment fault properties. The

misfit analysis indicates that the detachment friction used in the simulations representing the experiment excluding the glass bead layer (0.11) is higher than the detachment friction used in the simulations representing the experiment including the glass bead layer (0.098). In the remaining text, we refer to the simulations of the experiments excluding the glass bead layer as the stronger detachment simulations, and the simulations of the experiments including the glass bead layer as the weaker detachment simulations. We refer to the simulations representing the snapshots of the physical experiment preceding and following faulting as the pre-faulting and post-faulting stages, respectively.

The work budgets of the numerical simulations (Fig. 3.20) illuminate differences in energy partitioning arising from the varying detachment frictions identified in the misfit analysis. Compared to the stronger detachment simulations, the weaker detachment simulations produce less W_{grav}, W_{fric}, W_{int} and W_{ext} preceding and following faulting. The lower external work suggests that weaker detachments provide more efficient fault systems than stronger detachments.

Preceding and following thrust development, the detachment friction should produce negligible changes in W_{grav} because in the numerical models, limited uplift occurs in the pre-faulting stage, and detachment friction should not significantly influence uplift in the post-faulting stage. Preceding faulting, the stronger detachment simulations produce only ~0.05 mJ more W_{grav} than the weaker detachment simulation, or ~4% of the strong detachment simulations W_{grav}.

The stronger detachment simulations produce more W_{fric} than the weaker detachment simulations preceding and following faulting. An increase in detachment strength, as parameterized with a 0.012 increase in friction, is sufficient to increase W_{fric} by 0.79 mJ,

which is 9.2% of the W_{fric} of the weaker detachment simulation. Although increases in frictional strength can inhibit slip, and thus reduce W_{fric}, the increase in 0.012 of the detachment friction increases W_{fric} because the length of the slipping portion of the detachment is similar in the strong and weak detachment simulations. The comparable lengths of slipping portions of the detachments, and higher frictional strength of the detachment in the stronger detachment simulations leads to greater work expended against frictional slip.

Similarly, W_{int} is sensitive to the decrease in detachment friction (Fig. 3.20). Internal work is lower in the weaker detachment simulations because the detachment provides less resistance to the applied normal displacement, producing lower normal force on the backwall. The weaker detachment simulations produce less W_{ext} because less force is required to displace the backwall of the weaker detachment simulations compared to the stronger detachment model. This result is consistent with the physical force measurements, which show that the experiments including the glass bead layer have lower peak force at the first force drop than the experiments excluding the glass bead layer (Fig. 3.7A). In addition, the elevated W_{grav}, W_{fric} and W_{int} produced in the stronger detachment simulations compared to the weaker detachment simulations cause the total W_{ext} of the stronger detachment simulations to exceed the W_{ext} of the weaker detachment simulations in the pre-faulting stage (Fig. 3.20).

3.10.2.2. Sensitivity of work budget to along-strike fault geometry

The evolution of the work budget components in the numerical wedges provides insight into changes in the work budget that occur along strike within the physical

sandpack. In the physical experiments, we must calculate the incremental gravitational, frictional and internal work using the incremental displacement fields of the sandpack sides because we cannot take pictures of the center of the physical sandpack as it evolves. To assess potential differences in the physical work budget along-strike within the wedge, we constrain work budget components in numerical simulations that represent both sides of the sandpack viewed through the glass sidewalls, and a cross section of the interpreted faults at the center of the experiments. Because the sides of the sandpack comprise a small fraction of the total volume of the physical accretionary wedge, considering differences between the work budget estimates of the sides of the physical experiment and the center of the experiments enhances our understanding how fault development impacts system efficiency throughout the volume of the physical experiment.

The work budget components of the models of the center and sides of each experiment differ from each other in the post-faulting stages because the thrust fault geometry differs between the three models of the sides and center of the each experiment (Fig. 3.20). In the post-faulting stage of experiment E375, the position of the thrust root observed through one sidewall differs from the position observed through the other sidewall by ~7 mm (Fig. 3.21), whereas the position of the thrust root differs by <1 mm between the opposing sides of the other experiments. This difference in thrust position produces greater variations between the work budget components of the simulations of the opposing sides of experiment E375 than those differences in the fault geometries of the side and center simulations of the other experiments. The thrust faults observed on the right side of experiment E375 have shallower dips than the thrust faults observed on the

left, or interpreted for the center of the experiment (Fig. 3.21). The shallower dips of the thrusts inhibits uplift between the thrust fault pair, which suppresses the increase in W_{grav} that occurs after thrust fault development. In addition, the shallower dips decrease the slip along the thrusts, which decreases the gain in W_{fric} due to thrust fault development.

The incremental displacement fields of the top of the physical sandpacks indicate that the distance between the intersection of the backthrust and forethrust with the sandpack topography increases toward the sidewalls (Fig. 3.15). The increasing distance between the thrusts suggests that the thrust dips shallow toward the sidewalls for all of the experiments. Consequently, the physical gravitational and frictional work calculated from the side view displacement fields may underestimate the work done within the center of the wedge because the uplift and fault slip may be higher in the center of the wedge.

3.10.3. Comparison of numerical and physical work budgets

To assess the ability of the numerical simulations to capture the energy partitioning and accretion deformation of the physical experiments, we compare the work budget components of increments of the physical experiment to the components calculated in the numerical simulations representing those stages (Fig. 3.22). The misfit analysis ensures that the force exerted on the backwall in the numerical simulations will closely match the backwall force measured in the physical experiments, and that the length of the slipping portion of the detachment in the numerical simulations will match the physical observations preceding faulting. The agreement of the physical and numerical backwall force reduces differences in the physical and numerical external work. The agreement of

the detachment length preceding thrust faulting reduces differences in the physical and numerical frictional work preceding thrust faulting.

The uncertainties in the physical work components due to differences in successive displacement fields are generally larger than the uncertainties in the numerical work components calculated in simulations representing the sides and center of each experiment. Except for the W_{fric} of the post-faulting simulation of experiment E375, the height of the error bar showing the difference between the work calculated for the side and center simulations is insignificant relative to the height of the error bar indicating the variation in the physical work budget components (Fig. 3.22). This relationship indicates that difference between the physical work done on the side of the wedge and the work done within the center of the wedge is small relative to the differences in the work calculated on the sides of the wedge in successive DIC increments.

If the differences between the numerical work budget components calculated in the side and center simulations were significant relative to the uncertainties of the physical work components, comparing the physical and numerical work components would involve an additional layer of complexity. In particular, the most appropriate comparison of the numerical and physical external work should consider the work done in the center sandpack simulations, rather than the side models, because we calculate the physical external work using the normal force on the backwall, which averages the force across the width of the sandpack. Similarly, the most robust comparison of the physical and numerical gravitational, frictional and internal work components should use the work components calculated for the side models because we calculate these components in the physical experiments using the incremental displacement fields of the sandpack sides.

However, for these experiments, the differences between the numerical work components calculated for the side and center simulations are small relative to the differences in physical work components calculated in successive increments. Consequently, we do not distinguish between the numerical work components calculated for the side and center simulations when comparing them to the physical work components.

The evolutions of the work budget components from the stages preceding and following faulting are similar in the physical and numerical wedges: thrust fault development increases work done in uplift against gravity, increases work expended in frictional slip, and decreases the total external work done on the wedge. Preceding and following fault development, estimates of the numerical W_{grav} closely match the range of the physical W_{grav} for each experiment, differing by ~25% of the mean physical W_{grav}.

Preceding faulting, the numerical W_{fric} estimates exceed the physical estimates by <1 mJ (~20% of the mean numerical W_{fric}), with the W_{fric} estimates of the weaker detachment simulations more closely approaching the physical estimates than the stronger detachment simulations. Following faulting, the estimates of the numerical and physical W_{fric} overlap for each experiment. The physical W_{fric} reaches its maximum values after the pre-faulting stage and before the post-faulting stage, nearly coincident with the peak in force on the backwall. The maximum physical W_{fric} overlaps the pre-faulting and post-faulting numerical W_{fric}. The agreement of the physical and numerical W_{fric} following thrust fault development indicates that fault slip in the numerical simulations (Fig. 3.21) robustly captures fault slip in the physical experiments after the thrust faults form (Fig. 3.10). Although the misfit analysis does not examine slip partitioning between the thrust faults, the tuning of the model parameters with backwall force and detachment slip extent

resulted in the appropriate magnitude and distribution of slip between the thrust faults, promoting the agreement of W_{fric} in the post-faulting stages. In particular, the incremental curl rate fields of the physical experiments indicate higher slip along the forethrust compared to the backthrust (Fig. 3.10). In the numerical simulations, the total slip along the forethrust is consistently greater than the slip along the backthrust (Fig. 3.21). The similar partitioning of slip between the backthrust and forethrust in the numerical and physical experiments contributes to the agreement of the physical and numerical W_{fric} after the thrust faults develop.

The physical and numerical estimates of W_{ext} closely match because the misfit analysis identified the combination of parameters that allow the numerical backwall force to be within estimates of the physical backwall force of the experiments with the opposing apparatus configurations. If the force exerted on the numerical backwall exactly matches the force exerted on the physical backwall at a stage of an experiment, then the physical W_{ext} should equal the numerical W_{ext}. There are slight differences in the physical and numerical W_{ext} estimates in the experiments of simulations including and excluding the glass bead layer because the misfit analysis searches for the parameter combinations that allow the numerical backwall force to match the average of the backwall force of two experiments that include or exclude the glass bead layer.

3.10 Discussion of numerical analysis

Synthesizing quantitative observations from physical experiments and numerical simulations enables a robust analysis of energy partitioning. The incremental displacement fields of the top and sides of the sandpacks and force exerted on the

physical backwall provide critical data that help constrain the elastic moduli of the physical wedges, and the effective stiffness and detachment and thrust fault friction coefficients used in the numerical simulations.

3.10.1. Effective stiffness of numerical accretionary wedges

In an approach similar to the misfit analysis employed here, *Cubas et al*. [2013] use the sequential limit analysis method to constrain the internal friction and sliding friction of the detachment and thrust faults in a physical accretion experiment. These parameters are systematically varied in order to identify the combination of parameters that minimize the misfit in the locations, dips and lifetimes of active thrusts observed in the physical experiment and produced in numerical simulations that employ the sequential approach to limit analysis. This misfit analysis identified a detachment sliding friction (5.6±1º, 0.08-0.11) [*Cubas et al*., 2013], similar to the detachment dynamic frictions found here (0.08, 0.10). In addition, *Cubas et al*. [2013] identified a range of dynamic friction of the forethrust (7.6±3.6º, 0.07-0.19) that overlaps the dynamic friction of the thrust faults identified here (0.1).

In the Fric2D accretion models employed here, the misfit analysis reveals that the difference in the physical and numerical backwall force and detachment length is minimized when the effective elastic modulus is 0.62 MPa. With the implementation of the sequential approach to limit analysis, accretionary wedges are simulated as infinitely rigid, with infinitely high elastic moduli [e.g., *Maillot and Leroy*, 2006]. The close agreement of the derived detachment and thrust fault frictions in the numerical wedges within infinite and 0.62 MPa elastic moduli suggest that over a wide range of applied

elastic moduli, the force exerted on the backwall is a robust metric for determining the appropriate frictional parameters that capture deformation observed in physical experiments.

3.10.2. Frictional strength of detachment fault

Systematically varying the effective elastic modulus, and static and dynamic friction in numerical accretion simulations reveals that the dynamic friction of the thrust faults controls the normal force exerted on the modeled backwall. The dynamic friction of the thrust faults has greater influence on the backwall normal force than the static friction because most of faults slip beyond the prescribed slip-weakening distance in the numerical model.

The low detachment friction revealed in the misfit analysis (~0.1) is consistent with the estimates of the detachment frictional strength from physical experiments and field investigations. *Herbert et al.* [2015] found that the work done to propagate the detachment fault is close to zero in physical UCP accretion experiments, suggesting that the effective friction of the detachment fault is close to zero. The low dynamic detachment friction determined in the misfit analysis overlap estimates of the frictional strength of the detachment fault in crustal accretionary wedges [e.g., 0.11-0.25, *Kopf and Brown*, 2003; <0.3, *Ikari and Saffer*, 2011; 0.03-0.19, *Ujiie et al*., 2013; ~0.08, *Fulton et al*., 2013]. While the material and mechanisms producing the low detachment frictional strength in crustal accretionary prisms (i.e., fluid-rich and weakly lithified sediments, fluid fluxes along the detachment) differ from those that produce the low detachment frictional strength in the physical experiments (i.e., polished glass, limited grain

rearrangement near the base), perhaps the similarity in the dynamic frictions of the detachments contribute to the similarity between the evolving fault geometries observed in the physical experiments and inferred in crustal accretionary prisms.

3.10.3. Work budget evolutions

Assessing the tradeoffs of diverse deformation processes within the energy budget framework enables quantification of the impact of fault development on system efficiency. The energy budget of the physical experiments and numerical simulations reveal that accretionary fault development increases W_{fric} and W_{grav}, while decreasing W_{ext}. Thrust development increases fault length, and thus the total slip within the system, increasing W_{fric}. Upward motion between the thrust faults increases uplift, increasing W_{grav}. The numerical work budgets indicate that slip along the faults localizes strain so that less energy is expended in off-fault deformation, reducing W_{int}. In contrast, the physical estimates of incremental W_{int} indicate that off-fault deformation consistently increases throughout the experiment. In the physical experiments, thrust faulting slows the rate of the increase in W_{int} within each experimental increment. Previous analyses of the work budget of other deforming numerical accretionary wedges identified energy budget evolutions in which thrust fault development reduced W_{int} [*Del Castello and Cooke*, 2007; *McBeck et al.*, in rev.].

The numerical estimates of gravitational work closely match the physical estimates (Fig. 3.22), indicating that the numerical simulations produce similar magnitudes and distributions of uplift as the physical uplift observed on the sides of the sandpacks. The agreement of the frictional work done in the numerical simulations and physical

experiments (Fig. 3.22) suggest that the numerical models capture the slip on the faults. The numerical simulations host similar slip distributions along the thrust faults (supp. Fig. 3.6) to those observed in the physical experiments, in which the forethrust has more slip than the backthrust (Fig. 3.10). The agreement in thrust slip partitioning in the physical experiments and numerical simulations suggests that accretionary prisms with weaker detachment faults may favor slip along forethrusts over slip along backthrusts.

Similar to the reduction of the physical incremental W_{int} in the experiments (Fig. 3.8, Fig. 3.11), and the localization of strain as the thrust faults develop (Fig. 3.12, Fig. 3.13), we observe the reduction in off-fault deformation through the shrinkage of high strain energy density (SED) regions following fault development in the numerical simulations (Fig. 3.23). The reduction in median SED value accounts for the decrease in internal work following fault development. In the simulations of the center of experiment E373, preceding thrust fault development, the area of the wedge with high SED is 17 cm^2, and the median SED throughout the wedge is 0.84 Pa. Following fault development, the area of the high SED region shrinks by ~50%, extending only 9 cm^2, and the median SED falls by ~60%, reaching only 0.19 Pa. The force drop that accompanies the development of the first thrust pair in these physical experiments (Fig. 3.7), as well as other experiments [e.g., *Herbert et al.*, 2015], similarly indicates that fault development shrinks regions of high SED in physical accretionary wedges, reducing the internal work. The evolution of physical W_{int} (Fig. 3.8), additionally suggests that fault development reduces the rate of increase in work expended in off-fault deformation. This reduction in internal work increases the efficiency of the system as pervasive internal strain localizes onto discrete thrusts.

The evolution of the normal and shear components of the integrated strain tensor outside of the fault zones in the physical wedges (Fig. 3.11) highlights that preceding discrete thrust fault development, enhanced horizontal contraction and vertical thickening permeate the wedge, increasing the total W_{int} (Fig. 3.8; supp. Fig. 3.5). Snapshots of the complete field of each incremental strain tensor component as the thrusts develop (Fig. 3.13) reveal that this increase in strain develops in the region where the thrusts eventually form. In crustal accretionary wedges, regions of elevated compaction and/or layer-parallel shortening at the toe of accretionary wedges may indicate the future development of a new frontal accretionary thrusts.

The partitioning of energy revealed in these work budgets suggests that in accretionary tectonic settings fault development increases W_{fric} and W_{grav}, and decreases W_{int} and W_{ext}. Estimates of crustal stress from borehole breakouts [e.g., *Zoback and Healy*, 1992] and plate motions from GPS [e.g., *Mazzotti et al.*, 2001] constrain the external work done on crustal accretionary prisms. Uplift calculated from vertical GPS [e.g., *Ching et al*., 2011] and InSAR [e.g., *Schmidt and Burgmann*, 2003] constrain the work of uplift against gravity. Evidence of increasing temperature along faults during frictional slip, such as silica gel [e.g., *Kirkpatrick et al*., 2013] and pseudotachylyte [e.g., *Sibson and Toy*, 2006], indicates the magnitude of energy expended in slip against friction. Each of these components of the energy budget evolve as layer-parallel shortening amplifies pervasive internal strain, new accretion faults propagate, out-of-sequence faults cut older faults, and pre-existing faults are reactivated, perhaps slipping coseismically.

3.11. Conclusions of numerical analysis

This study compares the energetic tradeoffs of frictional slip, uplift and distributed off-fault deformation in physical accretion experiments, and in numerical simulations in order to shed insight on the transition from internal deformation to localized slip on accretionary thrust faults. Constraining the evolving physical and numerical energy budgets reveals that thrust fault development increases the overall system efficiency, as the work expended in frictional slip and uplift against gravity increases. The numerical work budgets indicate that decreasing off-fault deformation drives the increase in efficiency, whereas the physical estimates of internal work continually increase throughout the development of the first thrust pair. The application of this energy budget approach to crustal tectonic environments will help determine if energy partitioning in crustal environments is similar to the partitioning within physical and numerical accretion experiments. Applying the energy budget framework through the synthesis of field interpretations, the kinematics and external force measured in physical experiments, and the complete stress field provided by numerical simulations will enhance our understanding of the interaction of diverse deformation mechanisms operating in tectonic environments.

3.12. Figures

Figure 3.1

Physical experiment set up. A) Views of top and sides of sandpack reveal timing and geometry of fault development. B) Physical force measured on the backwall reveals strain hardening and softening associated with distributed compaction of the sand and thrust fault development. Comparing variations in force with the fault geometry observed in the side and top views allows a detailed understanding of the impact of fault development on the normal force exerted on the backwall, and thus the overall system efficiency.

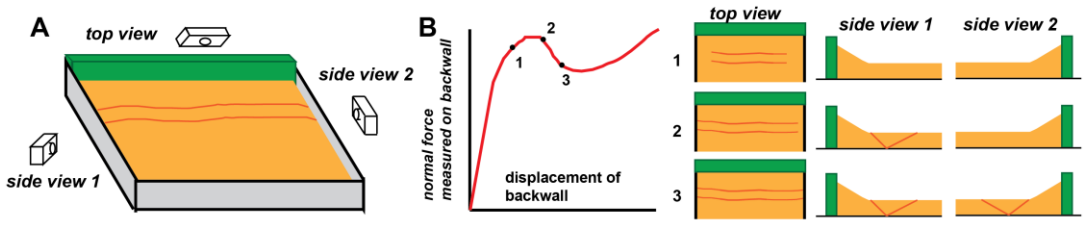

Figure 3.2

Views of fault development. Incremental displacement fields of top and side views of experiment E374 throughout the development of the first thrust pair, at 0.5 mm increments of applied backwall displacement. Preceding thrust fault development (A), the incremental strain field remains diffuse: the displacements gradually decrease from the backwall toward the opposite wall. B) When sharp gradients in the top view displacement field reveal the development of the first thrust pair, the side view displacement fields do not yet host sharp gradients indicative of localized slip, but show only diffuse zones of shear. C-E) With continued backwall displacement, the gradients in the top and side displacement fields progressively sharpen as faults begin to localize. In the top view displacement field, the thrusts begin to localize within the center of the sandpack, and then extend toward the sidewalls. In the side view displacement fields of this experiment, fault localization begins earlier on the right side than the left side (C), causing the forethrust to remain more diffuse on the left side view than the right side view in the last increment shown here (E).

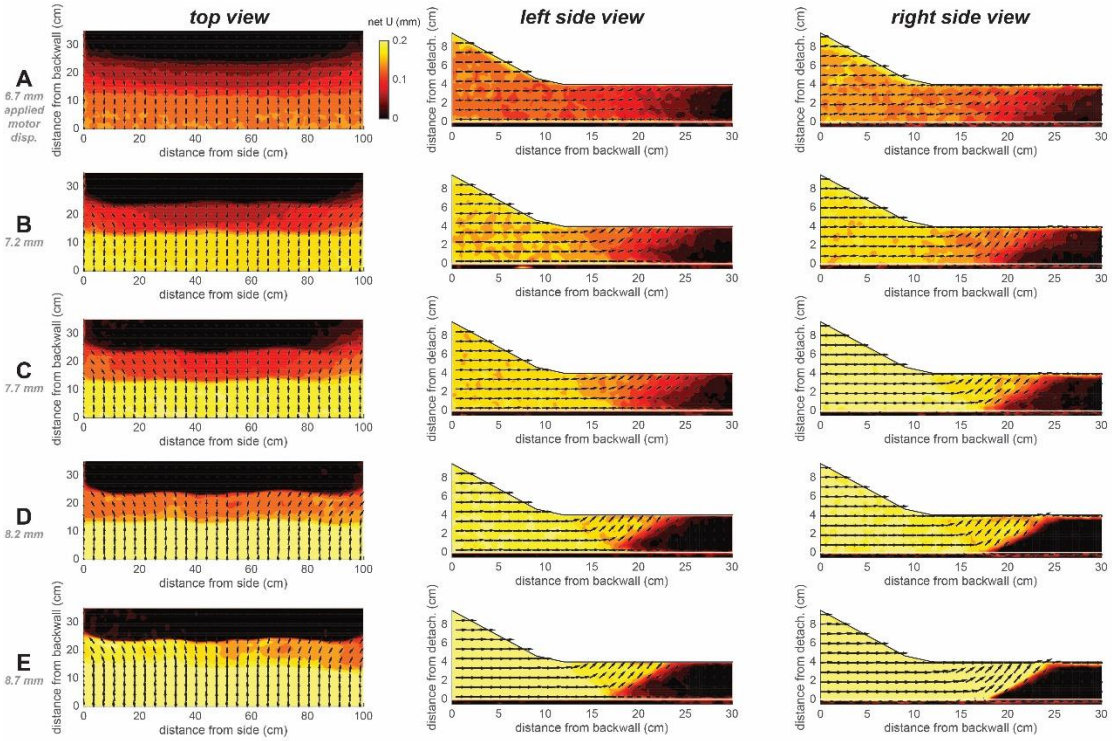

Figure 3.3

Experiment apparatus configurations. Experiments differ in apparatus configuration (moving base or backwall) and inclusion of glass bead layer. The different apparatus configurations should not influence the calculated work budget components. However, the inclusion or exclusion of the glass bead layer is expected to produce differences. Experiments E373 and E375 lack a glass bead layer. Experiments E374 and E376 include a glass bead layer. Experiment E373 and E374 (A) have moving bases. Experiment E375 and E376 have moving backwalls.

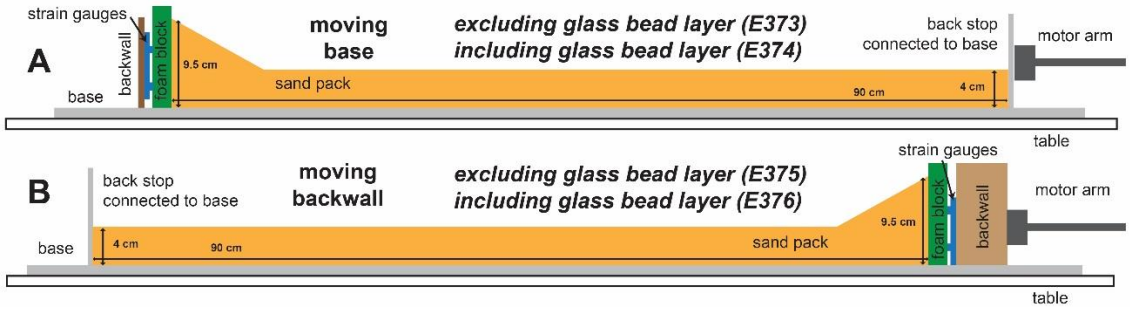

Figure 3.4

Measurement of physical backwall force. A) Configuration of uniaxial strain sensors on four plaques, which are fixed to a rigid board that is adjacent to the backwall in the experiments. Each plaque contains four uniaxial strain sensors (white rectangles) that are fixed to metal arms mounted on the plaque. B) Calibration of strain gauges to known weights results in a linear relationship of machine strain units to weight (R^2=0.99).

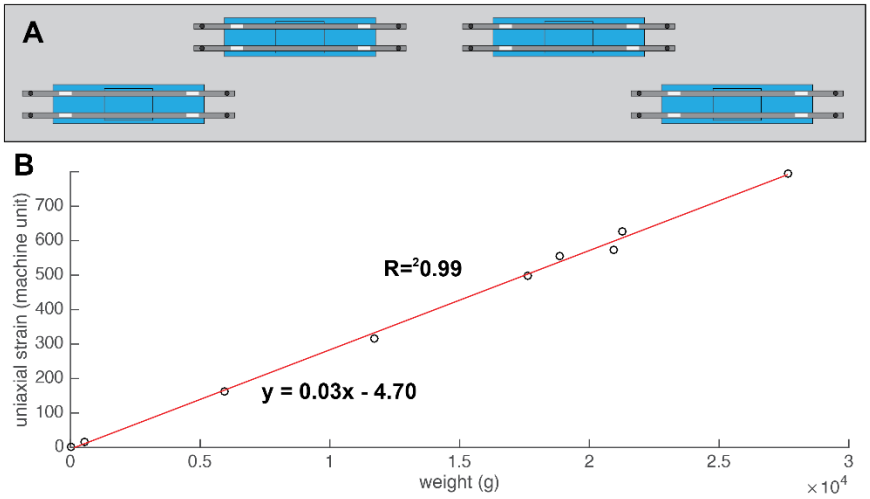

Figure 3.5

Kinematic compatibility assessment. We use kinematic compatibility to assess the relative robustness of the incremental displacement fields for experiment E373 (red), E374 (dark blue), E375 (pink) and E76 (light blue). From each kinematic compatibility field, we identify the mean plus one standard deviation, K^F, in order to define a representative value of K for the field. High values of K imply movement of material towards or away from the glass side walls, which invalidates 2D plane strain. We find the mean and standard deviation of the K^F of all the displacement fields and remove the fields from the analysis that have K^F above one standard deviation from the mean. Models within the gray region are thus considered reliable. Triangles pointing to the left (black triangle) and right (white triangle) show K^F of displacement fields derived from the left and right sides of the experimental apparatus, respectively. Most of the displacement fields from the right side of experiment E375 are considered unreliable due to inadequate focusing of the associated cameras. Consequently, we exclude the incremental displacement fields calculated for the right side of experiment E375 from the analysis. See supp. Fig. 3.3 for an example of displacement fields from both sides of experiment E375 with high and low K^F.

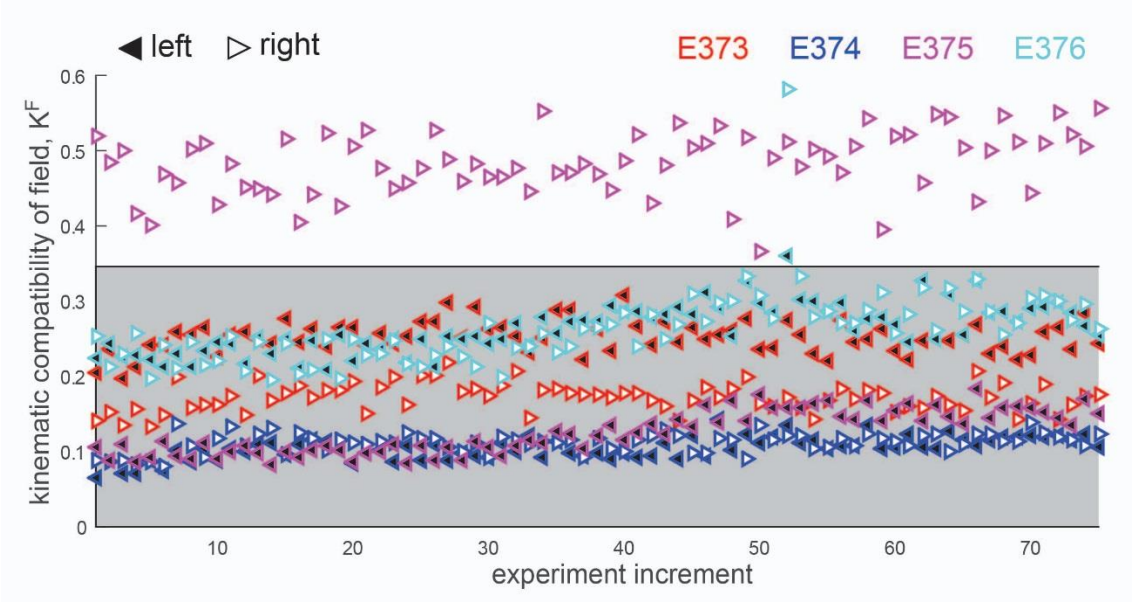

Figure 3.6

Faulting events with backwall force. Complete force curve (A, C, E, G) and faulting observations with physical force evolution (B, D, F, H) for each experiment. Fault development produces drops in force. Gray box in plots on left highlights portion force curve shown in plots on right. Vertical lines on right plots indicate when we first observe evidence of faulting on top (black), left side (dark blue), and right side (light blue) of the sandpack. Triangles indicate local maximum (peak, upward triangle) and local minimum (trough, side triangle) of first force drop. Evidence of fault development is observed in top view of sandpack before the force peak. Force trough occurs after the first evidence of faulting is observed in either side of the experiment.

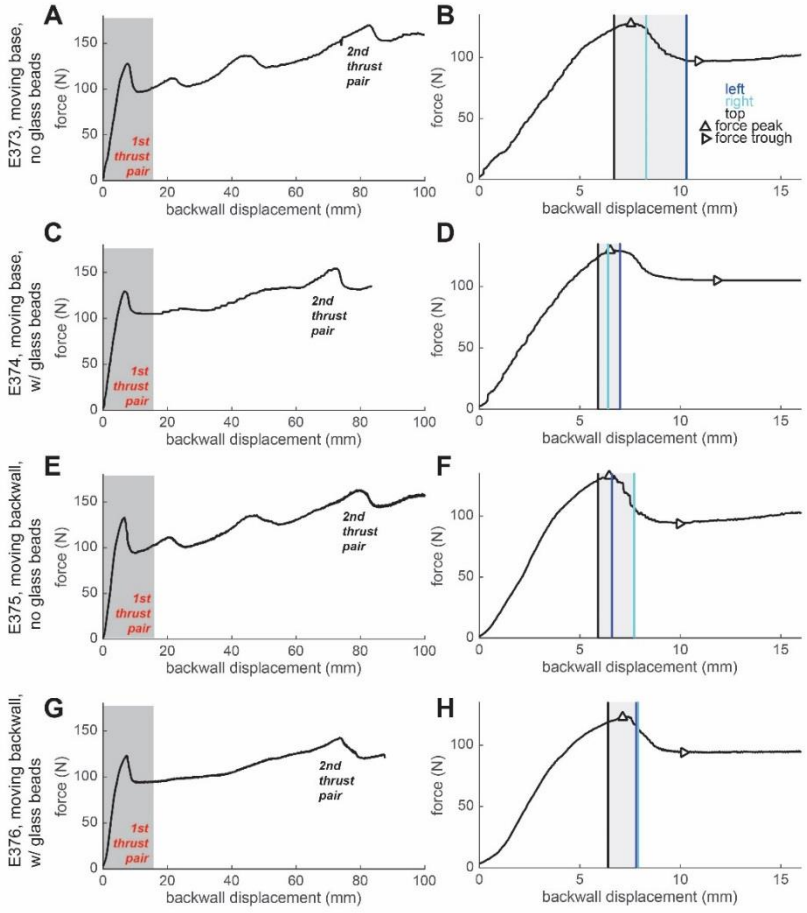

Figure 3.7

Estimates of physical effective elastic moduli of physical wedges. We calculate effective elastic modulus as the tangent to stress-strain curve at 50% of the peak stress. A) Force-displacement relationships for each experiment, from which we calculate stress-strain curves. Black dot shows 50% peak stress. Solid portions of curves indicate part from which we estimate effective elastic modulus. B) Estimates of effective elastic modulus, *E*, for each experiment as a function of the change in cumulative longitudinal strain (ε_{xx}) and change in backwall normal stress (σ_n) at 50% peak stress. Range in ε_{xx} (horizontal error bars) arise from differences in horizontal displacements on opposing sides of each experiment. Range in σ_n (vertical error bars) arise from differences between potential load-bearing heights of sandpack in contact with backwall, from 4 cm to 8 cm. We approximate *E* from the slope of the lines of best fit, $\Delta\sigma_n/\Delta\varepsilon_{xx}$, using σ_n calculated from the minimum load-bearing height for each experiment, the maximum load-bearing height for each experiment, and the preferred height for each experiment (minimum for moving base, and maximum for moving backwall). The line of best fit through the preferred heights (green) has the highest R^2 value, so we consider the slope of this line as the most robust estimate of *E* (0.99 MPa).

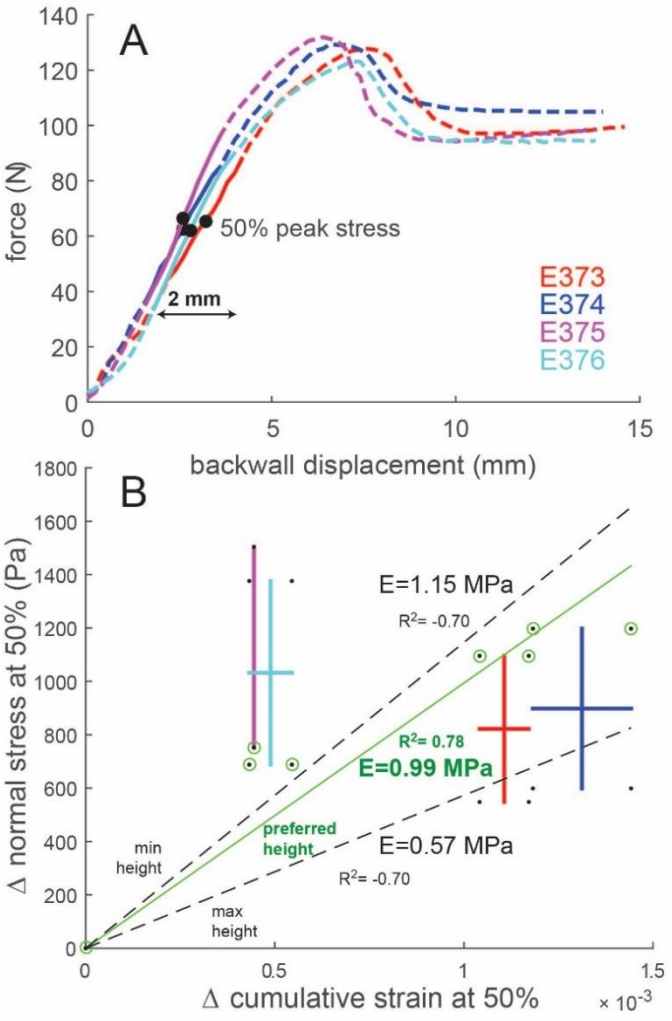

Figure 3.8

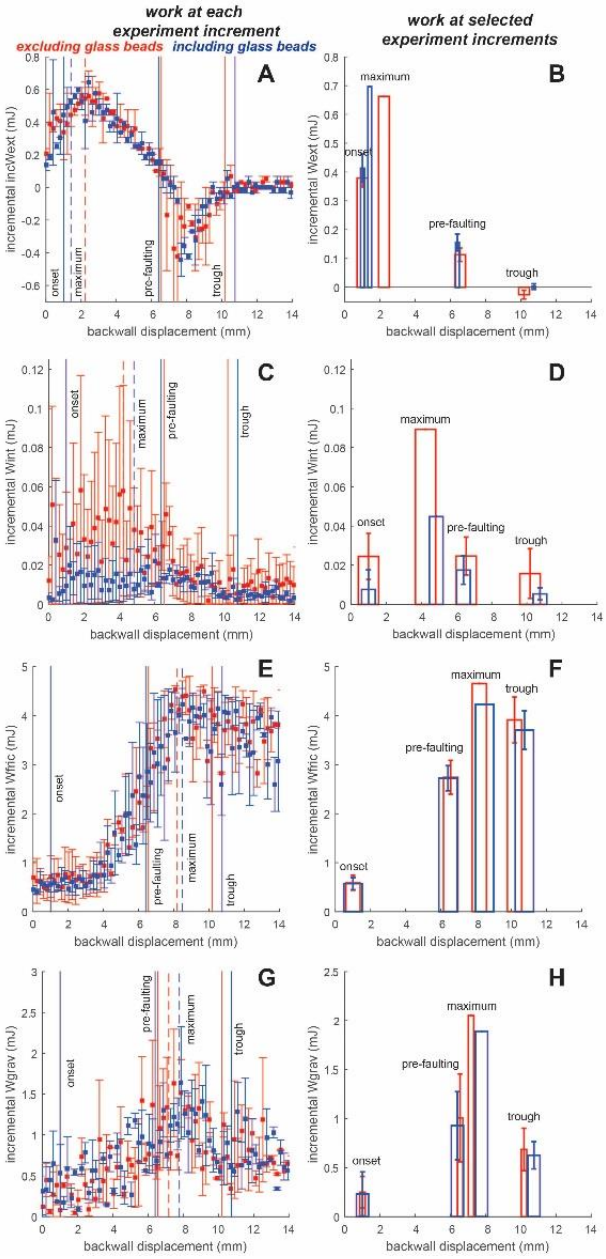

Physical incremental work budget. Work budget of physical experiments: incremental external work, W_{ext} (A-B), incremental internal work, W_{int} (C-D), incremental frictional work, W_{fric} (E-F), and incremental gravitational work, W_{grav} (G-H). First column (A, C, E, F) shows incremental work done at each increment. Second column (B, D, F, H) shows incremental work done at selected increments: at 1 mm of applied backwall displacement (onset), before faults are observed at the top of the sandpack (pre-faulting), at the increment when the work component is maximized (maximum), and at the trough of the force curve (or post-faulting stage). In the first column, the squares show the average work components of experiments with opposing apparatus configurations for experiments excluding (red) and including (blue) glass bead layer. Height of error bars are the difference between the work components calculated for the differing experiment configurations. Supp. Fig. 3.4 shows the incremental work done in each increment of each experiment individually.

Figure 3.9

Physical incremental uplift. Physical vertical displacement, U_Y, fields of moving backwall experiments excluding (A-B) and including (C-D) glass bead layer. Incremental U_Y preceding (A, C) and following (B, D) thrust fault development. Preceding thrust development, a broad pattern of uplift develops in the region where the faults ultimately form. Following thrust fault development, uplift localizes above discrete thrust faults. While the uplift pattern transitions from gradational to sharply bounded by faults, the overall W_{grav} remains similar preceding and following fault development.

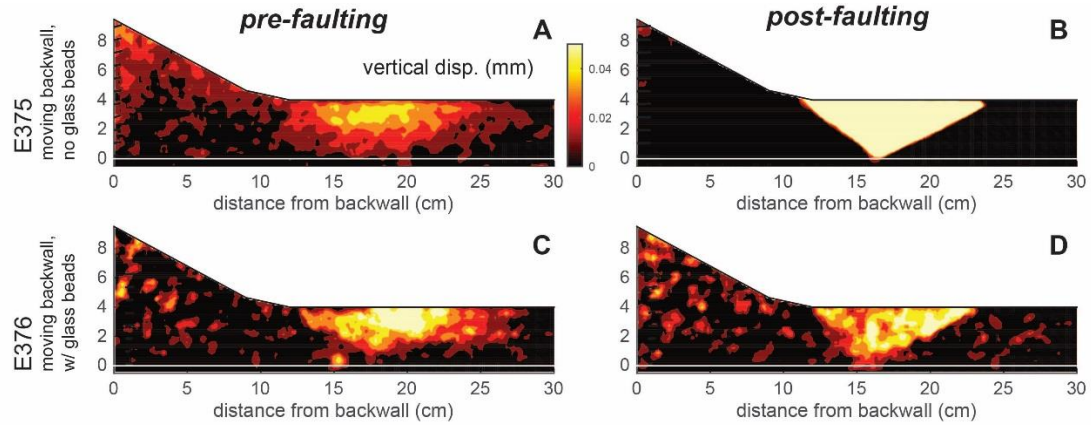

Figure 3.10

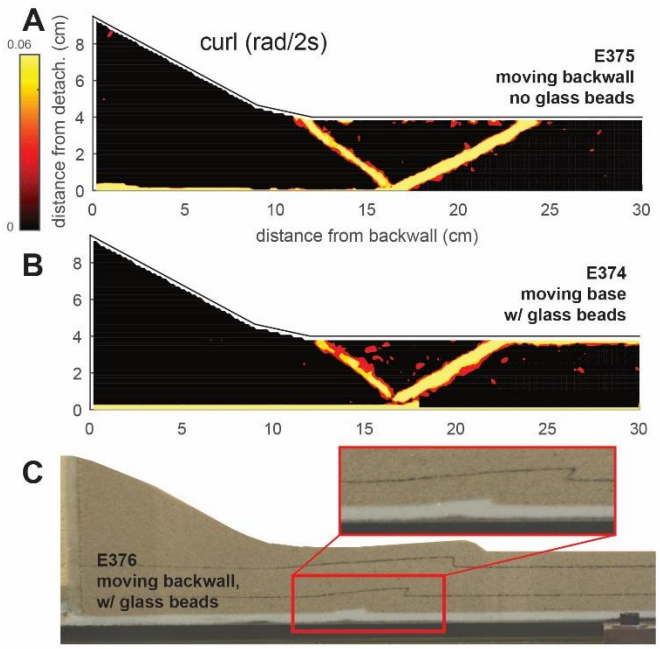

Physical incremental curl. Curl of incremental displacement fields of moving backwall experiment excluding (A) and including (B) glass bead layer following faulting. Curl field reveals that inclusion of glass bead layer suppresses slip on backthrust, reducing ΔW_{fric} associated with fault growth. C) Photo of side of experiment E376 following faulting. The entrainment of glass beads along the forethrust promotes slip on the forethrust and suppresses slip on the backthrust, perhaps by producing a smoother process zone near the base of the forethrust.

Figure 3.11

Evolution of integrated incremental strain tensor outside fault zones. We derive the internal work from the integrated incremental strain tensor components at each experiment increment. Error bars show range in tensor component from opposing sides of apparatus. Preceding faulting, the wedge experiences: A-B) increasing horizontal contraction (negative ε_{xx}), C-D) increasing vertical dilation (positive ε_{yy}), and E-F) relatively constant shear strain (ε_{xy}). These evolutions indicate that increasing normal strains drive the increase in W_{int} immediately preceding thrust fault. The development of the thrust faults reduces the off-fault horizontal contraction (decreasing magnitude of ε_{xx}), and off-fault vertical dilation (decreasing magnitude of ε_{yy}), while shear strain remains constant or decreases.

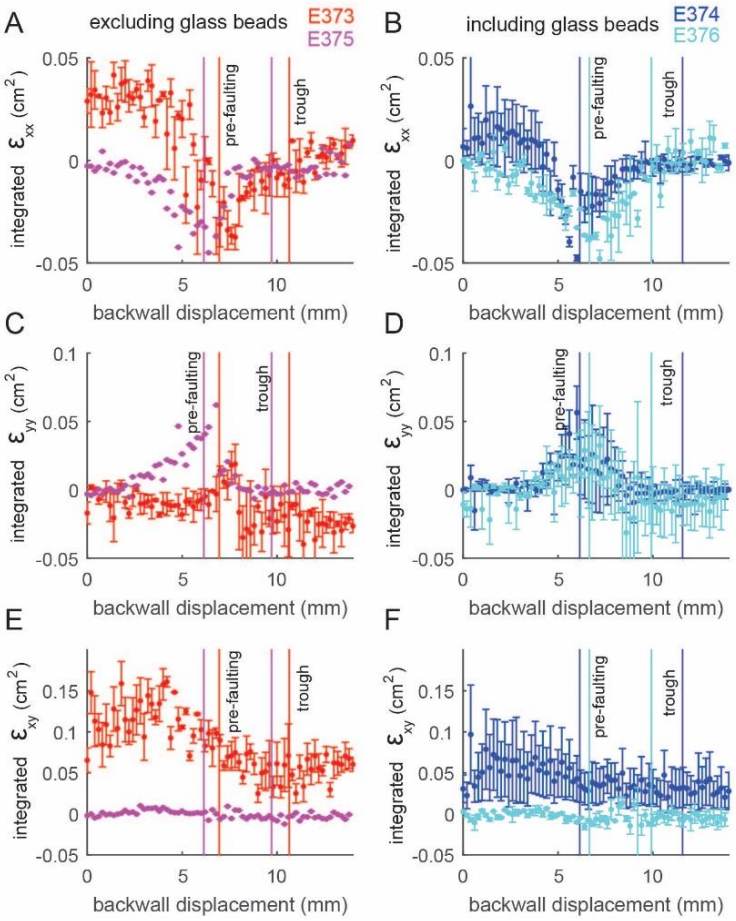

Figure 3.12

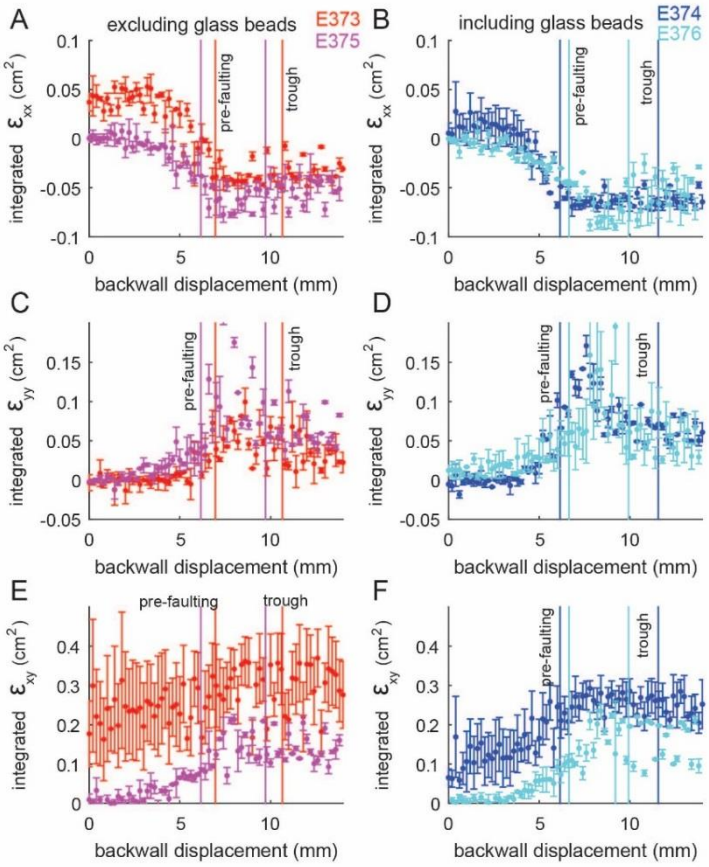

Evolution of integrated strain tensor including the fault zones. Preceding faulting, the wedge experiences: A-B) increasing horizontal contraction (negative ε_{xx}), C-D) increasing vertical extension (positive ε_{yy}), and E-F) increasing shear strain (ε_{xy}). The development of the thrust faults causes the total horizontal contraction and shear strain to plateau. The total vertical dilation increases as the faults develop and then plateaus when the faults are more fully localized.

Figure 3.13

Evolution of strain tensor components for experiment E375. A) Preceding thrust faulting, high normal strains remain dispersed through the wedge, while shear strain is localized along the detachment. B) With continued backwall displacement, horizontal contraction and vertical extension shift toward the region where the thrusts ultimately develop, and the zone of high shear strain surrounding the detachment extends further from the backwall. C) In the incipient stages of thrust development, horizontal contraction and vertical extension concentrate along the incipient thrusts, forming broad bands of high strain a few centimeters thick. At this stage, elevated zones of shear strain highlight slip along the thrust faults, with higher strain along the forethrust. D) As strain continues to localize along the thrusts, the zones of high horizontal contraction and vertical extension decrease in width as shear strain along the forethrust increases and shear strain along the backthrust remains low. Some of the patchy texture of the strain fields arise from spurious noise in the incremental displacement fields.

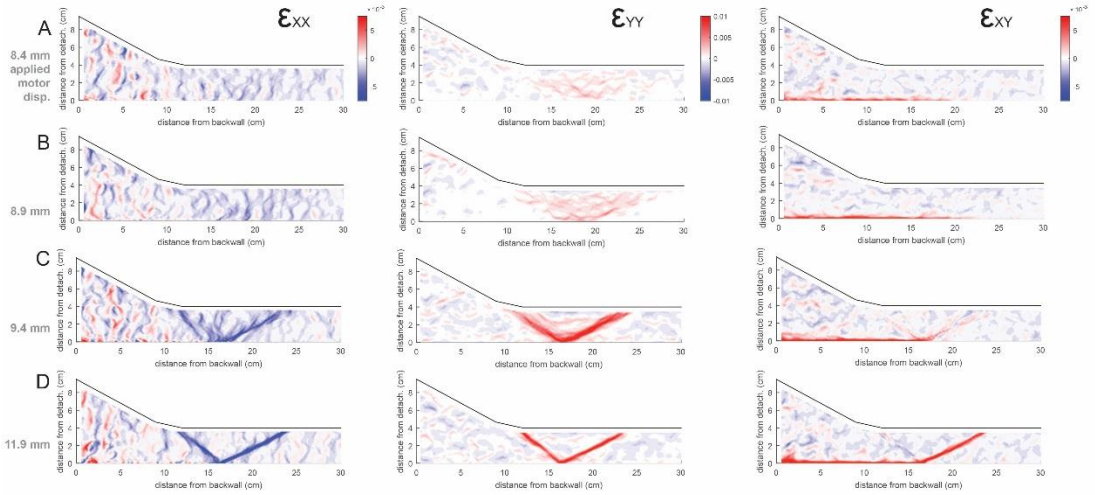

Figure 3.14

Numerical model boundary geometry and loading conditions. Rightward displacement is applied to left vertical boundary (backwall) towards the center of the model to simulate contraction. Right vertical boundary wall is prevented from displacing in the directions normal to the boundary (left or right), and is allowed to displace in directions parallel to the boundary (up or down). The model base remains fixed with no displacements in vertical (normal) or horizontal (shear) directions. Topography of wedge is allowed to deform freely with zero tractions. The numerical simulations contain a horizontal detachment fault 1 cm above the base of the model. The length of the model is 50 cm.

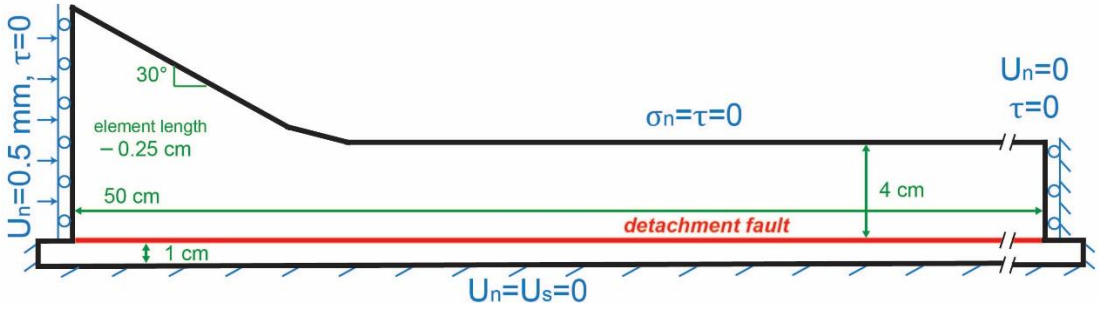

Figure 3.15

Differences in fault geometry along strike. Displacement fields of top of sandpacks reveal changes in fault geometry from the center of sandpack toward the sidewalls. Backthrust and forethrust position identified from top view incremental displacement field (A, C, E, G), and histograms of distance between thrust positions for portions of thrusts within center 20-80 cm (dark gray), and portions of thrusts within 5 cm of side walls (light gray) (B, D, F, H). I) Means and standard deviations of distances between thrusts within the center 20-80 cm (>20 cm, <80 cm) and outside 5 cm (<5 cm, >95 cm) measured in the incremental displacement field of the top of the sandpack, and distance between thrusts measured in the top view displacement fields at the sidewalls (1 & 100 cm). The distance between the thrusts increases from the center toward the sidewalls, suggesting that the thrust dips shallow toward the side walls.

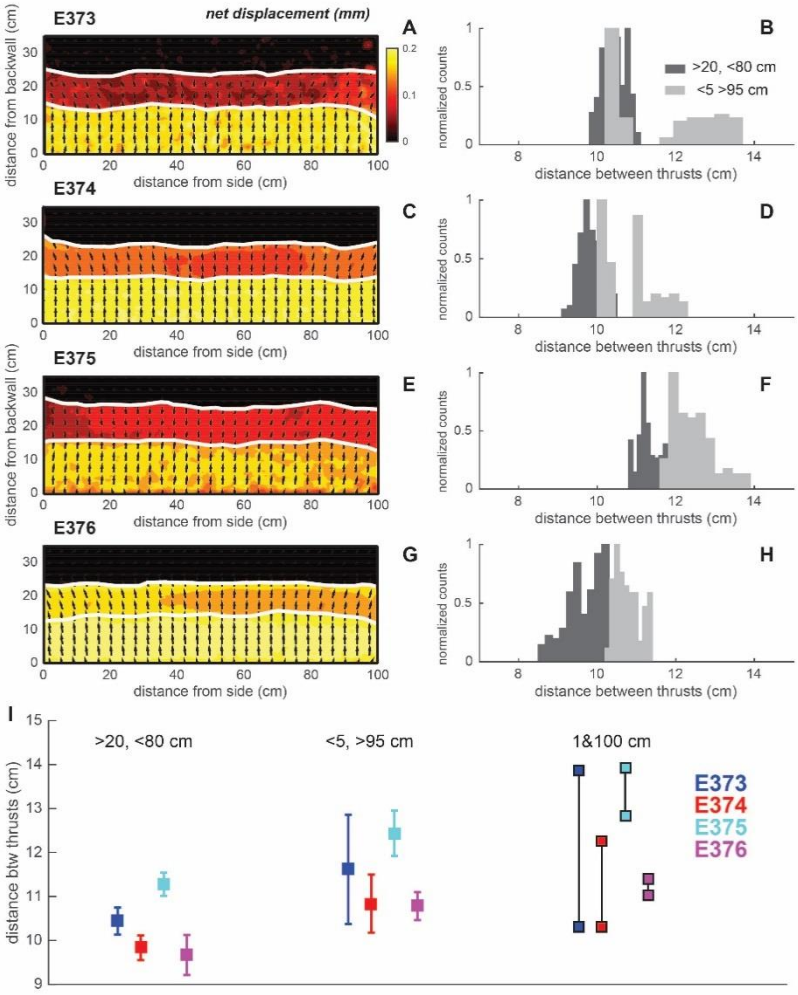

Figure 3.16

Construction of numerical thrust fault geometries. We use dips of thrusts observed in side view displacement fields and positions of thrusts observed in top view displacement fields. Mean thrust geometry observed through sidewalls (blue dashed lines) and mean positions of thrusts within center 20-80 cm (black triangles) for experiments excluding (A) and including (B) glass bead layer. Blue solid lines show the thrust geometries constructed from the mean thrust positions observed on top of sandpack and the mean thrust dips observed on sides of sandpack. The numerical faults, which represent conditions at the center of the experiment, are steepened from the sidewall observations, so that they share a common root (black lines).

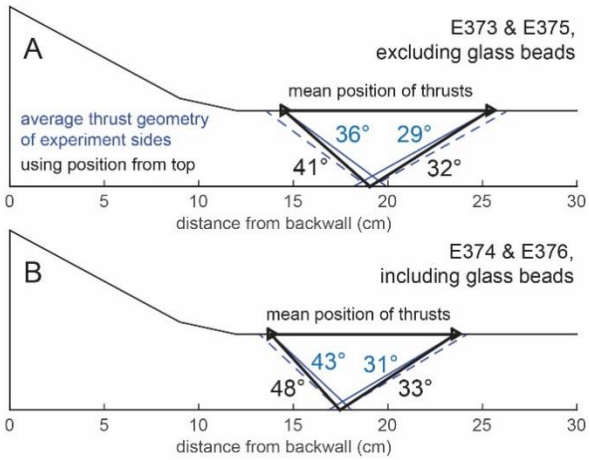

Figure 3.17

Pre-faulting step of misfit analysis. We vary detachment friction, μ, and elastic modulus, E, to reduce the misfit in numerical and physical backwall force (A, B) and misfit in slipping detachment length (C, D), for simulations of experiments excluding (A, C) and including (B, D) glass bead layer. Positive misfit indicates that the numerical results exceeds the physical backwall force or detachment length. Black contour lines indicate parameter combinations that produce numerical results within the range of physical observations. Dots show results from tested numerical simulations. The misfit analysis shows the tradeoffs between model stiffness and detachment friction on the stress and displacement fields resulting from the applied loading. As E increases, detachment μ must decrease in order for the numerical models to match the physical backwall force. In contrast, as E increases, μ must increase for the numerical models to match the observed detachment fault length.

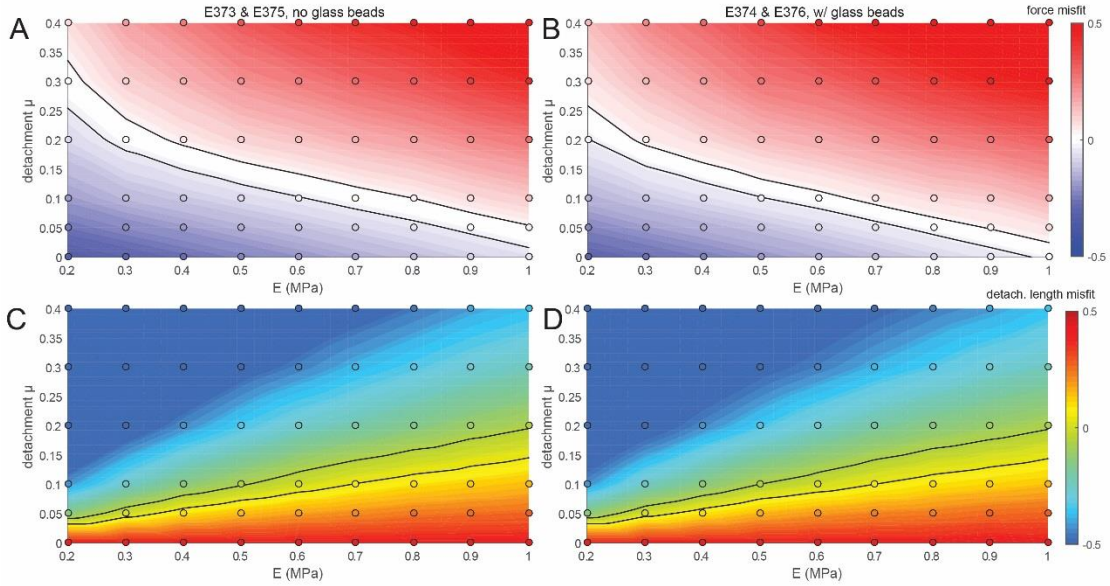

Figure 3.18

Synthesis of pre-faulting misfit step**.** The contrasting response of the detachment friction, μ, to increasing stiffness, E, in the misfit analysis constrains the parameter space that provides consistent material properties for experiments that exclude (A) or include (B) a glass bead layer. Blue and red lines indicate the range of E and detachment μ that produce the measured backwall force and detachment length, respectively. The polygon formed by the intersection of the red and blue contour lines reveal the combination of parameters that can produce numerical detachment length and backwall force that fall within the physical estimates. C) Overlapping the polygons of both simulations highlights the parameter combinations that enable the agreement of the physical and numerical properties for both simulations. We expect that the effective elastic modulus of the physical experiments including and excluding the glass bead layer should be similar because each wedge is built of CV32 sand. Consequently, we select the detachment μ from the parameter combinations with constant E. The specified constant E is the average of the minimum and maximum E from the overlap region of admissible parameter combinations from both simulations. At this constant E (0.615 MPa), the average of the admissible minimum and maximum detachment μ of each simulation provides the detachment μ for the simulations of the experiments including (μ=0.098) and excluding (μ=0.11) the glass bead layer.

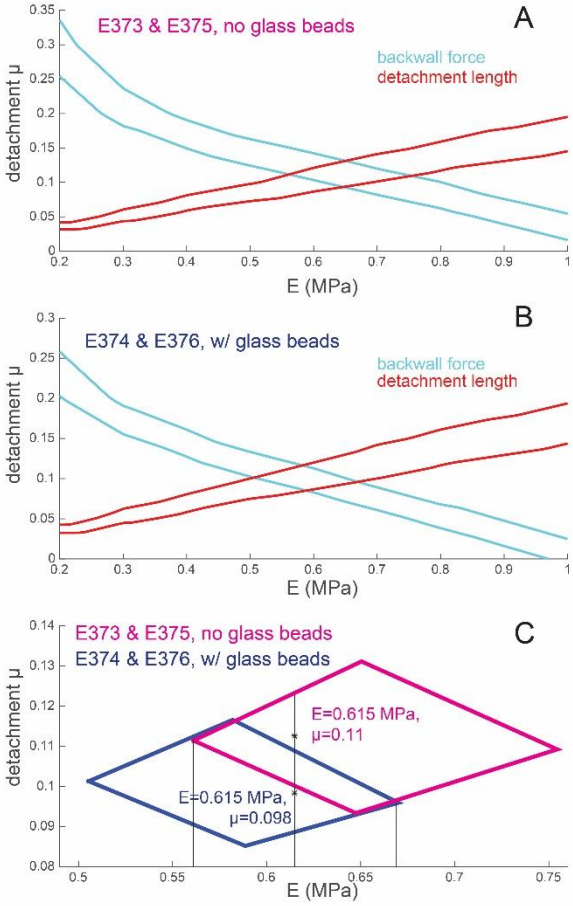

Figure 3.19

Post-faulting step of misfit analysis. We vary the static, μ_s, and dynamic friction, μ_s, along thrust faults within simulations of experiments excluding (A) and including (B) glass bead layer to minimize the misfit in backwall force. The friction of the thrust faults should be similar in all of the experiments regardless of basal glass beads because each wedge is built of the same CV32 sand. We select the static and dynamic friction of the thrust faults from the combination of parameters that enable both simulations to achieve the observed physical backwall force. The misfit analysis is insensitive to the prescribed static thrust friction because most of the fault elements slip beyond the slip weakening distance, so that they deform with dynamic friction. We prescribe μ_s=0.5, following laboratory measurements. The overlapping parameter spaces of the simulations indicate that when μ_d=0.1, the numerical backwall force closely matches the physical backwall force. In summary, the pre-faulting and post-faulting steps of this misfit analysis indicates that the detachment μ of the simulations of the experiments including and excluding the glass bead layer should be 0.098 and 0.11, respectively. For all the simulations, to achieve the desired backwall force and detachment length, E=0.615 MPa, thrust μ_s=0.5, and thrust μ_d=0.1.

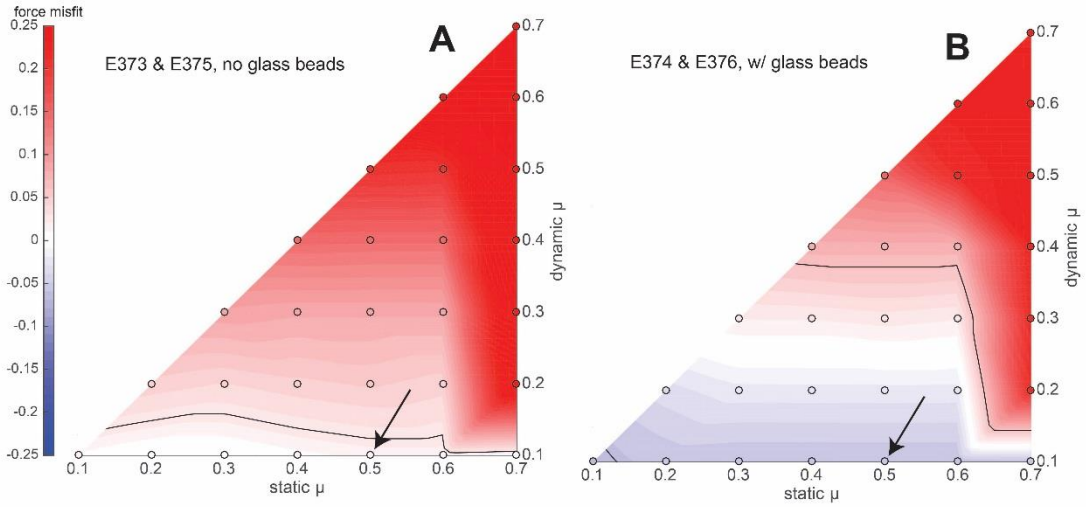

Figure 3.20

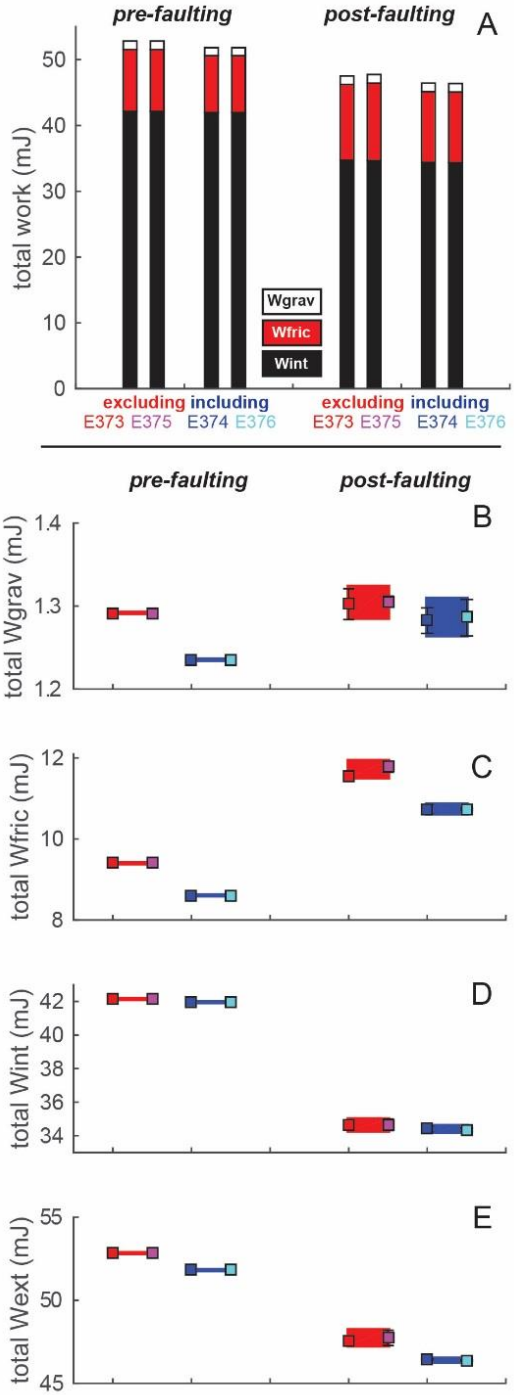

Evolving work budget of numerical simulations. A) Work budget for simulations representing center of each experiment. The total external work, W_{ext}, is dominated by internal work, W_{int}, while frictional, W_{fric}, and gravitational, W_{grav}, work comprise smaller portions of the total budget. B-E) Work budget components for simulations preceding and following faulting. Heights of error bars are the difference between the maximum and minimum work budget components of the simulations of the center, left side, and right side of each experiment. Thrust fault development increases W_{grav} (B) and W_{fric} (C), and decreases W_{int} (D) and W_{ext} (E). Compared to the stronger detachment simulations (excluding the glass bead layer experiments), the weaker detachment simulations (including the glass bead layer experiments) produce less W_{grav}, W_{fric}, W_{int} and W_{ext} preceding and following faulting.

Figure 3.21

Comparison between side and center simulations. Simulations of side views and center of experiment E375 preceding (1st column) and following thrust fault development (2nd-4th columns). A-D) Net displacement field. E-H) Slip on faults. I-L) Strain energy density (SED). The net displacement fields of the post-faulting simulations reveals greater uplift in the left side and center models (B-C) than in the right side model (D) due to the steeper thrust dips in the left and center models. The steeper dips in the left and center models produce greater slip on the thrusts in the left and center models (F-G) than in the right side model (H).

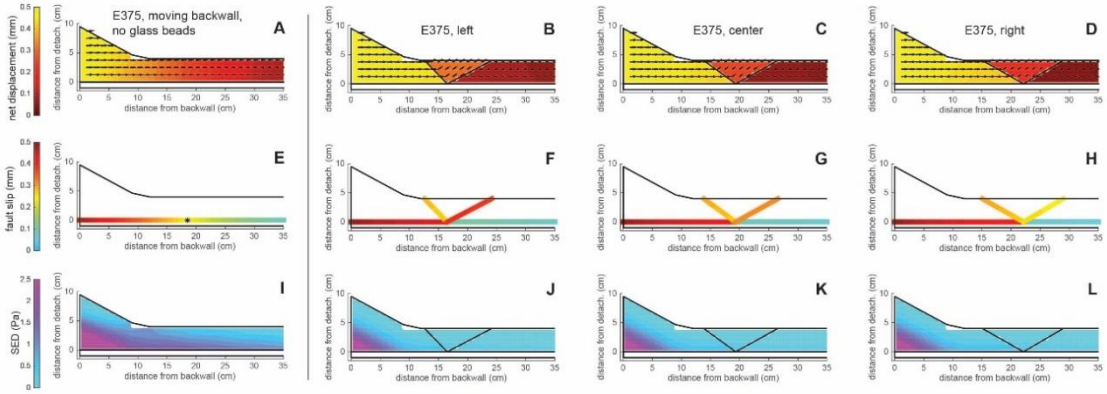

Figure 3.22

Numerical and physical work budget components. Circles show mean of physical work component within 0.5 mm of increments preceding and following faulting, and when work component reaches its maximum value for both experiments that either include or exclude the glass bead layer. Height of error bars are the standard deviation of work components within the associated increments of the experiment. Smaller squares show mean of numerical work components of side and center simulations with heights of error bars representing the range from the minimum to maximum work component. Larger rectangles highlight the range in the calculated physical work budget component for the experiments including or excluding the glass bead layer. The numerical work budget components overlap or closely approach the corresponding physical components for each set of experiments including or excluding the glass bead layer, at both the pre-faulting stage and the force trough.

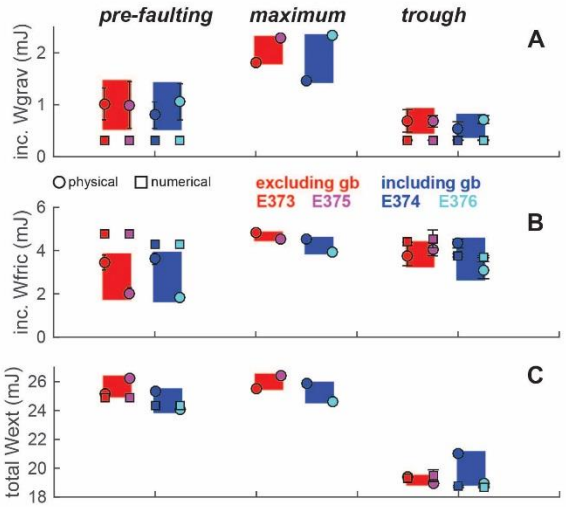

Figure 3.23

Strain energy density (SED) of numerical simulations. Preceding (A) and following (B) thrust fault development for center of experiment E373. Fault development shrinks area of wedge with high SED by 53%, and reduces median SED by 77%.

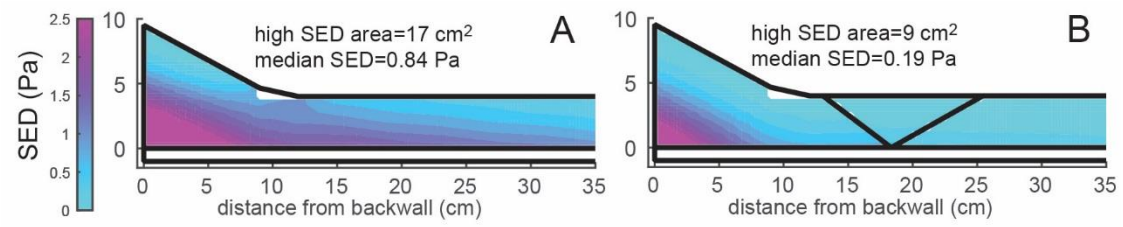

3.13. Tables

Table 3.1

Misfit analysis results. Elastic moduli, E, and coefficients of static, μ_s, and dynamic, μ_d, friction identified in misfit analysis for simulations of experiments excluding (E373, E375) and including (E374, E376) glass bead layer.

	E (MPa)	detachment		thrust	
		μ_s	μ_d	μ_s	μ_d
E373, E375	0.615	0.110	0.110	0.5	0.1
E374, E376	0.615	0.098	0.098	0.5	0.1

3.14. Supplemental information

Supplemental Fig. S.3.1

Physical E estimates using gauge calculation. Estimation of physical effective elastic modulus using stress-strain relationships derived from applied motor displacement and displacement of strain gauge arms. The uncertainty in the displacement of the strain gauge arm with varying loads produces unrealistic stress-strain curves, and associated estimates of effective elastic modulus. A) Set up of strain gauges with respect to applied displacement vectors in the moving base experiment configurations. B) Calibrations of applied stress to strain gauge arm displacement. Each calibration curve is derived from outer limits of each data point measured in calibration. Horizontal bar is derived from the uncertainty in stress measurement, which is taken from the amplitude of noise in the physical force measurements during the experiments. Vertical bar is derived from the uncertainty in the measurement of the strain gauge arm displacement. Correction of applied strain considering the displacement of the strain gauges (C-F) produces overly steepened curves with negative slopes, indicating that the correction of the applied strain results in lower strains than produced in the experiment. Applying a non-linear calibration curve may reduce the over-steepening of the stress-displacement curves. Stress is calculated by assuming that the load-bearing height of the sandpack is 9.5 cm.

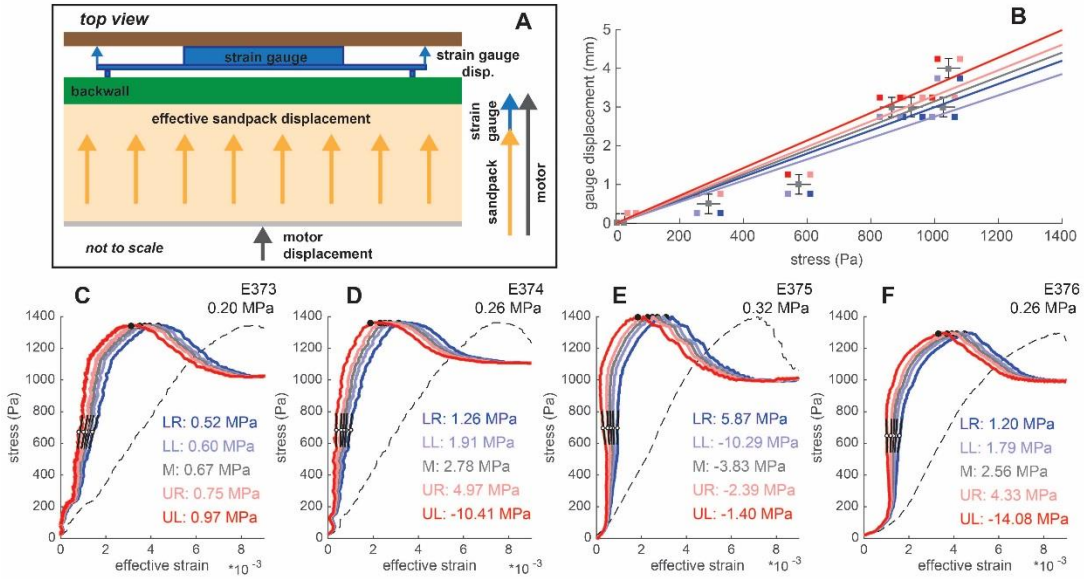

Supplemental Fig. S.3.2

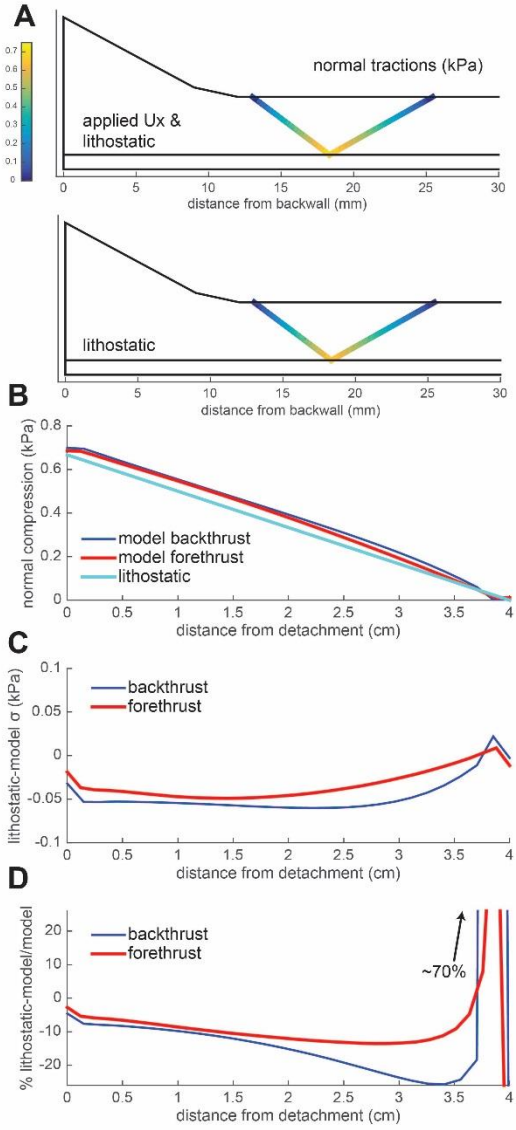

Assessment lithostatic stress and normal tractions. A) Normal tractions on thrust faults in numerical models with applied horizontal displacement of backwall, U_x (upper), and normal tractions arising from only lithostatic stresses (lower). B) Normal tractions on modeled faults due to lithostatic stresses and due to U_x and lithostatic stresses as a function of depth. C) Difference in normal tractions on faults arising from only lithostatic stress and from U_x and lithostatic stress. From the base of the wedge to 3.5 cm from the detachment, the lithostatic tractions underestimate the model tractions by <0.05 kPa. This difference is 5-25% of the lithostatic+U_x estimate (D) up to 3.5 cm from the detachment. Toward the top of the model, the normal tractions on the faults decrease, causing the percent difference to increase, although the magnitude of difference in normal tractions does not exceed 0.05 kPa. The underestimation of the normal compression on the faults by assuming that the tractions follow the lithostatic distribution will cause the W_{fric} to be less than the true W_{fric} in the physical experiments.

Supplemental Fig. S.3.3

Kinematic compatibility assessment. Net displacement fields (A), and kinematic compatibility fields, *K* (B) for incremental displacement fields of left (upper row) and right (lower row) side of experiment E375. In the left side displacement field, slip along faults produces localized regions of high *K*. In the right side displacement field, artificial noise due to inadequate image quality produces many patches of high *K*. C) Histogram of *K* field for left and right side reveal the distribution of higher *K* for the right side, compared to the left side. To compare the kinematic compatibility of each displacement field to other fields, we consider the mean plus one standard deviation of the *K* field as the kinematic compatibility value representing that field, K^F (red). We compare K^F from each experimental displacement field to determine the most reliable displacement fields from which to estimate the work budget components. This comparison excludes the right side displacement fields of experiment E375, and includes the left side displacement fields of experiments E375.

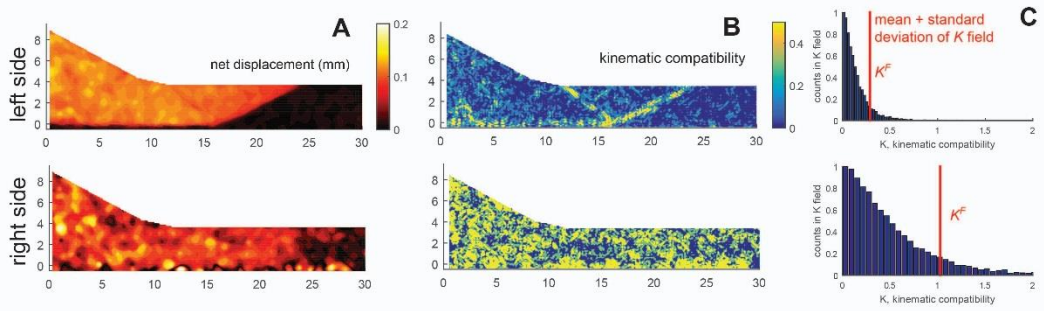

Supplemental Fig. S.3.4

Physical E estimates using DIC fields. Estimates of effective elastic modulus using stress-strain relationship of physical accretionary wedge. To calculate the incremental horizontal strain in each increment of each experiment, we find the difference in the horizontal displacements at the lateral edges of each compacting region, ΔU_x, within the left side views (A) and the right side views (B). We consider the incremental horizontal strain as $\Delta U_x/L$, where L is the length of the compacting region. To identify the representative U_x at each end, we take the median U_x within 1 cm of each end of the compacting region. The resulting stress-strain relationships for experiment E373 (C), E374 (D), E375 (E), and E376 (F). Minimum and maximum estimates for each experiment are derived from a maximum (8 cm) and minimum (4 cm) potential height of load-bearing area of sandpack in contact with backwall. Gradients in the displacement field indicate that the compacting region in the moving base experiments is 20 cm long (in the horizontal direction) and 4 cm tall (in the vertical direction), and in the moving backwall experiments is 10 cm long and 8 cm tall. Blue and pink lines indicate stress-strain relationship for left and right sides of each experiment, respectively. Black lines indicate stress-strain relationship using average of cumulative strain of left and right sides. Black dots indicate 50% peak stress, at which tangent to stress-strain curve determines elastic modulus. E) Cumulative strain calculated from right side displacement fields is excluded for experiment E375 because the kinematic compatibility criterion indicates high artificial noise for the right side displacement fields of experiment E375.

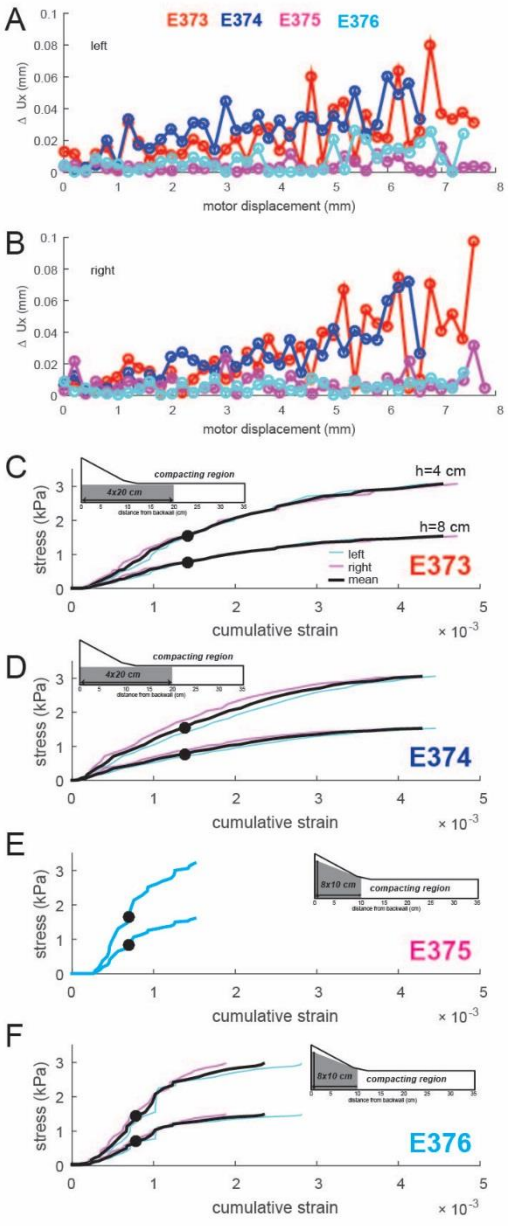

Supplemental Fig. S.3.5

Work budget of physical experiments. Work budget of individual physical experiments: external work, W_{ext} (A), internal work, W_{int} (B), frictional work, W_{fric} (C), and gravitational work, W_{grav} (D). First two columns show work budget of experiments excluding (red: E373, pink: E375) and including (dark blue: E374, light blue: E376) glass bead layer. Squares show average of work components calculated for the left and right side of the experiment at each increment. Height of error bars are the difference between the work components calculated for the opposing sides. Last two columns show incremental work component at selected increments: at the onset of faulting, the pre-faulting stage, when the work component is maximized, and at the post-faulting stage. The incremental work budgets are similar for the experiments in each set of experiments that include or exclude the glass beads, except for the estimates of W_{int}. The estimates of W_{int} differ by greater magnitudes than the other components of the work budget because the W_{int} estimates are more sensitive to artificial noise in the incremental displacement fields than the other work budget components.

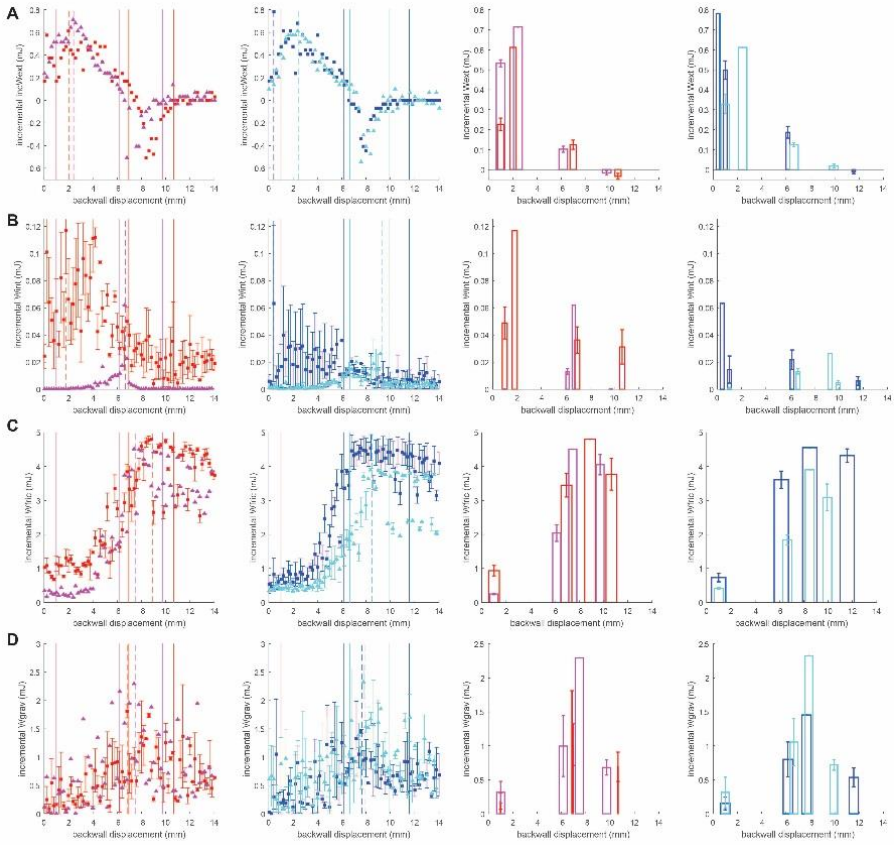

Supplemental Fig. S.3.6

Numerical loading curves. Numerical loading curves for center simulation of experiment E373 preceding (black) and following (red) fault development show non-linearity due to inelastic frictional slip. Preceding thrust development, the force exerted on the backwall continually increases with the applied backwall displacement. Following fault development, the backwall force increases until slip on the thrusts reduces the backwall force at the 6th loading step (0.3 mm of backwall displacement). To compare the work done in increments of the physical experiment to the numerical simulations, we take the work done in the last loading step of the numerical simulations (shaded region). We scale this value by the ratio of the displacement of the numerical backwall within the last loading step (0.05 mm), and the displacement of the physical backwall within each DIC increment of the experiment (0.2 mm).

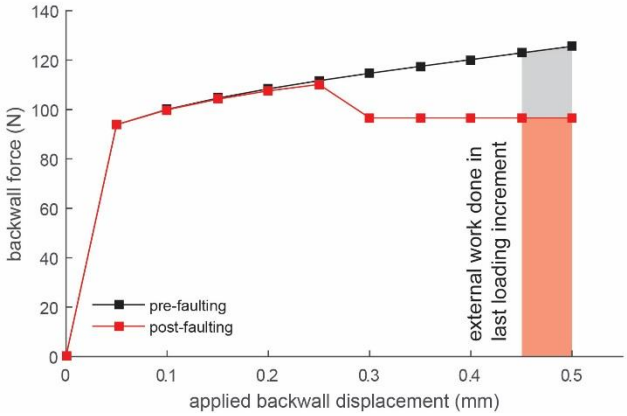

BIBLIOGRAPHY

Adam, J., D. Klaeschen, N. Kukowski, and E. Flueh, 2004. Upward delamination of Cascadia Basin sediment infill with landward frontal accretion thrusting caused by rapid glacial age material flux, *Tectonics, 23(3),* 1-21.

Adam, J., and C. D. Reuther, 2000. Crustal dynamics and active fault mechanics during subduction erosion: Application of frictional wedge analysis on to the North Chilean Forearc, *Tectonophysics,* 321, 297–325.

Adam, J., J. L. Urai, B. Wieneke, O. Oncken, K. Pfeiffer, N. Kukowski, J. Lohrmann, S. Hoth, W. van der Zee, and J. Schmatz, 2005. Shear localisation and strain distribution during tectonic faulting—new insights from granular-flow experiments and high-resolution optical image correlation techniques, *J. Struct. Geol*., *27*, 283–301, doi:10.1016/j.jsg.2004.08.008.

Baba, T., T. Hori, S. Hirano, P.R. Cummins, J.O. Park, M. Kameyama, and Y. Kaneda, 2001. Deformation of a seamount subducting beneath an accretionary prism: constraints from numerical simulation, *J. Geophys. Res*., *28(9),* 1827-1830.

Bailey, E.H., W.P. Irwin, and D.L. Jones, 1964. The Franciscan and Related Rocks and Their Significance in the Geology of Western California: California Division of Mines and Geology Bulletin, 183, 177.

Baldi, G., R. Bellotti, V. Ghionna, M. Jamiolkowski and E. Pasqualini, 1981. Cone resistance of a dry medium sand. 10th International Conference on Soil Mechanics and Foundation Engineering, Stockholm, Vol. 2, 427-432.

Bangs, N.L., T.H. Shipley, S.P. Gulick, G.F. Moore, S. Kuromoto, and Y. Nakamura, 2004. Evolution of the Nankai Trough décollement from the trench into the seismogenic zone: Inferences from three-dimensional seismic reflection imaging, *Geology, 32(4),* 273-276.

Barnes, P.M., B. Davy, R. Sutherland, and J. Delteil, 2002. Frontal accretion and thrust wedge evolution under very oblique plate convergence: Fiordland Basin, New Zealand, *Basin Res., 14(4),* 439-466.

Bellahsen, N. and J.M. Daniel, 2005. Fault reactivation control on normal fault growth: an experimental study. Journal of Structural Geology, 27(4), 769-780.

Bernard, S., J.-P. Avouac, S. Dominguez, and M. Simoes, 2007. Kinematics of fault-related folding derived from a sandbox experiment, *J. Geophys. Res., 112,* B03S12, doi: 10.1029/2005JB004149.

Bieniawski, Z.T., 1984. Rock Mechanics Design in Mining and Tunnelling. A.A. Balkema, The Netherlands.

Bigi, S., L. Di Paolo, L. Vadacca, and G. Gambardella, 2010. Load and unload as interference factors on cyclical behavior and kinematics of Coulomb wedges: insights from sandbox experiments, *J. Struct. Geol*., *32(1)*, 28-44.

Blake, M. C., D. G. Howell, and A. S. Jayko, 1984. Tectono-stratigraphic terranes of the San Francisco Bay Region, in Blake, M. C., Jr., ed., Franciscan geology of northern California: (Pacific Sect.) Soc. Econ. Paleont. Mineral., v. 43, 5-22.

Bonini, M., 2007. Deformation patterns and structural vergence in brittle–ductile thrust wedges: an additional analogue modelling perspective. *Journal of Structural Geology*, *29*(1), 141-158.

Bonini, M., T. Souriot, M. Boccaletti, and J.P. Brun, 1997. Successive orthogonal and oblique extension episodes in a rift zone: Laboratory experiments with application to the Ethiopian Rift. Tectonics, 16(2), 347-362.

Borchardt, G., 1998. Slip rate of the northern Hayward fault at Point Pinole, California: U.S. Geological Survey National Earthquake Hazards Reduction Program, Annual Summaries, v. 39. USGS Contract No. 1434-HQ-97-GR-03103 (http://erp-web.er.usgs.gov/).

Budding, K.E., D.P. Schwartz, and D.H. Oppenheimer, 1991. Slip rate, earthquake recurrence, and seismogenic potential of the Rodgers Creek fault zone, northern California: Initial results. Geophysical Research Letters, 18(3), 447-450.

Buiter, S.J., 2012. A review of brittle compressional wedge models, *Tectonophysics*, *530*, 1-17.

Buiter, S.J., G. Schreurs, M. Albertz, T.V. Gerya, B. Kaus, W. Landry, L. Le Pourhiet, Y. Mishin, D.L. Egholm, M. Cooke and B. Maillot, 2016. Benchmarking numerical models of brittle thrust wedges. *Journal of structural geology*, *92*, pp.140-177.

Burbidge, D.R., and J. Braun 2002. Numerical models of the evolution of accretionary wedges and fold-and-thrust belts using the distinct-element method, *Geophys. J. Int*., *148*, 542-561.

Bürgmann, R., D.D. Pollard, and S.J. Martel, 1994. Slip distributions on faults: effects of stress gradients, inelastic deformation, heterogeneous host-rock stiffness, and fault interaction. Journal of Structural Geology, 16(12), 1675-1690.

Byerlee, J., 1978. Friction of rocks. Pure and applied geophysics, 116(4-5), 615-626.

Byrne, T. and D. Fisher, 1987. Episodic growth of the Kodiak convergent margin, *Nature*, *325*, 338-341.

Byrne, D.E., W.H. Wang, and D.M. Davis, 1993. Mechanical role of backstops in the growth of forearcs. *Tectonics, 12*(1), 123-144.

Chang, C., M.D. Zoback, and A. Khaksar, 2006. Empirical relations between rock strength and physical properties in sedimentary rocks. *Journal of Petroleum Science and Engineering, 51*(3), 223-237.

Chester, J.S., F.M. Chester, and A.K. Kronenberg, 2005. Fracture surface energy of the Punchbowl fault, San Andreas system. *Nature, 437(7055),* 133-136.

Chester, J.S. and R.C. Fletcher, 1997. Stress distribution and failure in anisotropic rock near a bend on a weak fault. Journal of Geophysical Research: Solid Earth, 102(B1), 693-708.

Ching, K.E., M.L. Hsieh, K.M. Johnson, K.H. Chen, R.J. Rau, and M. Yang, 2011. Modern vertical deformation rates and mountain building in Taiwan from precise leveling and continuous GPS observations, 2000–2008. *Journal of Geophysical Research: Solid Earth*, *116*(B8).

Coleman, R.G., 2000. Prospecting for ophiolites along the California continental margin, in Dilek, Y.D., Moores, E.M., Elthon, D., and Nicolas, A., eds., Ophiolites and Oceanic Crust: New Insights from Field Studies and the Ocean Drilling Program: Geological Society of America Special Paper 349, 351–364.

Collettini, C., A. Niemeijer, C. Viti, and C. Marone, 2009. Fault zone fabric and fault weakness. Nature, 462(7275), 907-910.

Cooke, M.L., and E. H. Madden, 2014. Is the Earth lazy? A review of work minimization in fault evolution, *J. Struct. Geol*., *66*, 334–346, doi:10.1016/j.jsg. 2014.05.004.

Cooke, M.L., and S. Murphy, 2004. Assessing the work budget and efficiency of fault systems using mechanical models. *J. Geophys. Res: Solid Earth*, *109*(B10).

Cooke, M. L., and D. D. Pollard, 1997. Bedding plane slip in initial stages of fault-related folding. Journal of Structural Geology, 19, 567-581.

Cooke, M.L., J.E. Reber, and S. Haq, 2016. Physical Experiments of Tectonic Deformation and Processes: Building a Strong Community. *GSA Today*, *26*(12).

Cooke, M.L., M.T. Schottenfeld, and S.W. Buchanan, 2013. Evolution of fault efficiency at restraining bends within wet kaolin analog experiments. Journal of Structural Geology, 51, 180-192.

Cowie, P.A., S. Gupta, and N.H. Dawers, 2000. Implications of fault array evolution for synrift depocentre development: insights from a numerical fault growth model. Basin Research, 12(3-4), 241-261.

Crider, J.G. and D.D. Pollard, 1998. Fault linkage: three-dimensional mechanical interaction between echelon normal faults. Journal of Geophysical Research: Solid Earth, 103(B10), 24373-24391.

Cruz, L., J. Malinski, A. Wilson, W.A. Take, and G. Hilley, 2010. Erosional control of the kinematics and geometry of fold-and-thrust belts imaged in a physical and numerical sandbox, *J. Geophys. Res: Solid Earth*, *115*(B9).

Cubas, N., C. Barnes, and B. Maillot, 2013. Inverse method applied to a sand wedge: estimation of friction parameters and uncertainty analysis, *J. Struct. Geo.*, *55*, 101-113.

Cubas, N., Y.M. Leroy, and B. Maillot, 2008. Prediction of thrusting sequences in accretionary wedges, *J. Geophys. Res*., *113*, B12412**,** doi:10.1029/2008JB005717.

Cubas, N., B. Maillot, and C. Barnes, 2010. Statistical analysis of an experimental compressional sand wedge, *J. Struct. Geo.*, *32*, 818-831, doi:10.1016/j.jsg.2010.05.010.

Cubas, N., P. Souloumiac, and S. Singh, 2016. Relationship link between landward vergence in accretionary prisms and tsunami generation, *Geology*, doi:10.1130/G38019.1

Dahlen, F., 1984. Noncohesive critical Coulomb wedges: An exact solution, *J. Geophys. Res*., *89*, 10125-10133.

Dahlen, F. A., 1990. Critical taper model of fold-and-thrust belts and accretionary wedges, *Annu. Rev. Earth Planet. Sci*., *18*, 55–99.

Dahlen, F.A., J. Suppe and D. Davis, 1984. Mechanics of fold-and-thrust belts and accretionary wedges: cohesive coulomb theory, *J. Geophys. Res.*, *89*(B12), 10087–10101.

Daily, M.C., J. Chorowicz, and D. Fairhead, 1989. Rift basin evolution in Africa: the influence of reactivated steep basement shear zones. In: Cooper, M.A., Williams, G.D. (Eds.), Inversion Tectonics, Geological Society of London Special Publication, 44, 309–334.

Daphalapurkar, N.P., F. Wang, B. Fu, H. Lu, and R. Komanduri, 2011. Determination of mechanical properties of sand grains by nanoindentation. *Experimental Mechanics*, *51*(5), 719-728.

Davey, F.J., M. Hampton, J. Childs, M.A. Fisher, K. Lewis, and J.R. Pettinga, 1986. Structure of a growing accretionary prism, Hikurangi margin, New Zealand, *Geology*, *14(8*), 663-666.

Davis, D., J. Suppe and F. Dahlen, 1983. Mechanics of fold-and-thrust belts and accretionary wedges, *J. Geophys. Res*., *88*, 1153-1172.

Del Castello, M., and M.L. Cooke, 2007. Underthrusting-accretion cycle: work budget as revealed by the boundary element method, *J. Geophys. Res*., *113*, B12404, 1–14, doi:10.1029/2007JB004997.

Del Ventisette, C., D. Montanari, F. Sani, and M. Bonini, 2006. Basin inversion and fault reactivation in laboratory experiments. Journal of Structural Geology, 28(11), 2067-2083.

Dempsey, D., S. Ellis, R. Archer, and J. Rowland, 2012. Energetics of normal faults earthquakes on dip slip faults. Geology, 79-282. http://dx.doi.org/10.1130/ G32643.1.

Desrues, J., and G. Viggiani, 2004. Strain localization in sand: an overview of the experimental results obtain in Grenoble using stereophotogrammetry. International Journal for Numerical and Analytical Methods in Geomechanics 28, 279-321.

Dixon, T.H., R.J. Stern, and I.M. Hussein, 1987. Control of Red Sea rift geometry by Precambrian structures. Tectonics 6, 551–571.

Dooley, T. and K. McClay, 1997. Analog modeling of pull-apart basins. AAPG bulletin, 81(11), 1804-1826.

Dooley, T., K. McClay, and M. Bonora, 1999. January. 4D evolution of segmented strike-slip fault systems: applications to NW Europe. In Geological Society, London, Petroleum Geology Conference series (Vol. 5, 215-225). Geological Society of London.

Dooley, T.P. and G. Schreurs, 2012. Analogue modelling of intraplate strike-slip tectonics: A review and new experimental results. Tectonophysics, 574, 1-71.

Dotare, T., Y. Yamada, J. Adam, T. Hori and H. Sakaguchi, 2016. Initiation of a thrust fault revealed by analog experiments, *Tectonophysics*, doi: 10.1016/j.tecto.2015.12.023.

Dubois, A., F. Odonne, G. Massonnat, T. Lebourg, and R. Fabre, 2002. Analogue modelling of fault reactivation: tectonic inversion and oblique remobilisation of grabens. Journal of Structural Geology, 24, 1741–1752.

Du, Y. and A. Aydin, 1993. The maximum distortional strain energy density criterion for shear fracture propagation with applications to the growth paths of en echelon faults, *Geophys. Res. Lett., 20*(11), 1091-1094.

Du, Y. and A. Aydin, 1996. Is the San Andreas big bend responsible for the Landers earthquake and the eastern California shear zone?, *Geology, 24*(3), 219-222.

D'Errico, J, 2008. Inpainting nan elements in 3d, MATLAB Central File Exchange.

Ellis, S., C. Beaumont and O. A. Pfiffner, 1999. Geodynamic models of crustal-scale episodic tectonic accretion and underplating in subduction zones, *J. Geophys. Res.: Solid Earth, 104(B7),* 15169-15190.

Ellis, S., G. Schreurs, and M. Panien, 2004. Comparisons between analogue and numerical models of thrust wedge development, *J. Struct. Geo., 26(9),* 1659-1675.

Escartin, J., G. Hirth, and B. Evans, 1997. Nondilatant brittle deformation of serpentinites: Implications for Mohr-Coulomb theory and the strength of faults. Journal of Geophysical Research: Solid Earth, 102(B2), 2897-2913.

Faccenna, C., T. Nalpas, J.P. Brun, and P. Davy, 1995. The influence of preexisting thrust fault on normal fault geometry in nature and in experiments. Journal of Structural Geology, 17.

Ferrill, D.A., Morris, A.P. and Smart, K.J., 2007. Stratigraphic control on extensional fault propagation folding: Big Brushy Canyon monocline, Sierra del Carmen, Texas. Geological Society, London, Special Publications, 292(1), 203-217.

Field, E.H., G.P. Biasi, P. Bird, T.E. Dawson, K.R. Felzer, D.D. Jackson, K.M. Johnson, T.H. Jordan, C. Madden, A.J. Michael, and K.R. Milner, 2015. Long-term time-dependent probabilities for the third Uniform California Earthquake Rupture Forecast (UCERF3). Bulletin of the Seismological Society of America, 105(2A), 511-543.

Finzi, Y., E.H. Hearn, Y. Ben-Zion, and V. Lyakhovsky, 2009. Structural properties and deformation patterns of evolving strike-slip faults: Numerical simulations incorporating damage rheology. Pure and Applied Geophysics,166(10-11), 1537-1573.

Fulton, P.M., E.E. Brodsky, Y. Kano, J. Mori, F. Chester, T. Ishikawa, R.N. Harris, W. Lin, N. Eguchi, and S. Toczko, 2013. Low coseismic friction on the Tohoku-Oki fault determined from temperature measurements. *Science, 342*(6163), 1214-1217.

Furlong, K.P., W.D. Hugo, and G. Zandt, 1989. Geometry and evolution of the San Andreas fault zone in northern California. Journal of Geophysical Research: Solid Earth, 94(B3), 3100-3110.

Ghisetti, F. C., P. M. Barnes, S. Ellis, A. A. Plaza-Faverola, and D. H. N. Barker, 2016. The last 2 Myr of accretionary wedge construction in the central Hikurangi margin (North Island, New Zealand): Insights from structural modeling, Geochem. Geophys. Geosyst., 17, 2661–2686, doi:10.1002/2016GC006341.

Graveleau, F., J. Malavielle, and S. Dominquez, 2012. Experimental modelling of orogenic wedges: a review, *Tectonophysics, 538–540*, 1–66, doi:10.1016/j.tecto.2012.01.027.

Gudmundsson, A., T.H. Simmenes, B. Larsen, and S.L. Philipp, 2010. Effects of internal structure and local stresses on fracture propagation, deflection, and arrest in fault zones. J. Struct. Geol. 32, 1643–1655.

Gulick, S.P.S., N.L.B. Bangs, T.H. Shipley, Y. Nakamura, G. Moore, and S. Kuramoto, 2004. Three-dimensional architecture of the Nankai accretionary prism's imbricate thrust zone off Cape Muroto, Japan: Prism reconstruction via en echelon thrust propagation, *J. Geophys. Res.: Solid Earth, 109*(B2), 2156-2202, doi:10.1029/2003JB002654.

Gupta, S., P.A. Cowie, N.H. Dawers, and J.R. Underhill, 1998. A mechanism to explain rift-basin subsidence and stratigraphic patterns through fault-array evolution. Geology, 26(7), 595-598.

Gutscher, M., N. Kukowski, J. Malavieille, and S. Lallemand, 1996. Cyclical Behavior in Thrust Wedges: Insights from High Basal Friction Sandbox Experiments, *Geology, 24*, 135-138.

Gutscher, M.A., N. Kukowski, J. Malavieille, and S. Lallemand, 1998. Episodic imbricate thrusting and underthrusting: analog experiments and mechanical analysis applied to the Alaskan Accretionary Wedge, *J. Geophys. Res., 103*, 10,161-10,176.

Hatem, A.E., M.L. Cooke, and E.H. Madden, 2015. Evolving efficiency of restraining bends within wet kaolin analog experiments. Journal of Geophysical Research: Solid Earth, 120(3), 1975-1992.

Haq, S.S., 2012. Out-of-sequence thrusting in experimental Coulomb wedges: Implications for the structural development of mega-splay faults and forearc basins, *Geophys. Res. Lett., 39(20)*, L20306, 1-5.

Hardy, S., C. Duncan, J. Masek, and D. Brown, 1998. Minimum work, fault activity and the growth of critical wedges in fold and thrust belts, *Basin Res., 10*, 365–373., doi:/10.1046/j.1365-2117.1998.00073.x.

Hart, D.J. and H.F. Wang, 1995. Laboratory measurements of a complete set of poroelastic moduli for Berea sandstone and Indiana limestone. *Journal of Geophysical Research: Solid Earth, 100*(B9), .17741-17751.

Hayward Fault Paleoearthquake Group, 1999. Timing of paleoearthquakes on the northern Hayward fault—Preliminary evidence in El Cerrito, California: U.S. Geological Survey Open-File Report 99-318, 34.

Hecker, S., D. Pantosti, D.P. Schwartz, J.C. Hamilton, L.M. Reidy, and T.J. Powers, 2005. The most recent large earthquake on the Rodgers Creek fault, San Francisco Bay area. Bulletin of the Seismological Society of America, 95(3), 844-860.

Herbert, J.W., 2014. Investigating fault system deformation with numerical models and analog experiments, Ph. D. thesis, Dep. of Geosciences, Univ. of Massachusetts, Amherst, Massachusetts, USA.

Herbert, J.W., M.L. Cooke, P. Souloumiac, E.H. Madden, B.C. Mary and B. Maillot, 2015. The work of fault growth in laboratory sandbox experiments, *Earth Planet. Sci. Lett., 432*, 95-102.

Holdsworth, R.E., E.W.E. Van Diggelen, C.J. Spiers, J.H.P. De Bresser, R.J. Walker, and L. Bowen, 2011. Fault rocks from the SAFOD core samples: Implications for weakening at shallow depths along the San Andreas Fault, California. Journal of Structural Geology, 33(2), 132-144.

Hoth, S., 2005. Deformation, erosion, and natural resources in continental collision zones – insight from scaled sandbox simulations, PhD thesis. Geo-Forschungs Zentrum Potsdam, Potsdam, Germany. 141.

Hoth, S., A. Hoffmann-Rothe, and N. Kukowski, 2007. Frontal accretion: An internal clock for bivergent wedge deformation and surface uplift. *Journal of Geophysical Research: Solid Earth, 112*(B6).

Huiqi, L., K.R. McClay, and D. Powell, 1992. Physical models of thrust wedges. In *Thrust Tectonics*, edited by K. R. McClay, Chapman and Hall, London, 71-8l, doi: 10.1007/978-94-011-3066-0.

Ikari, M.J. and D.M. Saffer, 2011. Comparison of frictional strength and velocity dependence between fault zones in the Nankai accretionary complex. *Geochemistry, Geophysics, Geosystems*, *12*(4).

Jaeger, J. C., N.G. Cook, and R.W. Zimmerman, 2007. Fundamentals of Rock Mechanics, Blackwell Publishing.

Kattenhorn, S.A. and D.D. Pollard, 2001. Integrating 3-D seismic data, field analogs, and mechanical models in the analysis of segmented normal faults in the Wytch Farm oil field, southern England, United Kingdom. AAPG bulletin, 85(7), 1183-1210.

Kirkpatrick, J.D., C.D., Rowe, J.C. White and E.E. Brodsky, 2013. Silica gel formation during fault slip: Evidence from the rock record. *Geology*, *41*(9), 1015-1018.

Klinkmüller, M., M. Rosenau, D. Boutelier, H. Kemnitz, and G. Schreurs, 2008, September. Properties benchmark of granular and viscous analogue materials. In *International Geological Modelling Conference–GeoMod*.

Klinkmüller, M., G. Schreurs, M. Rosenau, and H. Kemnitz, 2016. Properties of granular analogue model materials: A community wide survey. *Tectonophysics*, *684*, 23-38.

Knuth, M.W., H.J. Tobin, and C. Marone, 2013. Evolution of ultrasonic velocity and dynamic elastic moduli with shear strain in granular layers. *Granular Matter*, *15*(5), 499-515.

Konstantinovskaia, E., and J. Malavieille, 2005. Erosion and exhumation in accretionary orogens: experimental and geological approaches, *Geochem. Geophys. Geosyst., 6* (*Q02006*), doi: 10.1029/2004GC000794.

Konstantinovskaya, E., and J. Malavieille, 2011. Thrust wedges with décollement levels and syntectonic erosion: a view from analogue models, *Tectonophysics, 502 (3–4*), 336–350.

Kopf, A. and K.M. Brown, 2003. Friction experiments on saturated sediments and their implications for the stress state of the Nankai and Barbados subduction thrusts. *Marine Geology*, *202*(3), 193-210.

Kopp, C., J. Fruehn, E.R. Flueh, C. Reichert, N. Kukowski, J. Bialas, and D. Klaeschen, 2000. Structure of the Makran subduction zone from wide-angle and reflection seismic data, *Tectonophysics, 329(1*), 171-191.

Kopp, H., and N. Kukowski, 2003. Backstop geometry and accretionary mechanics of the Sunda margin, *Tectonics, 22(6*), 1072, doi:10.1029/2002TC001420.

Koyi, H., 1995. Mode of internal deformation in sand wedges. *Journal of Structural Geology*, *17*(2), 293297-295300.

Koyi, H.A., and J. Cotton, 2004. Experimental insights on the geometry and kinematics of fold-and-thrust belts above weak, viscous evaporitic décollement; a discussion, *J. Struct. Geo., 26(11)*, 2139–2141.

Krantz, R.W. 1991. Measurements of friction coefficients and cohesion for faulting and fault reactivation in laboratory models using sand and sand mixtures, *Tectonophysics, 188 (1–2*), 203–207, doi:10.1016/0040-1951[91]90323-K.

Lallemand, S., P. Schnrle, and J. Malavieille, 1994. Coulomb theory applied to accretionary and nonaccretionary wedges: Possible causes for tectonic erosion and/or frontal accretion, *J. Geophys. Res., 99*, 12033-12055.

Lambe, T.W., and R.V. Whitman, 1969. Soil Mechanics, 553, John Wiley Press, New York.

Lettis, W., J. Bachhuber, R. Witter, C. Brankman, C.E. Randolph, A. Barka, W.D. Page, and A. Kaya, 2002. Influence of releasing step overs on surface fault rupture and fault segmentation: examples from the 17 August 1999 Izmit earthquake on the North Anatolian Fault, Turkey. Bulletin of the Seismological Society of America, 92(1), 19-42.

Lo, T.W., K.B. Coyner, and M.N. Toksöz, 1986. Experimental determination of elastic anisotropy of Berea sandstone, Chicopee shale, and Chelmsford granite. *Geophysics, 51*(1), 164-171.

Lockner, D.A., C. Morrow, D. Moore, and S. Hickman, 2011. Low strength of deep San Andreas fault gouge from SAFOD core. Nature, 472(7341), 82-85.

Lohrmann, J., N. Kukowski, J. Adam, and O. Oncken, 2003. The impact of analogue material properties on the geometry, kinematics, and dynamics of convergent sand wedges, *J. Struct. Geol., 25*, 1691–1711, doi:/10.1016/S0191- 8141[03]00005-1.

Lundberg, N. and J.C. Moore, 1986. Macroscopic structural features in Deep Sea Drilling Project cores from forearc regions. *Geological Society of America Memoirs, 166*, 13-44.

MacKay, M.E., 1995. Structural variation and landward vergence at the toe of the Oregon accretionary prism. *Tectonics, 14*(6), 1309-1320.

Madden, E., M.L. Cooke, J.A. McBeck, J. Herbert (in rev.). Fault propagation and estimates of fault energy budgets using the fault growth modeling tool GRowth by Optimization of Work (GROW), submitted to International Journal of Rock Mechanics & Mining Sciences.

Maillot, B., 2013. A sedimentation device to produce uniform sand packs, *Tectonophysics, 593*, 85–94, doi:/10.1016/j.tecto.2013.02.028.

Maillot, B., C. Barnes, J.M. Mengus, and J.M. Daniel, 2007. Constraints on friction coefficients by an inverse analysis of sand box thrust dips, *J. Struct. Geol., 29*, 117– 128.

Maillot, B., and H. Koyi, 2006. Thrust dip and thrust refraction in fault-bend folds: Analogue models and theoretical predictions, *J. Struct. Geol., 28*, 36– 49.

Maillot, B., and Y.M. Leroy, 2003. Optimal dip based on dissipation of back thrusts and hinges in fold-and-thrust belts, *J. Geophys. Res., 108*(B6).

Mair, K., K.M. Frye, and C. Marone, 2002. Influence of grain characteristics on the friction of granular shear zones. *J. Geophys. Res*., vol. 107, B10, 2219, doi:10.1029/2001JB000516

Malavielle, J., 2010. Impact of erosion, sedimentation, and structural heritage on the structure and kinematics of orogenic wedges: analog models and case studies, *GSA Today*, *20(1*), 4–10.

Mann, P., M.R. Hempton, D.C. Bradley, and K. Burke, 1983. Development of pull-apart basins. The Journal of Geology, 529-554.

Marshall, S.T., S.A. Kattenhorn, and M.L. Cooke, 2010. Secondary normal faulting in the Lake Mead fault system and implications for regional fault mechanics. *Geological Society of America Special Papers*, *463*, pp.289-310.

Mary, B.C.L., B. Maillot, and Y.M. Leroy, 2013. Deterministic Chaos in frictional wedges revealed by convergence analysis, *Int. J. Num. Anal. Methods Geomech., 37*, 3036–3051**,** http://dx.doi.org/10.1002/nag.2177.

Masek, J.G. and C.C. Duncan, 1998. Minimum-work mountain building. *Journal of Geophysical Research: Solid Earth*, *103*(B1), 907-917.

Matti, J.C. and D.M. Morton, 1993. Paleogeographic evolution of the San Andreas fault in southern California: A reconstruction based on a new cross-fault correlation. Geological Society of America Memoirs, 178, 107-160.

Mazzotti, S., P. Henry, and X. Le Pichon, 2001. Transient and permanent deformation of central Japan estimated by GPS: 2. Strain partitioning and arc–arc collision. *Earth and Planetary Science Letters*, *184*(2), 455-469.

McBeck, J., E. Madden, and M.L. Cooke, 2016. Growth by Optimization of Work (GROW): A new modeling tool that predicts fault growth through work minimization. Computers and Geosciences, 88, 142-151.

McClay, K. and T. Dooley, 1995. Analogue models of pull-apart basins. Geology, 23(8), 711-714.

McClay, K. R., and P.S. Whitehouse, 2004. Analog modeling of doubly vergent thrust wedges, in *Thrust Tectonics and Hydrocarbon Systems*, edited by K. R. McClay, AAPG Mem., 82, 187 – 209.

McConnell, R.B., 1972. Geological development of the rift system of eastern Africa. Geological Society of America Bulletin 83, 2549–2572.

McKay, M.E., G.F. Moore, G.R. Cochrane, J.C. Moore, and L.D. Kulm, 1992. Landward vergence and oblique structural trends in the Oregon margin accretionary prism: implications and effect on fluid flow. Earth and Planetary Science Letters 109, 477-491.

McLaughlin, R. J., A. M. Sarna-Wojcicki, D.L. Wagner, R.J. Flack, V. E. Langenheim, R. C. Jachens, K. Clahan, and J. R. Allen, 2012. Evolution of the Rodgers Creek–Maacama right-lateral fault system and associated basins east of the northward-migrating Mendocino Triple Junction, northern California, Geosphere, 8, 342-373, doi:10.1130/GES00682.

Miyakawa, A., Y. Yamada, and T. Matsuoka, 2010. Effect of increased shear stress along a plate boundary fault on the formation of an out-of-sequence thrust and a break in surface slope within an accretionary wedge, based on numerical simulations, *Tectonophysics, 484(1)*, 127-138.

Moore, J.C., J. Diebold, M.A. Fisher, J. Sample, T. Brocher, M. Talwani, J. Ewing, R. von Huene, C. Rowe, D. Stone, and C. Stevens, 1991. EDGE deep seismic reflection transect of the eastern Aleutian arc-trench layered lower crust reveals underplating and continental growth, *Geology, 19(5*), 420-424.

Moore, D.E. and D.A. Lockner, 2004. Crystallographic controls on the frictional behavior of dry and water-saturated sheet structure minerals. Journal of Geophysical Research: Solid Earth, 109(B3).

Moore, G.F., D. Saffer, M. Studer, and P. Costa Pisani, 2011. Structural restoration of thrusts at the toe of the Nankai Trough accretionary prism off Shikoku Island, Japan: Implications for dewatering processes, *Geochem. Geophys. Geosyst., 12(5*), Q0AD12, doi: 10.1029/2010GC003453.

Moore, G.F., T.H. Shipley, P.L. Stoffa, D.E. Karig, A. Taira, S. Kuramoto, H. Tokuyama and K. Suyehiro, 1990. Structure of the Nankai Trough accretionary zone from multichannel seismic reflection data, *J. Geophys. Res.: Solid Earth, 95(B6*), 8753-8765.

Morley, C.K., C. Haranya, W. Phoosongsee, S. Pongwapee, A. Kornsawan, and N. Wonganan, 2004. Activation of rift oblique and rift parallel pre-existing fabrics during extension and their effect on deformation style: examples from the rifts of Thailand. Journal of Structural Geology, 26(10), 1803-1829.

Morgan, J.K., and D.E. Karig, 1995. Kinematics and a balanced and restored cross-section across the toe of the eastern Nankai accretionary prism. Journal of Structural Geology 17, 31–45.

Morgan, J.K., D.E. Karig, and A. Maniatty, 1994. The estimation of diffuse strains in the toe of the western Nankai accretionary prism: A kinematic solution. *Journal of Geophysical Research: Solid Earth, 99*(B4), 7019-7032.

Morrow, C.A. and D.A. Lockner, 2001. Hayward fault rocks: Porosity, density and strength measurements. US Department of the Interior, US Geological Survey.

Mulugeta, G., 1988. Modelling the geometry of Coulomb thrust wedges, *J. Struct. Geo., 10*, 847–859.

Mulugeta, G., and H. Koyi, 1992. Episodic accretion and strain partitioning in a model sand wedge, *Tectonophysics, 202(2*), 319-333.

Naylor, M., H.D. Sinclair, S. Willett, and P.A. Cowie, 2005. A discrete element model for orogenesis and accretionary wedge growth, *J. Geophys. Res.: Solid Earth, 110*(B12).

Nemcok, M., M.P. Coward, W.J. Sercombe and R.A. Klecker, 1999. Structure of the West Carpathian accretionary wedge: insights from cross section construction and sandbox validation, *Physics and Chemistry of the Earth, Part A: Solid Earth and Geodesy, 24(8*), 659-665.

Okubo, C.H., and R.A. Schultz, 2005. Evolution of damage zone geometry and intensity in porous sandstone: insight gained from strain energy density, *J. Geol. Soc., 162*(6), 939-949.

Olson, E.L., and M.L. Cooke, 2005. Application of three fault growth criteria to the Puente Hills thrust system, Los Angeles, California, USA, *J. Struct. Geol., 27*(10), 1765-1777.

Panien, M., G. Schreurs, and A. Pfiffner, 2006. Mechanical behaviour of granular materials used in analogue modelling: insights from grain characterisation, ring-shear tests and analogue experiments. Journal of Structural Geology 28, 1710-1724.

Parsons, T., R. Sliter, E.L. Geist, R.C. Jachens, B.E. Jaffe, A. Foxgrover, P.E. Hart and J. McCarthy, 2003. Structure and mechanics of the Hayward–Rodgers creek fault step over, San Francisco bay, California. Bulletin of the Seismological Society of America, 93(5), 2187-2200.

Peacock, D.C.P. and D.J. Sanderson, 1992. Effects of layering and anisotropy on fault geometry. Journal of the Geological Society, 149(5), 793-802.

Persson, K.S., and D. Sokoutis, 2002. Analogue models of orogenic wedges controlled by erosion, *Tectonophysics, 356 (4),* 323–336.

Pittarello, L., G. Di Toro, A. Bizzarri, G. Pennacchioni, J. Hadizadeh, and M. Cocco, 2008. Energy partitioning during seismic slip in pseudotachylyte-bearing faults (Gole Larghe Fault, Adamello, Italy), *Earth Planet. Sci. Lett., 269*(1), 131-139.

Pollitz, F. F., and M. Nyst, 2005. A physical model for strain accumulation in the San Francisco Bay Region. Geophysical Journal International 160.1 302-317.

Powell, R.E., 1993. Balanced palinspastic reconstruction of pre-late Cenozoic paleogeology, southern California: Geologic and kinematic constraints on evolution of the San Andreas fault system. Geological Society of America Memoirs, 178, 1-106.

Rahe, B., D.A. Ferrill, and A.P. Morris, 1998. Physical analog modeling of pull-apart basin evolution. Tectonophysics, 285(1), 21-40.

Robertson, P.K. and R.G. Campanella, 1983. Interpretation of cone penetration tests. Part I: Sand. *Canadian geotechnical journal*, *20*(4), 718-733.

Saffer, D. M., and B. A. Bekins, 2002. Hydrologic controls on the morphology and mechanics of accretionary wedges, *Geology, 30*, 271– 274.

Sassi, W., B. Colletta, P. Bale, and T. Pacquereau, 1993. Modelling of structural complexity in sedimentary basins: the role of pre-existing faults in thrust tectonics. Tectonophysics 226, 97–112.

Saltzer, S.D., and D.D. Pollard, 1992. Distinct element modelling of structures formed in sedimentary overburden by extensional reactiva- tion of basement normal faults. Tectonics 11, 165–174.

Savage, H.M., and M.L. Cooke, 2010. Unlocking the effects of friction on fault damage zones. *J. Struct. Geol., 32 (11*), 1732-1741, doi:10.1016/j.jsg.2009.08.014.

Schmidt, D.A. and R. Bürgmann, 2003. Time-dependent land uplift and subsidence in the Santa Clara valley, California, from a large interferometric synthetic aperture radar data set. *Journal of Geophysical Research: Solid Earth*, *108*(B9).

Schwartz, D. P., D. Pantosti, S. Hecker, K. Okumura, K. E. Budding, and T. Powers, 1992. Late Holocene behavior and seismogenic potential of the Rodgers Creek fault zone, Sonoma County, California, in Proc. of the Second Conference on Earthquake Hazards in the Eastern San Francisco Bay Area, G. Borchardt, S. E. Hirschfeld, J. J. Lienkaemper, P. McClellan, and I. G. Wong (Editors), Calif. Div. Mines Geol. Spec. Publ. 113, 393–398.

Schwartz, D.P., J.J. Lienkaemper, S. Hecker, K.I. Kelson, T.E. Fumal, J.N. Baldwin, G.G. Seitz, and T.M. Niemi, 2014. The earthquake cycle in the San Francisco Bay region: AD 1600–2012. Bulletin of the Seismological Society of America, 104(3), 1299-1328.

Seely, D.R., 1977. The significance of landward vergence and oblique structural trends on trench inner slopes. *Island Arcs, Deep Sea Trenches and Back-Arc Basins*, 187-198.

Sibson, R.H. and V.G. Toy, 2006. The habitat of fault-generated pseudotachylyte: Presence vs. absence of friction-melt. *Earthquakes: Radiated Energy and the Physics of Faulting*, 153-166.

Singh, S.C., N.D. Hananto, A.P. Chauhan, H. Permana, M. Denolle, A. Hendriyana, and D. Natawidjaja, 2010. Evidence of active backthrusting at the NE Margin of Mentawai Islands, SW Sumatra. *Geophysical Journal International*, *180*(2), 703-714.

Smit, J.H.W., J.P. Brun, and D. Sokoutis, 2003. Deformation of brittle-ductile thrust wedges in experiments and nature, *J. Geophys. Res.: Solid Earth*, *108(B10).*

Smith, M., and P. Mosley, 1993. Crustal heterogeneity and basement influence on the development of the Kenya Rift, East Africa. Tectonics 12, 591–606.

Souloumiac, P., Y.M. Leroy, B. Maillot, and K. Krabbenhøft, 2009. Predicting stress distributions in fold-and-thrust belts and accretionary wedges by optimization, *J. Geophys. Res., 114*, doi:10.1029/2008JB005986.

Souloumiac, P., K. Krabbenhøft, Y.M. Leroy, and B. Maillot, 2010. Failure in accretionary wedges with the maximum strength theorem: numerical algorithm and 2D validation, *Comput. Geosci., 14*, 793-811, doi:10.1007/s10596-010- 9184-4.

Souloumiac, P., B. Maillot, and Y. M. Leroy, 2012. Bias due to side wall friction in sand box experiments, *J. Struct. Geol.*, *35*, 90-101, doi:10.1016/j.jsg.2011.11.002.

Strayer, L.M., P.J. Hudleston, and L.J. Lorig, 2001. A numerical model of deformation and fluid-flow in an evolving thrust wedge. Tectonophysics, 335(1), 121-145.

Storti, F., and K. McClay, 1995. Influence of syntectonic sedimentation on thrust wedges in analog models, *Geology, 23*, 999 – 1002.

Strayer, L.M., S.G. Erickson, and J. Suppe, 2004. Influence of growth strata on the evolution of fault-related folds-distinct element models. In: McClay, K.R. (Ed.), Thrust Tectonics and Hydrocarbon Systems. American Association of Petroleum Geologists, Memoir 82, 413–437.

Takami, M. and T. Itaya, 1996. Episodic accretion and metamorphism of Jurassic accretionary complex based on biostratigraphy and K-Ar geochronology in the western part of the Mino-Tanba Belt, Southwest Japan, *Island Arc, 5(3*), 321-336.

Tong, H. and A. Yin, 2011. Reactivation tendency analysis: A theory for predicting the temporal evolution of preexisting weakness under uniform stress state. Tectonophysics, 503(3), 195-200.

U.S. Geological Survey and California Geological Survey, 2006. Quaternary fault and fold database for the United States, *from USGS web site: https://earthquake.usgs.gov/hazards/qfaults/.*

Ujiie, K., H. Tanaka, T. Saito, A. Tsutsumi, J.J. Mori, J. Kameda, E.E. Brodsky, F.M. Chester, N. Eguchi, and S. Toczko, 2013. Low coseismic shear stress on the Tohoku-Oki megathrust determined from laboratory experiments. *Science, 342*(6163), 1211-1214.

von Huene, R. and D.W. Scholl, 1991. Observations at convergent margins concerning sediment subduction, subduction erosion, and the growth of continental crust, *Rev. of Geophys., 29(3*), 279-316.

Wakabayashi, J., 1989. Tectonics and metamorphism of the Franciscan and related rocks, San Francisco Bay Area, California: Unpub. Ph.D. dissertation, University of California, Davis. 124.

Wakabayashi, J., 1992. Nappes, tectonics of oblique plate convergence, and metamorphic evolution related to 140 million years of continuous subduction, Franciscan Complex, California. The Journal of Geology, 19-40.

Wakabayashi, J., 2004. Contrasting settings of serpentinite bodies, San Francisco Bay area, California: Derivation from the subducting plate vs. mantle hanging wall: International Geology Review, v. 46, p. 1103–1118, doi:10.2747/0020-6814.46.12.1103.

Wakabayashi, J., 2012. Subducted sedimentary serpentinite mélanges: Record of multiple burial-exhumation cycles and subduction erosion: Tectonophysics, v. 568–569, 230–247, doi:10.1016/j.tecto.2011.11.006.

Wakabayashi, J., and E. M. Moores, 1988, Evidence for the collision of the Salinian block with the Franciscan subduc-tion zone, California: Jour. Geology, v. 96, 245-253.

Waldhauser, F., and D.P. Schaff, 2008. Large-scale relocation of two decades of Northern California seismicity using cross-correlation and double-difference methods, J. Geophys. Res., 113, B08311, doi:10.1029/2007JB005479.

Watt, J., D. Ponce, T. Parsons, and P. Hart, 2016. Missing link between the Hayward and Rodgers Creek faults. Science Advances, 2(10), 1601441.

Wells, D.L. and K.J. Coppersmith, 1994. New empirical relationships among magnitude, rupture length, rupture width, rupture area, and surface displacement. Bulletin of the seismological Society of America, 84(4), 974-1002.

Wesnousky, S.G., 2008. Displacement and geometrical characteristics of earthquake surface ruptures: Issues and implications for seismic-hazard analysis and the process of earthquake rupture. Bulletin of the Seismological Society of America, 98(4), 1609-1632.

Willemse, E.J., 1997. Segmented normal faults: Correspondence between three-dimensional mechanical models and field data. Journal of Geophysical Research: Solid Earth, 102(B1), 675-692.

Willett, S. D., 1992. Dynamic and kinematic growth and change of a Coulomb wedge, in *Thrust Tectonics,* edited by McClay, 19-31.

Wilson, B., T. Dewers, Z.E. Reches and J. Brune, 2005. Particle size and energetics of gouge from earthquake rupture zones, *Nature*, *434*(*7034*), 749-752.

Wenk, L. and K. Huhn, 2013. The influence of an embedded viscoelastic–plastic layer on kinematics and mass transport pattern within accretionary wedges, *Tectonophysics, 608*, 653-666.

Wu, J.E., K. McClay, P. Whitehouse and T. Dooley, 2009. 4D analogue modelling of transtensional pull-apart basins. Marine and Petroleum Geology, 26(8), 1608-1623.

Yagupsky, D.L., B.A. Brooks, K.X. Whipple, C.C. Duncan, and M. Bevis, 2014. Distribution of active faulting along orogenic wedges: minimum-work models and natural analogue, *J. Struct. Geol., 66*, 90–101, doi:10.1016/j.jsg.2014.05.025.

Yamada, Y., K. Baba, A. Miyakawa and T. Matsuoka, 2014. Granular experiments of thrust wedges: insights relevant to methane hydrate exploration at the Nankai accretionary prism, *Marine and Petroleum Geology, 51*, 34-48.

Yang, Wei H., 1993. Large deformation of structures by sequential limit analysis. International Journal of Solids and Structures 30, 1001-1013.

Yin, A., 1994. Mechanics of monoclinal systems in the Colorado plateau during the Laramide orogen. J. Geophys. Res. 99, 22043–22058.

Yu, E., and P. Segall, 1996. Slip in the 1868 Hayward earthquake from the analysis of historical triangulation data, J. Geophys. Res., 101*(*B7*)*, 16101–16118, *doi:*10.1029/96JB00806.

Yuan, X.P., B. Maillot, and Y.M. Leroy, 2015. Tectonic and gravity extensional collapses in overpressured cohesive and frictional wedges, *J. Geophys. Res*. *Solid Earth, 120*, doi:10.1002/2014JB011612.

Zampieri, D., M. Massironi, R. Sedea, and V. Sparacino, 2003. Strike-slip contractional stepovers in the Southern Alps (northeastern Italy). *Eclogae Geologicae Helvetiae*, *96*(1), 115-124.

Zhao, W. L., D. M. Davis, F. A. Dahlen, and J. Suppe, 1986. Origin of convex accretionary wedges: Evidence from Barbados, *J. Geophys. Res., 91*, 10,246–10,258.

Zoback, M.D. and J.H. Healy, 1992. In situ stress measurements to 3.5 km depth in the Cajon Pass scientific research borehole: Implications for the mechanics of crustal faulting. *Journal of Geophysical Research: Solid Earth*, *97*(B4), 5039-5057.